

12-2012

Updated Force Model for Milling Nickel-based Superalloys

Andrew Henderson

Clemson University, ajh@clemson.edu

Follow this and additional works at: https://tigerprints.clemson.edu/all_dissertations



Part of the [Operations Research, Systems Engineering and Industrial Engineering Commons](#)

Recommended Citation

Henderson, Andrew, "Updated Force Model for Milling Nickel-based Superalloys" (2012). *All Dissertations*. 1037.
https://tigerprints.clemson.edu/all_dissertations/1037

This Dissertation is brought to you for free and open access by the Dissertations at TigerPrints. It has been accepted for inclusion in All Dissertations by an authorized administrator of TigerPrints. For more information, please contact kokeefe@clemson.edu.

UPDATED FORCE MODEL FOR MILLING NICKEL-BASED SUPERALLOYS

A Dissertation
Presented to
the Graduate School of
Clemson University

In Partial Fulfillment
of the Requirements for the Degree
Doctor of Philosophy
Automotive Engineering

by
Andrew James Henderson
December 2012

Accepted by:
Dr. Thomas Kurfess, Committee Co-Chair
Dr. Laine Mears, Committee Co-Chair
Dr. Mohammad Omar
Dr. Robert Prucka

ABSTRACT

Nickel-based superalloys are commonly used in applications which require high strength and resistance to creep and oxidation in extreme conditions. All nickel-based superalloys are considered difficult to machine; however, cast gamma-prime-strengthened nickel-based superalloys are more difficult to machine than common nickel-based superalloys. Machining comprises a significant portion of manufacturing processes and with advancements in technology and material properties, the methods and models used must be adapted in order to keep pace.

In this research, correlations are made, using fundamental principles, between measurements made with on-machine touch probes and the cutting tool's wear state, those correlations are used in an adaptive algorithm to estimate the size of the tool wear, and the estimates are used in an updated mechanistic cutting force model to predict the progression of cutting forces in gamma-prime-strengthened Nickel-based superalloys.

This work impacts machining operations on advanced and common materials by developing a tool wear estimation method with readily available equipment and a computationally tractable force model. It influences knowledge in the field through the fundamental relationships, robust adaptive approach, and modifications to the mechanistic force model.

This research shows that on-machine touch probes are able to measure changes in the geometry of a cutting tool as it wears; however, measurement uncertainty results in 20 μm of variation in the wear estimation. The wear estimation was improved through the use of a Kalman filter. The average error from 24 estimations was 8 μm . Addressing the geometric changes in the tool due to wear, the mechanistic cutting force model estimated the progression of cutting forces with 30% more accuracy than without addressing the tool changes.

ACKNOWLEDGEMENTS

I would like to acknowledge Bryan Dods, Dr. Gitahi Mukira, and others within GE Energy for engaging Clemson University's International Center for Automotive Research (CU-ICAR) in their endeavors to expand the knowledge associated with machining nickel-based superalloys. This research would not have been possible without the support, on many levels, from them. I would also like to acknowledge Dr. Thomas Kurfess and Dr. Cristina Bunget for patience, guidance, and encouragement during this research. I would also like to acknowledge my committee members and the entire faculty and staff at CU-ICAR for being invaluable resources along this journey. Finally, I would like to acknowledge my wife and children for inspiration and support.

TABLE OF CONTENTS

	Page
ABSTRACT	ii
ACKNOWLEDGEMENTS	iii
LIST OF TABLES	vi
LIST OF FIGURES	vii
LIST OF NOMENCLATURE	xiv
 CHAPTER	
I. INTRODUCTION	1
Problem Statement	1
Research Objective.....	3
II. BACKGROUND	5
Cast γ' -strengthened Nickel-based Superalloys	5
Milling Process.....	9
Experimental Setup and Data Collection	15
Machinability	24
Tool Wear.....	30
Kalman Filter.....	39
Force Modeling	45
Concluding Remarks	49
III. TOOL WEAR ESTIMATION.....	51
Determination of Wear Model	51
Experiment Design	53
Estimation from Probe Measurements	55
Concluding Remarks	73
IV. ADAPTIVE TOOL WEAR ESTIMATION.....	74
Derivation of Specific Kalman Filter Equations	74
Results and Discussion.....	77
Concluding Remarks	80

Table of Contents (Continued)

	Page
V. FORCE MODEL DEVELOPMENT	82
Investigate Feasibility of Mechanistic Force Model	82
Incorporate Wear into the Force Model	94
New Approach for an Updated Model	98
Concluding Remarks	102
VI. VALIDATION OF THE NEW MODEL APPROACH	103
Results and Discussion	104
Concluding Remarks	115
VII. SUMMARY AND CONCLUSIONS	117
Contributions	118
Impact of Research	119
Bounds of Applicability	120
Recommendations	121
APPENDICES	123
A: Force Estimation Using Touch Probes	124
B: Model Results for Each Pass of Tests 1-3	130
C: Kalman Filter Matlab Code	144
D: NC Program for Tests	146
E: Force Modeling Matlab Code	156
REFERENCES	158

LIST OF TABLES

Table	Page
2.1 Google scholar search results.	5
2.2 Measurement specifications of Kistler 9257B dynamometer [16].	17
2.3 Measurement specifications of the Kistler 5070A amplifier [17].	17
2.4 Critical machine specifications for the Okuma MB-46VAE [18].	21
2.5 Dimesions of cutting tool [23].	23
2.6 Insert dimensions [23].	24
2.7 Cutting parameters for machinability tests.	25
2.8 Factors and levels for the DOE conducted on the nickel-based superalloys.	28
3.1 Cutting parameters for tool wear test.	55
3.2 Truncated raw touch probe data from tool wear tests.	59
3.3 Processed tool setting touch probe data.	59
5.1 Cutting parameters for the Aluminum slot milling tests.	87
5.2 Cutting parameters for the Steel slot milling tests.	88
5.3 Cutting force coefficients for Aluminum slot tests.	89
5.4 Cutting force coefficients for steel slot milling tests.	90
5.5 Cutting parameters for the slot milling tests performed on the nickel-base superalloy.	91
5.6 Cutting coefficients for superalloy (test 1).	92
5.7 Cutting parameters for.	95
6.1 Improved wear estimates from Kalman filter.	103
6.2 Model coefficients for updated force model.	104

LIST OF FIGURES

Figure	Page
1.1 Machinability rankings for two classes of nickel-based superalloys relative to 304 stainless [2].....	2
2.1 Yield strength comparison of γ and γ' phases [7]	7
2.2 Yield strength for a γ' -strengthened nickel-based superalloy over a range of temperatures [8].....	8
2.3 Top and side views of climb milling process.	10
2.4 Top view of milling tool in a (a) conventional milling and (b) slot milling process.....	10
2.5 Typical subsurface damage [15].....	13
2.6 Source of run-out from offset tool.....	14
2.7 Source of run-out from insert location errors.	14
2.8 Diagram of experimental setup including example of post- processed data.....	15
2.9 Actual experimental setup of machine tool, dynamometer, and data acquisition system.	16
2.10 Forces on the tool in the normal (n), tangential (t), x-, and y- directions.	19
2.11 Force component in x-direction for second aluminum slot milling test with the average force overlaid.	20
2.12:Model of Okuma MB46-VAE indicating axis movement directions [18].	21
2.13 (a) Tool setting touch probe and (b) spindle touch probe.....	22
2.14 Cutting tool shape with dimensions [23].....	23
2.15 Insert shape with dimensions [23].....	23
2.16 Machinability rankings for two classes of nickel-based superalloys relative to 304 stainless [2].....	25
2.17 Resultant of the measured cutting forces when milling a γ' - strengthened nickel-based superalloy, Inconel 718, and 304 stainless steel under identical cutting conditions.....	26

List of Figures (Continued)

Figure	Page
2.18 Measured spindle power when milling a γ' -strengthened nickel-based superalloy, Inconel 718, and 304 stainless steel under identical cutting conditions.....	27
2.19 Cutting forces for the ‘high’ parameter tests conducted on three cast γ' -strengthened nickel-based superalloys.....	29
2.20 Cutting forces for the ‘low’ parameter tests conducted on three cast γ' -strengthened nickel-based superalloys.....	29
2.21 Sketches of (a) flank wear, (b) crater wear, (c) chipping, (d) flaking, (e) cracks, and (f) catastrophic failure [29].	31
2.22 Crater wear on tool with cross-section.	33
2.23 Multiple views of flank wear.....	34
2.24 Two-dimensional representation of tool cutting the workpiece indicating contact zones.....	35
2.25 Flank face forces in Teitenberg wear model [41].	37
2.26 Generalization of standard tool wear curve.....	37
2.27 Orthogonal cutting model proposed by Merchant [85].	47
2.28 (a) J-C prediction and measured flow stress for Inconel 718, (b) Predicted using the new model and measured yield stress for IN100 [11].	48
2.29 Typical results of a finite element simulation [89].	49
3.1 Generalized wear model on a typical wear curve.....	52
3.2 Schematic of the test cuts.	53
3.3 Flow chart of the cutting experiment.....	54
3.4 The insert and tool geometry at the bottom of the cutting edge.	56
3.5 A worn insert depicting flank wear and the probe measurement.	56
3.6 Sketch of cross-section of bottom of insert with wear progression and viewing angles.	57
3.7 Picture of tool’s end wear showing measurement location.	58

List of Figures (Continued)

Figure	Page
3.8 Flank wear versus the volume of material removed.....	60
3.9 Wear rate comparison between a γ' -strengthened nickel-based superalloy and AISI 4340 Steel.	61
3.10 Change in measured tool length from pass-to-pass during tool wear tests.	62
3.11 Four general scenarios of cutter run-out.....	63
3.12 Top, front, and side views of a machined pass showing changes due to tool wear.	64
3.13 Uncut chip thicknesses when run-out is present.....	66
3.14 Resultant cutting forces for three tool rotations during pass 1 of Test 1 and Test2.....	68
3.15 Resultant cutting forces for three tool rotations during pass 5 of Test 1 and Test2.....	69
3.16 Microscope measurements and error bar plot of VB estimates from probe measurements.	70
3.17 Microscope measurements and error bar plot of VB estimates from probe measurements with new correlation factor.	71
4.1 Results of the Kalman filter on the data from Test 1.....	78
4.2 Results of the Kalman filter on the data from Test 2.....	79
4.3 Results of the Kalman filter on the data from Test 3.....	79
5.1 Tool engaging the workpiece.	82
5.2 Normal and tangential forces on the cutter.....	83
5.3 Sketch of slot milling process.....	84
5.4 Graph showing a_1 and a_0	87
5.5 Average force versus feed per tooth for Aluminum.	88
5.6 Model on real data for three tool rotations during slot milling of Aluminum (test 3).....	89

List of Figures (Continued)

Figure	Page
5.7 Average force versus feed per tooth for Steel.	90
5.8 Model on real data for three tool rotations during slot milling of Steel (test 3).	91
5.9 Average forces versus feed per tooth for each slot milled in the superalloy.	92
5.10 Model on real data for three tool rotations during milling of superalloy (beginning).	93
5.11 Model on real data for three tool rotations during milling of superalloy (end).	94
5.12 Average cutting forces during the fourth nickel-based superalloy test.	95
5.13 Flow chart for determining tool wear effect on force coefficients.	96
5.14 Change in chip area and edge effect coefficients with respect to volume of material removed.	97
5.15 Wear progression in relation to the cutting action.	100
5.16 The effect of tool wear progression on chip size.	100
5.17 Plot of model components when the tool is (a) new and (b) worn.	101
6.1 Cutting forces in the normal (n), tangential (t), x-, and y- directions.	105
6.2 Comparison of average measured and modeled cutting forces as a function of volume of material removed for Test 1.	106
6.3 Comparison of average measured and modeled cutting forces as a function of volume of material removed for Test 2.	106
6.4 Comparison of average measured and modeled cutting forces as a function of volume of material removed for Test 3.	107
6.5 Corner radius and depth of cut notches.	108
6.6 Insert comparison from the eighth pass of the second and third test.	109
6.7 Statistical analysis of tangential cutting forces.	110

List of Figures (Continued)

Figure	Page
6.8 Statistical analysis of normal cutting forces.....	111
6.9 Comparison of model without tool wear compensation.....	112
6.10 Modeled and measured x- and y-direction cutting forces for three tool rotations in the first pass of the first test.....	113
6.11 Modeled and measured x- and y-direction cutting forces for three tool rotations in the fourth pass of the first test.	114
6.12 Modeled and measured x- and y-direction cutting forces for three tool rotations in the seventh pass of the first test.....	114
6.13 Flow chart for implementing the methodology presented.....	116
7.1 Necessary inputs for in-process estimations of subsurface damage.....	122
A.1 Sketch of tool deflection while cutting.....	125
A.2 Example results from a finite element simulation.	125
A.3 Error bar plot of y-direction forces with estimations from probe analysis.	129
B.1 Modeled forces compared to measured forces for the first pass of test 1.....	130
B.2 Modeled forces compared to measured forces for the second pass of test 1.	131
B.3 Modeled forces compared to measured forces for the third pass of test 1.	131
B.4 Modeled forces compared to measured forces for the fourth pass of test 1.	132
B.5 Modeled forces compared to measured forces for the fifth pass of test 1.....	132
B.6 Modeled forces compared to measured forces for the sixth pass of test 1.	133
B.7 Modeled forces compared to measured forces for the seventh pass of test 1.	133

List of Figures (Continued)

Figure	Page
B.8 Modeled forces compared to measured forces for the eighth pass of test 1.	134
B.9 Modeled forces compared to measured forces for the first pass of test 2.....	135
B.10 Modeled forces compared to measured forces for the second pass of test 2.	135
B.11 Modeled forces compared to measured forces for the third pass of test 2.	136
B.12 Modeled forces compared to measured forces for the fourth pass of test 2.	136
B.13 Modeled forces compared to measured forces for the fifth pass of test 2.....	137
B.14 Modeled forces compared to measured forces for the sixth pass of test 2.	137
B.15 Modeled forces compared to measured forces for the seventh pass of test 2.	138
B.16 Modeled forces compared to measured forces for the eighth pass of test 2.	138
B.17 Modeled forces compared to measured forces for the first pass of test 3.....	139
B.18 Modeled forces compared to measured forces for the second pass of test 3.	140
B.19 Modeled forces compared to measured forces for the third pass of test 3.	140
B.20 Modeled forces compared to measured forces for the fourth pass of test 3.	141
B.21 Modeled forces compared to measured forces for the fifth pass of test 3.....	141
B.22 Modeled forces compared to measured forces for the sixth pass of test 3.	142

List of Figures (Continued)

Figure	Page
B.23 Modeled forces compared to measured forces for the seventh pass of test 3.	142
B.24 Modeled forces compared to measured forces for the eighth pass of test 3.	143

LIST OF NOMENCLATURE

γ : Alloy matrix

γ' (gamma prime): Strengthening phase of the alloy

Δb : Change in depth-of-cut

ΔL : Change in tool length measured with a tool setting touch probe

$\Delta L_{A,B}$: Difference of cutting length from insert A to insert B

ΔL_{TW} : Change in tool length measurement made with the tool set station

$\Delta r_{A,B}$: Difference of cut radius from insert A to insert B

ΔSP : Change in the depth of cut which is measured with the spindle probe

ΔTS : Change in tool length measured by the tool set station

ΔV_{MR} : Change in volume of material removed from one cutting pass to the next

$\delta_{y,max}$: Maximum beam deflection in the y-direction

δ_z : Beam deflection in the z-direction

ε : Equivalent plastic strain in Johnson-Cook model

$\dot{\varepsilon}$: Equivalent plastic strain rate in Johnson-Cook model

$\dot{\varepsilon}_0$: Reference equivalent plastic strain rate in Johnson-Cook model

θ : Cutter rotation angle

θ_e : Cutter angle at the end of an individual tooth engagement.

θ_j : Temperature at the interface between the tool and the workpiece

θ_{max} : Maximum deflection angle of a cantilevered beam with a point load applied to the beam's tip

θ_s : Cutter angle at the start of an individual tooth engagement.

λ_s : Inclination angle of cutting tool

ν_{TP} : Tooth passing frequency

σ : Equivalent flow stress in Johnson-Cook model

List of Nomenclature (Continued)

$\sigma_{TS}^2 | \sigma_m^2 | \sigma_p^2 | \sigma_{VB}^2 | \sigma_{VB'}^2$: Variance of the tool setting touch probe, total measurement, power measurement, process variance with regards to flank wear, and process variance with regards to rate of flank wear change

τ : Time for 180° of tool rotation

Ψ : Angle of lower edge of cutting tool

a_a : Axial depth of cut used in Alauddin et al. model.

A : Papazafiriou, et al. model constant which depends on the tool and workpiece material

A : Designator for insert A in run-out discussion

A : Matrix that relates previous state to current state in Kalman Filter

a_l : The slope of a line which is fit to the average force versus feed per tooth points from the measured data

a_0 : The theoretical cutting force at a feed per tooth of zero

B : Designator for insert B in run-out discussion

b and a_p : Axial depth of cut

b_s : Length of insert's minor cutting edge

C : Empirical constant within the Taylor tool life equation that depends on tool and workpiece properties, as well as cutting parameters.

dA_f : Change in the area of the flank wear.

d_c (D_c): Cutting diameter of tool

$d\vec{F}_{nf}$: Change in the normal flank force.

$d\vec{F}_{ff}$: Change in the friction flank force.

dm_m : Diameter of tool's shank

DOC_r : Radial depth of cut

E : Young's modulus

e : Error between actual process state and estimated state

F : Cutting force

List of Nomenclature (Continued)

\bar{F} : Average cutting force

$f | f_{rev} / ft$: Feed rate of the tool (distance per time | distance per revolution | distance per tooth)

\hat{F}_{ta} : Predictive average tangential cutting force

f_z : Feed per tooth used in Alauddin et al. model.

$g(\theta)$: Force model switching function

H: Measurement correlation to states in the Kalman filter

h : Uncut chip thickness

I : Relative machinability index

iW : Width of insert

L : Tool stick-out length

l_1, l_2 , and l_3 : Tooling supplier geometry nomenclature

l_a : Length of insert's major cutting edge

l_e : Length of the edge that is in contact with the material

K: Kalman gain at the current time step

K : Specific cutting force (force per unit of chip area) for the semi-empirical cutting force model.

k : Discrete time step indicator for Kalman filter.

$k, k-1$: Current time step with respect to information from previous time step (*a priori*)

K_d : Papazafiriou, et al. model constant which depends on the tool and workpiece material

K_{ff} : Teitenberg's model, flank pressure parameters

K_{nf} : Teitenberg's model, friction parameters

$k_n | k_t | k_a | k_{ne} | k_{te} | k_{ae} | k_A | k_{e,l} | k_{e,vB}$: Normal, tangential, axial, normal edge-effect, tangential edge-effect, axial edge-effect, chip area, edge length, and flank wear specific cutting forces

k_y : Beam stiffness in the y-direction

m : Designator for current material being analyzed in relative machinability rankings

List of Nomenclature (Continued)

MSE : Mean square error

N : Cutter rotational speed

n , and t : Normal and tangential direction indicators

n : Empirical constant within the Taylor tool life equation that depends on tool and workpiece properties, as well as cutting parameters.

\vec{n}_f : Unit vector in the normal direction.

N_t : The number of teeth on the cutter

\mathbf{P} : The error covariance.

P_y : Load applied to a cantilevered beam

\mathbf{Q} : Process noise covariance

\mathbf{R} : Covariance in the measurement

r_e : Insert's corner radius

r_{tool} : Radius of the tool

re : Radial engagement (%) of cutter in workpiece

ref : Designator for reference material in the relative machinability rankings

res : Resultant

s : Depth of insert

single: Designator for wear parameters in regards to a single insert

T : Time of useful tool life in the Taylor tool life equation.

T : Workpiece temperature in the Johnson-Cook model

T_m : Material melting temperature in Johnson-Cook model

T_r : Room temperature in Johnson-Cook model

t : Time

t_{eq} : Time at which cutter run-out equalizes

$\text{tr}(\mathbf{A})$: Trace of matrix \mathbf{A}

List of Nomenclature (Continued)

V : Cutting speed used in the Taylor tool life equation.

VB : Size of flank wear

VB' : Rate of change in flank wear size

VB_{corr} : Correlation factor between the tool set station measurement and the tool's flank wear

VB_0 : "Initial" flank wear for tool wear model

V_{MR} : Cumulative volume of material removed

vc : Cutting speed

x -, y -, and z :- Orthogonal direction indicators

$x(t)$: Distance as a function of time

\mathbf{v} : Measurement noise

\mathbf{w} : Process noise

\mathbf{x} : Vector of states used in Kalman filter

$\hat{\mathbf{x}}$: Kalman filter state estimate

\mathbf{z} : Measurements used in Kalman filter

CHAPTER ONE

INTRODUCTION

Nickel-based superalloys are specially designed for applications where high strength, creep resistance, and oxidation resistance are critical at high temperatures. Many of their applications are in the hot gas sections of turbo-machinery (e.g., jet engines, gas turbines, and turbochargers for internal combustion engines). With greater demands on the performance and efficiency of these types of machines, the firing temperatures are reaching higher levels and nickel-based superalloys are being utilized more because of their excellent mechanical qualities at extreme temperatures. However, the properties that make them attractive for these applications present difficult challenges for the manufacture, particularly machining, of the components that are made from these materials. Considering the extreme environments that these components operate in, part quality, in particular surface quality, is paramount. The damage and stresses imparted on the surfaces of these components during manufacture needs to be well understood and controlled in order to ensure that premature component and machine failures do not occur.

Problem Statement

Very little research has been conducted on machining nickel-based superalloys and even less has been conducted in regards to milling cast γ' -strengthened nickel-based superalloys [1]. To illustrate the difference in machining these materials, a graph of relative machinability rankings for two different categories of nickel-based superalloys is shown in relation to stainless steel 304 in Figure 1.1. Lower relative machinabilities indicate that the measured values of power, force, and tool wear were all greater than that measured for the stainless steel. Thus, a lower machinability indicates that a material is more difficult to machine. More details on the

data gathered and calculations made in the determination of the machinability indexes are presented in the Background chapter.

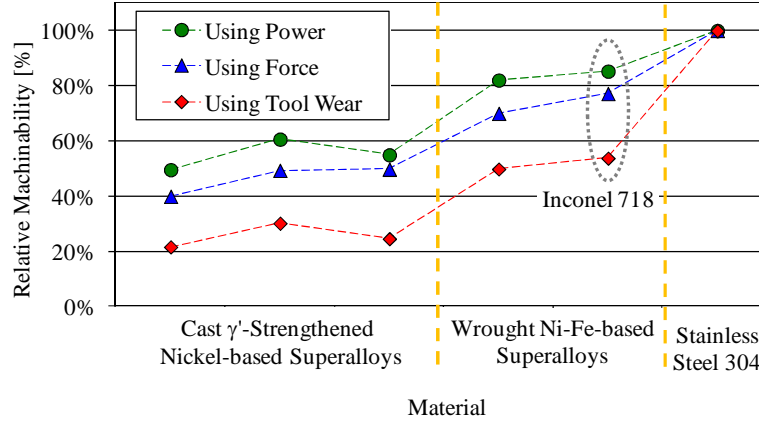


Figure 1.1: Machinability rankings for two classes of nickel-based superalloys relative to 304 stainless [2].

Tool wear is a stochastic process and significant errors can result from a purely model based estimation. This is true when machining any material but when machining very difficult to machine alloys, such as γ' -strengthened nickel-based superalloys, the errors become exacerbated. The time scale for determining the tool's wear state and reacting are much shorter for these lower machinability alloys. Incorporating a method of measuring the tool wear would capture unexpected shifts, or errors, in the wear state. Various methods exist for measuring tool wear and will be discussed in the Background chapter. Combining a tool wear model with a measurement method in an adaptive approach (i.e., Kalman filter) provides a robust and accurate method for determining wear at any point in the tool's life.

Typically, when modeling forces, tool wear is either assumed to be negligible or quasi-constant. It is shown throughout this work that these assumptions are valid for common materials,

such as steel or aluminum but does not apply to cast γ' -strengthened nickel-based superalloys. Therefore, it is necessary to incorporate tool wear. Typically when tool wear is incorporated into a force model, it is done with an empirical relationship and parameters that do not necessarily have physical meaning. However, an alternative model proposed in the Force Model chapter includes geometric parameters of tool wear that are updated as the tool is used.

Research Objective

Subsurface damage is critical to the quality of γ' -strengthened Nickel-based superalloy components due to the extreme environments that these components operate in. Cutting forces and temperatures are crucial for predicting the amount of subsurface damage imparted on a workpiece after machining. Cutting forces also provide insight into power usage, tool condition, and the mechanisms of material removal. Also, commercial measurement equipment is readily available and able to be implemented into the operation without disturbing the natural cutting process. Therefore, cutting forces were the primary focus of this work. Current cutting force models do not consider the extreme tool wear that occurs when milling γ' -strengthened Nickel-based superalloys. The objective of this research was to develop a robust and accurate wear estimation method in conjunction with an updated milling force model which can be applied to γ' -strengthened nickel-based superalloys and developed for process control, in the future.

The research objective was broken into several components. The first was to investigate a viable on-machine wear estimation technique and relate the wear to the physical changes of the tool. This technique integrates commonly available machine capabilities with accepted wear modeling practices in an adaptive approach. Next an applicable force model was determined. This model is based on physical principles rather than strictly on empirical relationships in order to provide a more fundamental understanding of the cutting mechanics in milling. However, this

model is not entirely analytical due to the large number of variables (e.g., material properties, cutting tool geometry, cutting tool materials, machine tool variations, and cutting fluids) in milling and their complex interactions. A purely analytical model would also be computationally intense and would not be conducive to real-time implementation in a control strategy in the future. Finally, the physical tool change estimates were integrated into the new force model and the applicability was demonstrated on experimental data.

CHAPTER TWO

BACKGROUND

Tool wear and cutting forces have been researched extensively for many years. However, much of the work has been conducted in regards to turning, as opposed to milling. Very little research has been conducted on nickel-based superalloys and most of this research was conducted on Inconel 718. Very few articles were found in regards to milling cast γ' -strengthened nickel-based superalloys. This research gap is illustrated by the data in Table 2.1. These data were collected by performing a series of searches on Google Scholar [3]. This example is not intended to be a definitive representation of the works available. The statement being made is that as the search was refined, the number of results significantly decreased. Of the 45 results for the final search, only two were relevant to milling cast γ' -strengthened nickel-based superalloys. Both are machinability reviews published in 1998 and 2003 [4,5]. Process models specific to these materials have not been developed. This chapter presents the concepts discussed in this work and the research that has been conducted in the fields related to the objectives of this work.

Table 2.1: Google scholar search results.

Search Criteria	Number of Results
Machining	941,000
Machining Turning	161,000
Machining Milling	148,000
Machining Nickel-based superalloy	4,800
Machining milling Nickel-based superalloy	1,430
Machining milling cast gamma prime Nickel-based superalloy	45

Cast γ' -strengthened Nickel-based Superalloys

This subsection gives a brief overview of the history of nickel-based superalloys, the microstructure aspects that give them their qualities, and the effect of these qualities on tool

performance. The book, *Superalloys II*, and the nickel-based superalloy machinability reviews by Ezugwu, et. al. (1999 and 2003) are excellent sources for a more detailed review of the material presented here [4-6]. Superalloy development has progressed in conjunction with aircraft engine and gas turbine technology since the early 1900s. The earliest superalloys were primarily iron- or nickel-based and in the 1930s iron's usage declined giving way to nickel and cobalt due to their favorable FCC structure formation. Nickel-based superalloys were initially only used in the wrought condition and were used in turbines as far back as the 1940s. In the 1950s, vacuum melting allowed the addition of more hardening elements and the removal of undesirable alloy impurities which led to the development of higher strength materials. These alloys were not able to be forged as their predecessors were because of their strength. So, they were cast into rough shape via investment casting. Since that time, chemistry compositions, casting techniques, and post-casting heat-treatment processes have paved the way for more advancement in the properties of these materials [4,6].

The microstructure of these alloys consists of an alloy matrix (γ), a strengthening gamma prime (γ') phase, carbides, borides, and topologically close packed (TCP) phases. Carbides represent a small percentage of the microstructure because of a relatively low carbon percentage and they typically exist along grain boundaries within nickel-based superalloys. Researchers believe that the carbides are beneficial for high temperature rupture strength and creep resistance. Precipitation hardening is a primary means of strengthening nickel-based superalloys and γ' precipitation is the primary goal. The γ' phase is comprised of nickel, aluminum, and titanium and is beneficial because it exhibits high strength, helps prevent dislocation movement, and its strength actually increases as temperature goes up. The temperature behavior of the γ' phase is shown in Figure 2.1 [6,7].

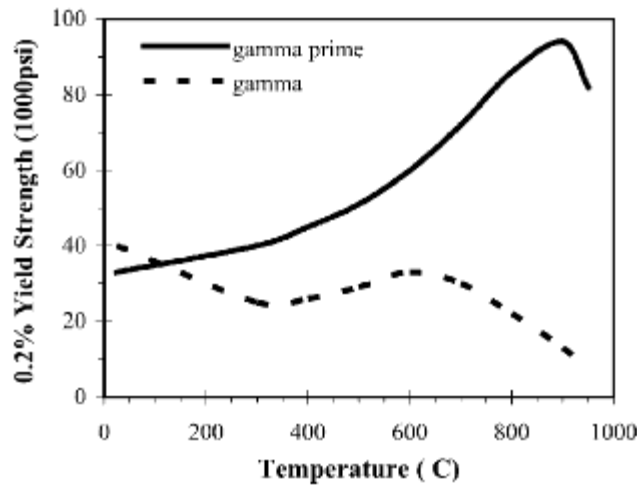


Figure 2.1: Yield strength comparison of γ and γ' phases [7]

The change in alloy strength over a range of temperatures is shown Figure 2.2. Figure 2.2 shows that the material maintains its strength over a broad temperature range and its strength actually increases at high temperatures. High stresses and temperatures are imparted on the cutting tool while machining these alloys because of the high strength of these materials at the elevated temperatures of machining and their low thermal conductivity. These effects exacerbate the breakdown of the tool in milling because the tool undergoes thermal and mechanical shock due to the interrupted nature of the milling process. In addition, the carbides in the alloys act as an abrasive. Each of these factors is detrimental to a cutting tool and contributes to the low machinability of cast γ' -strengthened nickel-based superalloys [4,6].

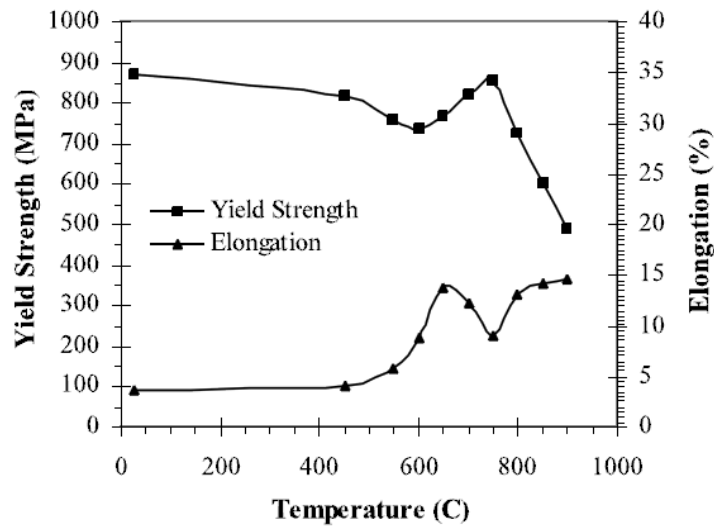


Figure 2.2: Yield strength for a γ' -strengthened nickel-based superalloy over a range of temperatures [8].

Many different chemical compositions exist within cast nickel-based superalloys but the primary elements are nickel, chromium, molybdenum, aluminum, titanium, and carbon. Cobalt, tungsten, tantalum, columbium, boron, and zirconium are also used to varying degrees. As mentioned, earlier superalloys also used a significant amount of iron. Each element has an important role to play but aluminum is particularly vital to the alloy because it helps form a protective oxide and γ' . Carbon's role is not as straightforward because certain carbides were found to have unfavorable effects on ductility but in certain alloys reducing carbon led to reductions in creep life and ductility. Titanium is commonly used as a replacement for some aluminum in the γ' phase[4,6].

Milling Process

Milling is a traditional method of material removal which shapes a workpiece in order to achieve target geometry. It is, and will remain, a significant operation in most manufacturing operations. When compared to other material removal methods, it is relatively inexpensive and productive with the potential for high quality output. With multi-axis machine tools, it also has the ability to create complex geometry parts.

Process Definition

Milling involves a rotating cutter with multiple teeth engaging a workpiece repeatedly in order to remove material. A typical milling operation is shown in Figure 2.3. This figure depicts an indexable-insert milling cutter. In this case, the cutting edges are formed on removable inserts. When the cutting edge becomes worn to the point that the cutting performance becomes unpredictable or part quality suffers, the inserts are replaced. There are many variations of milling cutters and this is only one example. This figure also depicts a climb/down milling process. In climb milling, the uncut chip thickness (h) is greater in the beginning of the cut than in the end of the cut and it is a function of the cutter rotation angle (θ). The alternatives to climb milling are conventional/up milling or slot milling. In conventional milling, the uncut chip thickness is greater at the end of the cut than at the beginning. In slot milling, the uncut chip thickness is small at the beginning and end. These alternative milling processes are shown in Figure 2.4.

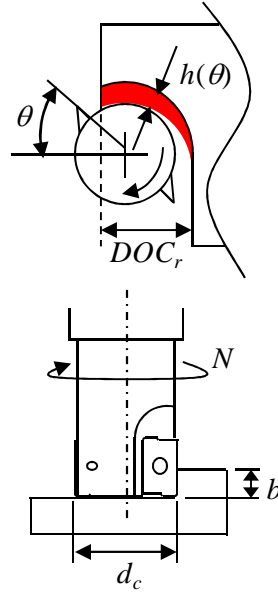


Figure 2.3: Top and side views of climb milling process.

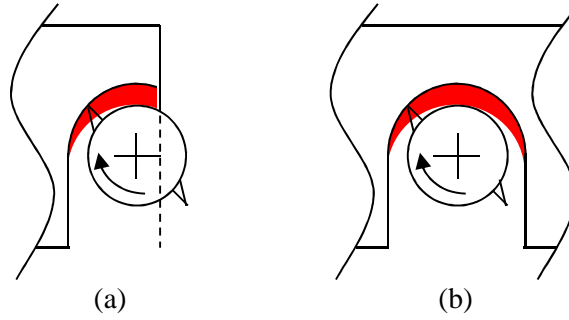


Figure 2.4: Top view of milling tool in a (a) conventional milling and (b) slot milling process.

To define a milling operation, the cutting speed (v_c), feed per tooth (f_t), axial depth of cut (b), and radial engagement (re) need to be specified. The cutting speed is the velocity of the cutting edge at the radius of the tool. The cutter rotational speed (N), in revolutions per minute (rpm), is therefore a function of the cutting speed. This is shown in equation (2.1),

$$N = \frac{v_c}{\pi d_c} \quad (2.1)$$

where d_c is the cutting diameter of tool which is shown in Figure 2.3. The feed per tooth is the maximum uncut chip thickness (h). The radial engagement is typically specified as a percentage which is the ratio of the width of the cut to the diameter of the tool. This is shown in equation (2.2),

$$re = \frac{DOC_r}{d_c} \cdot 100\% . \quad (2.2)$$

Therefore, the cut in Figure 2.3 has ~60% radial engagement. A full slot is 100% radial engagement.

When programming a machine tool, typical programming inputs are the coordinates of the tool's centerline at its end, cutter rotational speed, and the feed rate of the tool with respect to the workpiece (f). The feed rate is the distance per time at which the centerline of the tool moves. To determine this feed rate, the feed per tooth is multiplied by the number of teeth (n_t) to give the feed per revolution (f_{rev}) and then this value is multiplied by the rotational speed to determine the distance traveled per unit of time. The feed per revolution relationship is shown in equation (2.3),

$$f_{rev} = f_t \cdot n_t , \quad (2.3)$$

and the feed rate relationship is shown in equation (2.4),

$$f = f_{rev} \cdot N . \quad (2.4)$$

The uncut chip thickness is dependent on the feed per tooth and is shown as a function of cutter rotation angle for tooth j in equation (2.5),

$$h(\theta_j) = f_t \sin(\theta_j) g(\theta_j) , \quad (2.5)$$

where $g(\theta_j)$ is a switching function that is one when a tooth is engaged in the material and zero when no tooth is engaged. The switching function is shown in equation (2.6),

$$g(\theta_j) = \begin{cases} 1, & \text{when } \theta_s \leq \theta_j \leq \theta_e \\ 0, & \text{when } \theta_j < \theta_s, \theta_e < \theta_j \end{cases}, \quad (2.6)$$

where θ_s and θ_e are the angles when a tooth starts to engage in the cut and ends the engagement, respectively [9]. Since the cutter rotation angle is related to time by the cutter rotational speed, it can also be written as a function of time as shown in equation (2.7),

$$\theta(t) = 6Nt, \quad (2.7)$$

where time is in seconds and 6 is the necessary conversion factor from revolutions per minute to degrees per second. Using the relationship in equation (2.7), the uncut chip thickness is shown as a function of time in equation (2.8)

$$h(t) = f_t \sin(6Nt) g(t). \quad (2.8)$$

Process Considerations

Any material removal process has an effect on the material of the final component. In regards to milling nickel-based superalloys, surface quality (i.e., subsurface damage) is paramount due to the extreme environments that these components operate in. Subsurface damage is critical to part quality because the damage gives the material at the surface different properties than the bulk material and leads to unpredictable behavior of the finished part [10,11]. An image of typical subsurface damage is shown in Figure 2.5. The most accurate way to detect this subsurface damage is through destructive testing after a part has been machined. Since this is not possible on components which are to be used in an actual application, there needs to be a means of understanding the mechanisms which contribute to generation of the damage and control them. Cutting forces and temperature are key components of subsurface damage generation [12-14].

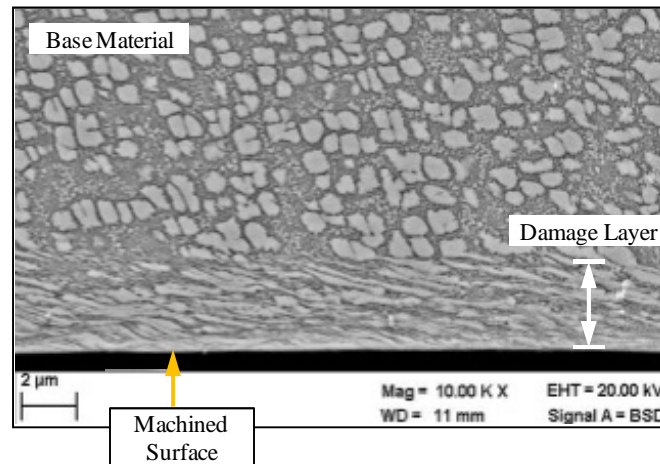


Figure 2.5: Typical subsurface damage [15].

Cutter run-out is a common occurrence in milling. It is present when one tooth sweeps a larger diameter or protrudes lower from the bottom of the tool than the other(s). This results in one tooth bearing a greater amount of the machining load than the other tooth/teeth. Run-out is a by-product of milling that can be minimized but is very difficult to eliminate, especially with an inserted cutter. Figure 2.6 illustrates run-out and errors due to tool holding system. The set screw that holds the cutter in position pushes on the cutter body and induces differences between the cutting teeth. Figure 2.7 illustrates the errors that can occur due to the installation and location of inserts in the cutter body. The run-out depicted in Figure 2.6 is minimized by using a holder that will center the tool (e.g., hydraulic, heat-shrink, or collet holders). The run-out depicted in Figure 2.7 is minimized through the use of precision pre-setters. A pre-setter is an additional piece of equipment that is separate from the machining center and is used to inspect the tool before inserting it into the machine. This equipment allows run-out in the inserts to be detected and adjusted prior to machining. Some run-out is unavoidable due to tolerances of the tooling.

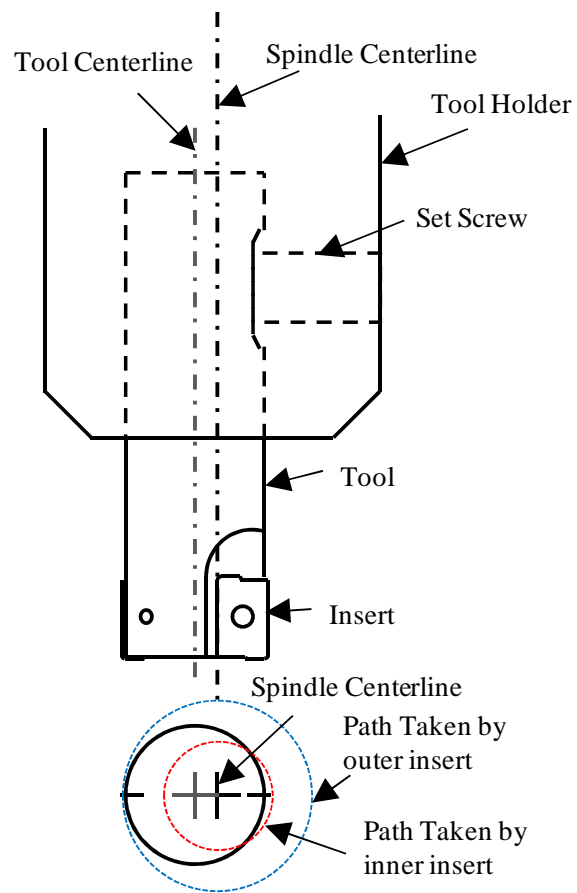


Figure 2.6: Source of run-out from offset tool.

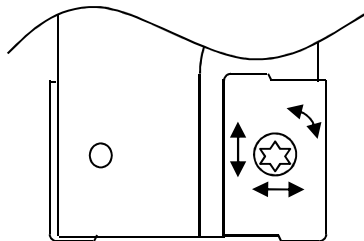


Figure 2.7: Source of run-out from insert location errors.

Experimental Setup and Data Collection

An empirical tool wear model and a semi-empirical cutting force model are investigated in this research. Therefore, milling tests have been conducted and data has been collected for the development and validation of these models and this approach. A diagram of the setup for the cutting tests is shown in Figure 2.8 and real pictures of the equipment and lab setup are shown in Figure 2.9. A Kistler 9257B three-component piezoelectric force dynamometer was mounted on the table of an Okuma, MB46 VAE, three-axis milling machine. The workpiece was clamped on the table of the dynamometer, as shown in Figure 2.9. The signals from the piezoelectric crystals were sent to a Kistler 5070A charge amplifier and the amplified signal was transmitted to an analog to digital (A/D) converter PC card (DAS16/16) in a computer running Dynoware software. The Dynoware software recorded the force data from the A/D converter. The x-, y-, and z-components of force were recorded and then exported to a tab-delimited text file. The text files were then imported into Matlab for post-processing. During post-processing the raw data were analyzed to understand the forces generated by each individual tooth passing and the data were also filtered to determine the average forces.

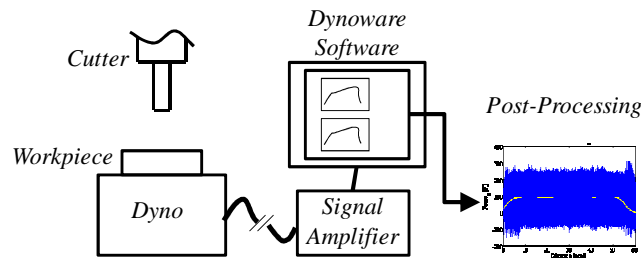


Figure 2.8: Diagram of experimental setup including example of post-processed data.

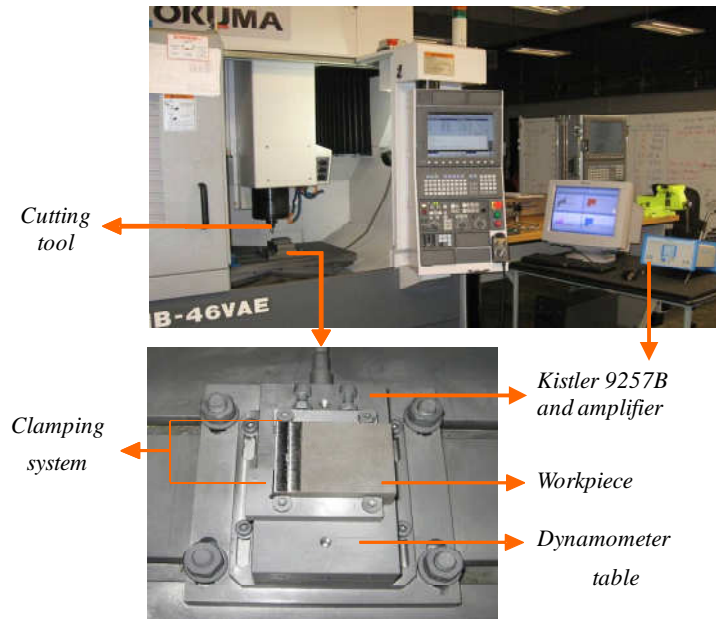


Figure 2.9: Actual experimental setup of machine tool, dynamometer, and data acquisition system.

The measurement specifications for the Kistler dynamometer are shown in Table 2.2. These specifications show that the dynamometer is capable of measuring forces with magnitudes up to 5000 N in the x- and y-direction and 10,000 N in the z-direction. The output of the piezoelectric crystals in the dynamometer is a charge which is proportional to a force applied to the crystals. The linearity specification indicates that the output charge is linear with the input force within $\pm 1\%$ of the full-scale output (FSO) of the device. The hysteresis specification indicates that difference in charging and discharging will be within $\pm 0.5\%$ of the FSO. The cross talk specification indicates that when a force is applied in one direction it will affect the measurements in other directions by $\pm 2\%$ or less. The sensitivities indicate the amount of charge, in picocoulombs, that the piezoelectric crystals will output per unit of force, in Newtons, input.

Table 2.2: Measurement specifications of Kistler 9257B dynamometer [16].

Criteria	Units	Value
Range (F_x, F_y)	kN	-5 - +5
Range (F_z)	kN	-10 - +10
Linearity	%FSO	$\leq \pm 1$
Hysteresis	%FSO	$\leq \pm 0.5$
Cross talk	%	$\leq \pm 2$
Sensitivity (F_x, F_y)	pC/N	$\cong -7.5$
Sensitivity (F_z)	pC/N	$\cong -3.7$

The measurement specifications for the Kistler charge amplifier are shown in Table 2.3. The range of input that the amplifier is specified for is $\pm 200 - 200,000$ pC. The typical error of the measurement due to the amplifier is less than $\pm 0.3\%$ and the maximum error is less than $\pm 1\%$. The measurement drifts at a rate less than ± 0.05 pC/s. This drift is due to the exponential decay of the resistor/capacitor (RC) circuit in the charge amplifier. The drift is a factor when measuring constant loads for a long period of time. The cutting forces in milling are cyclic with a short time period, therefore, the drift is not a significant factor in these measurements.

Table 2.3: Measurement specifications of the Kistler 5070A amplifier [17].

Criteria	Units	Value
Input Range	pC	$\pm 200 - 200,000$
Error typ./max.	%	$< \pm 0.3 / < \pm 1$
Drift	pC/s	$< \pm 0.05$
Frequency Range	kHz	$\cong 0 - > 45$

The data collection frequency when milling is set so that a significant amount of data points are measured for each tooth passing. The frequency of tooth passes (ν_{TP}), in Hertz (Hz), is determined using equation (2.9),

$$v_{TP} = Nn_t \left(\frac{1 \text{ min}}{60 \text{ s}} \right). \quad (2.9)$$

In order to capture data from each tooth passing and avoid aliasing, the sample rate must be at least equal to the Nyquist rate. The Nyquist rate is twice the highest frequency in the measured signal. For example, a tool with two teeth rotating at 1000 rpm has a tooth passing frequency of 33.3 Hz and the Nyquist rate is 66.6 Hz. However, the shape of the force curve for each tooth is of interest and, therefore, the sample rate is set at least 20 times the tooth passing frequency.

The dynamometer measures forces in the x-, y-, and z-directions (F_x , F_y , and F_z) and it is arranged in the milling machine such that the x-, y-, and z-measurement directions are parallel to the respective axes of movement. The x- and y-forces are shown on a milling cutter in Figure 2.10. If the cutter's angle of rotation is known, then forces can also be analyzed in the normal, F_n , direction using equation (2.10),

$$F_n = F_y \sin(\theta) + F_x \cos(\theta), \quad (2.10)$$

and tangential, F_t , directions using equation (2.11),

$$F_t = F_y \cos(\theta) - F_x \sin(\theta). \quad (2.11)$$

Cutting forces are also analyzed via the resultant, or magnitude, of the force. The resultant of the x- and y-direction forces ($F_{res,xy}$) is shown in equation (2.12),

$$F_{res,xy} = \sqrt{F_x^2 + F_y^2}, \quad (2.12)$$

and the resultant of the forces in all directions (F_{res}) is shown in equation (2.13),

$$F_{res} = \sqrt{F_x^2 + F_y^2 + F_z^2}. \quad (2.13)$$

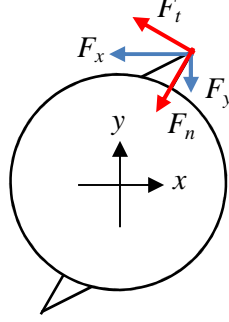


Figure 2.10: Forces on the tool in the normal (n), tangential (t), x-, and y-directions.

The data is recorded by the dynamometer with respect to time. If the feed rate, f , is constant and the tool moves along a straight path in a single direction then the distance as a function of time, $x(t)$, is calculated as shown in equation (2.14),

$$x(t) = f \cdot t. \quad (2.14)$$

If the radial emersion, re , and axial depth of cut, b , are constant, then the volume of material removed with respect to time is calculated as shown in equation (2.15),

$$V_{MR}(t) = b \cdot \frac{re \cdot d_c}{100\%} \cdot f \cdot t \quad (2.15)$$

This relationship does not apply as a milling cutter is entering or exiting the material because the radial emersion is not constant during these portions of the operation.

The raw data (recorded by the dynamometer) is often condensed by determining the mean cutting forces. The mean is obtained in this research by filtering the data in Matlab using a low order and low cut-off frequency Low-Pass Butterworth filter. The mean and raw x-force data from an aluminum slot milling test are shown in Figure 2.11.

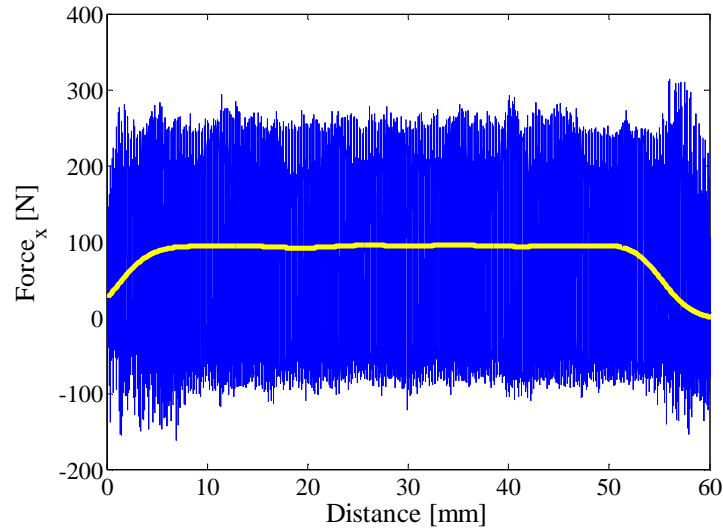


Figure 2.11: Force component in x-direction for second aluminum slot milling test
with the average force overlaid.

A model of the Okuma MB-46VAE is shown in Figure 2.12 with arrows indicating which components move and their direction of movement. The figure indicates that x- and z-axis movements are accomplished by moving the spindle, while y-axis movements are accomplished by moving the table. The critical machine specifications are shown in Table 2.4. The maximum spindle power, torque, and speed are not significant factors when machining nickel-based superalloys with carbide tooling because the tool will breakdown before machine limits are reached. However, when machining with tools such as ceramics, these machine limits must be considered because ceramic tooling is capable of machining at high speeds and high chip loads. Thus the cutting forces and therefore torque will be high at high speeds, creating the demand for high power. The spindle taper of this machine is 40° . This is significant because it dictates the type of interface between the tool holder and the spindle and thus influences the stiffness and dynamics of the tool. The positioning accuracy and repeatability are important for ensuring that

the proper part dimensions are machined and also these specifications are critical when considering the accuracy and precision of measurements made with probing.

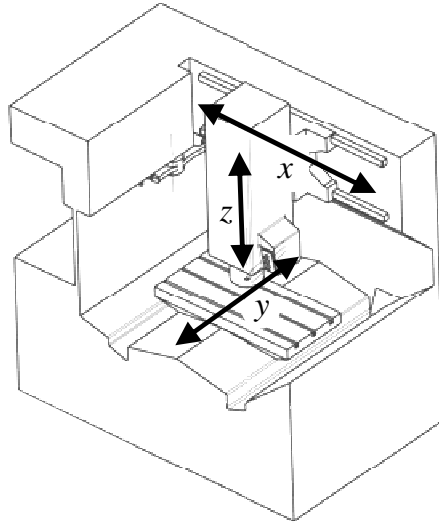


Figure 2.12: Model of Okuma MB46-VAE indicating axis movement directions [18].

Table 2.4: Critical machine specifications for the Okuma MB-46VAE [18].

Criteria	Units	Value
Max Spindle Power	kW	11
Max Spindle Speed	rpm	15,000
Max Spindle Torque	Nm	198
Spindle Taper	°	40
Positioning Accuracy	mm	± 0.003
Positioning Repeatability	mm	± 0.001

In addition to the machine tool and force sensors, touch sensors and an optical microscope were also used to make tool wear measurements. The two touch sensors were a tool setting probe and a spindle probe. They were manufactured by Renishaw. These types of probes

are shown in Figure 2.13. The tool setting probe was used to measure the length and diameter of a cutting tool. The spindle probe was used to make measurements on the surface of a workpiece. Renishaw documentation specified that the repeatability for both probes was 1 μm [19-21]. The microscope was a Dino-Lite Pro AM413ZTA. It is a 1.3M pixels handheld digital microscope with variable magnification from 10x to 50x then 200x and 220x magnifications. It also has built-in LEDs and an adjustable polarizer.

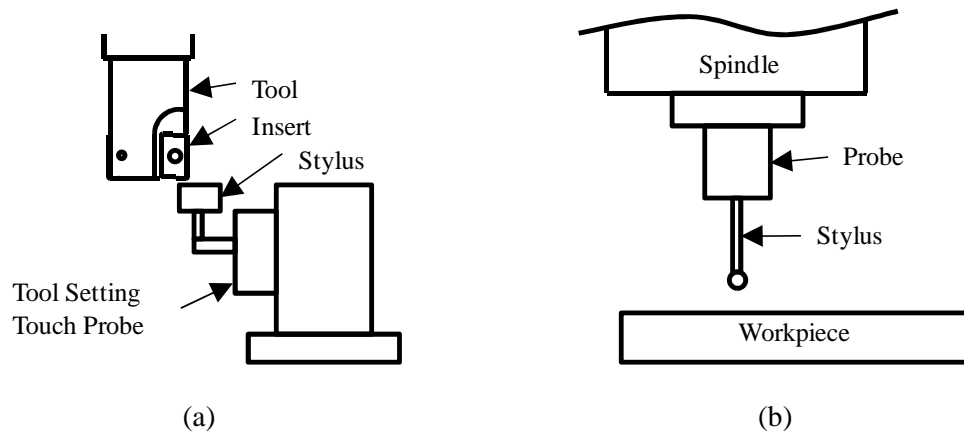


Figure 2.13: (a) Tool setting touch probe and (b) spindle touch probe.

The cutter was a 15.875 mm diameter Sandvik Coromill 390 two flute tool. The tool's part number was RA390-016M19-11L. The tool is shown in Figure 2.14 and the dimensions are shown in Table 2.5. The inserts were Sandvik Coromill 390 and the part number was R390-11 T3 08M-PM 1030. The inserts are shown in Figure 2.15 and the dimensions are shown in Table 2.6. The inserts were TiAlN PVD coated [22]. The 1030 grade is recommended by Sandvik for milling superalloys due to its resistance of material build-up on the cutting edge and plastic deformation [23].

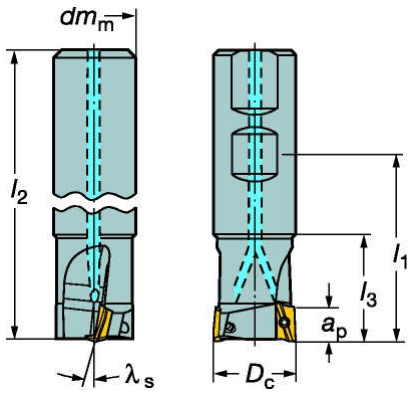


Figure 2.14: Cutting tool shape with dimensions [23].

Table 2.5: Dimesions of cutting tool [23].

Parameter	Value
D_c [mm]	15.875
dm_m [mm]	19
l_1 [mm]	56.8
l_2 [mm]	82.6
l_3 [mm]	25.9
a_p [mm]	10
λ_s [°]	13.43

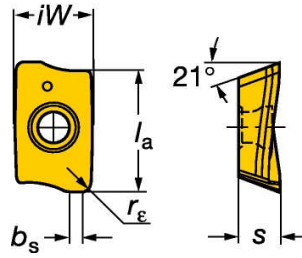


Figure 2.15: Insert shape with dimensions [23].

Table 2.6: Insert dimensions [23].

Parameter	Value
l_a [mm]	11
iW [mm]	6.8
s [mm]	3.59
b_s [mm]	1.2
r_ε [mm]	0.8

Machinability

Machinability is a term typically used to describe the ease or difficulty associated with machining a material. When machinability is quantified as a percentage, it represents a relative machinability or the ease or difficulty of machining one material in regards to another. Six phases of a nickel-superalloy machining project have been completed by a research team at Clemson University's International Center for Automotive Research (CU-ICAR) through funding and support from General Electric (GE) [18,24-28]. In that research, the machinability of several nickel-based superalloys has been studied. The relative machinabilities shown in Figure 2.16 were calculated using equation (2.16),

$$I_m = \frac{P_{ref}}{P_m} \cdot 100\% \quad (2.16)$$

where the subscript *ref* designates a reference material, *m* designates the material that is being analyzed, *I* is the machinability index, and *P* is the value of the parameter being investigated. The reference material for the data in Figure 2.16 is 304 stainless steel. This reference material was chosen because it is common in many applications and well understood. It is also more difficult to machine than carbon steels and will allow for the necessary granularity in the superalloy machinability indices [26].

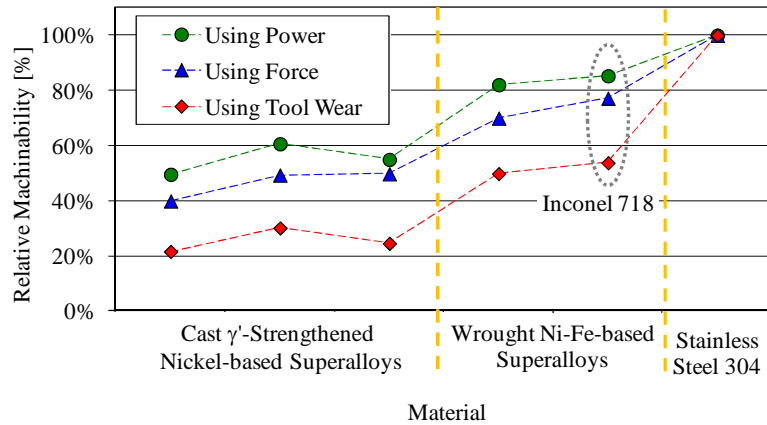


Figure 2.16: Machinability rankings for two classes of nickel-based superalloys relative to 304 stainless [2].

Three parameters were chosen for investigating and comparing materials. They were spindle power, cutting forces, and tool wear. Each of these parameters will vary in magnitude depending on the material being machined. When their magnitudes increase, the material is considered more difficult to machine and the percentage decreases. These data were collected during and after cutting tests on each material. Each cutting test was conducted with identical tooling, cutting parameters, and after a consistent specimen preparation. The test parameters are shown in Table 2.7. A 15.875 mm diameter, Sandvik, two flute tool was used with TiAlN PVD coated Coromill 390 inserts (Part number: R390-11 T3 08M-PM 1030).

Table 2.7: Cutting parameters for machinability tests.

Feed Rate [mm/rev/tooth]	0.05
Cutting Speed [m/min]	50
Depth of Cut [mm]	0.5
Radial Depth of Cut [mm]	9.5

The tool wear data, used in the machinability indices, were flank wear measurements made on the inserts by a microscope after each test. This measurement will be discussed in more detail in the Tool Wear Estimation chapter. Plots of cutting force and spindle power are shown in Figure 2.17 and Figure 2.18, respectively, for a γ' -strengthened nickel-based superalloy, Inconel 718, and 304 stainless steel.

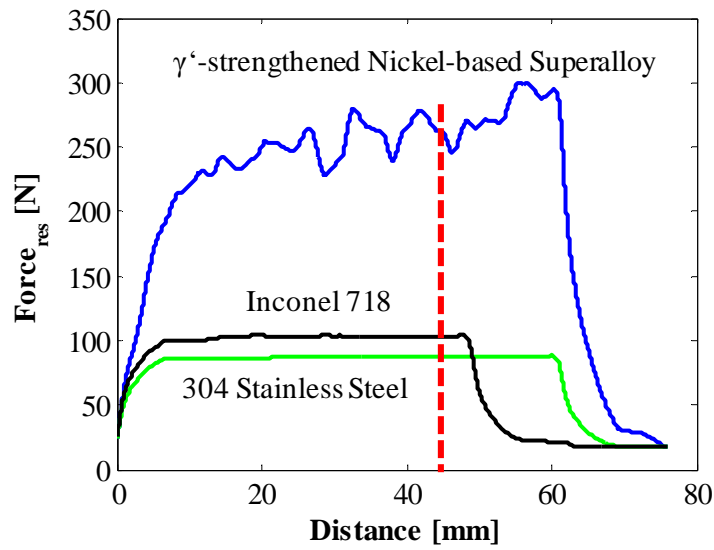


Figure 2.17: Resultant of the measured cutting forces when milling a γ' -strengthened nickel-based superalloy, Inconel 718, and 304 stainless steel under identical cutting conditions.

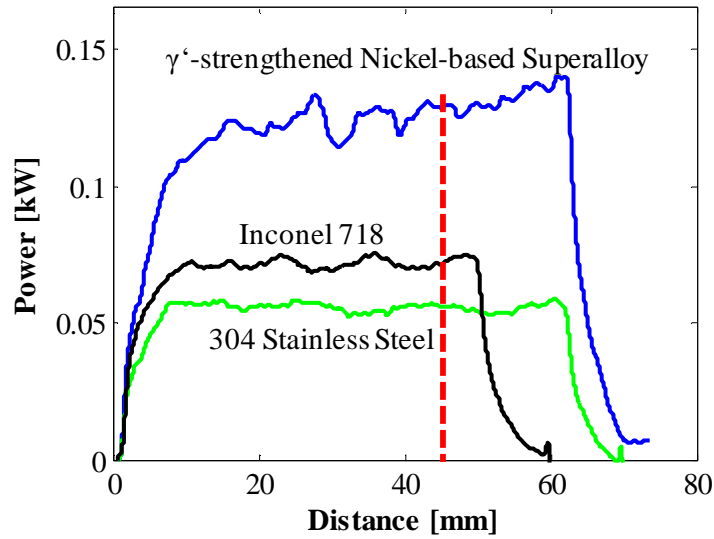


Figure 2.18: Measured spindle power when milling a γ' -strengthened nickel-based superalloy, Inconel 718, and 304 stainless steel under identical cutting conditions.

The milling forces and spindle power for the superalloy material were more than 100% higher than those for the other materials and they never stabilize on a quasi-constant value, as the others do. Rapid tool wear causes the forces and power to increase in a manner which is consistent with tool wear. This rapid increase is extreme because the forces after 50 mm of cutting are ~10% higher than at full engagement of the tool in the workpiece. The CU-ICAR team conducted a two-level, three-factor, full-factorial design of experiments (DOE) on multiple nickel-based superalloys. The factors and levels are shown in Table 2.8. The resultant cutting forces for the tests conducted with each factor at their respective high and low levels on three different cast γ' -strengthened nickel-based superalloys is shown in Figure 2.19 and Figure 2.20. These data show that even at the reduced cutting parameters, the low levels, forces increase rapidly due to tool wear and the trend is similar for multiple different γ' -strengthened nickel-based superalloy materials. Since the forces and power for the γ' -strengthened nickel-based

superalloys do not stabilize, it was necessary to determine a standard, representative, force and power value for the machinability index calculation. The maximums, during each pass, are the most appropriate because they occur while the tool is fully engaged in the material and they capture the wear effect. However, the width of the test specimens varied between 50 mm and 60 mm. Thus, the force and power data at a standard distance of 45 mm was chosen as the comparison point for all materials. The 45 mm gage distance is indicated by the dashed red line in Figure 2.17 and Figure 2.18. A substantial amount of variation is present at 45 mm in the force and power data for the superalloy. Therefore, a window of data around 45 mm was averaged and the averaged values were used in equation (2.16) to calculate the machinability indices.

Table 2.8: Factors and levels for the DOE conducted on the nickel-based superalloys.

Factors	High Level (+)	Low Level (-)
Feed Rate [mm/rev/tooth]	0.05	0.025
Cutting Speed [m/min]	50	25
Depth of Cut [mm]	0.5	0.25
Radial Depth of Cut [mm]	9.5	

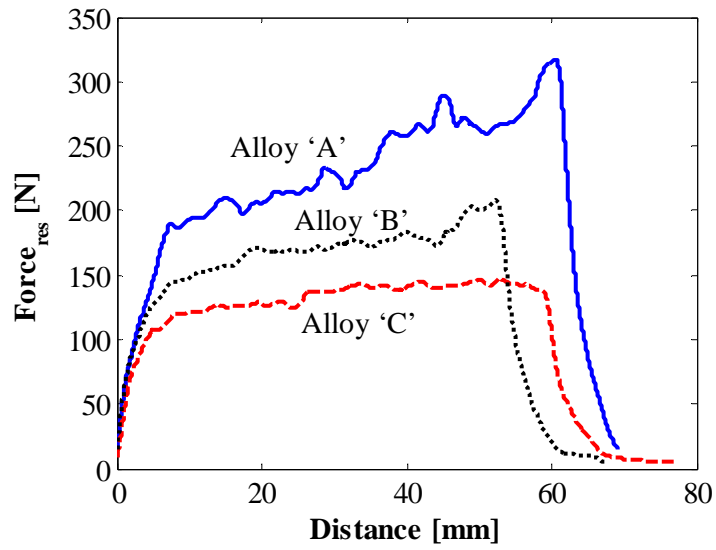


Figure 2.19: Cutting forces for the ‘high’ parameter tests conducted on three cast γ' -strengthened nickel-based superalloys.

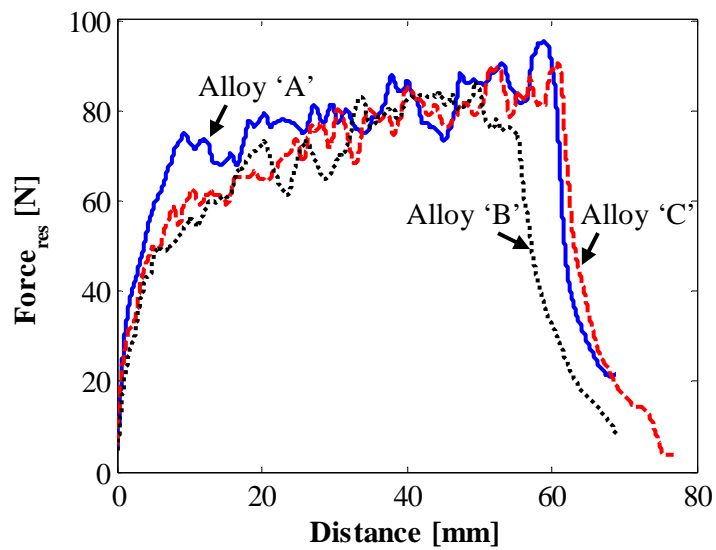


Figure 2.20: Cutting forces for the ‘low’ parameter tests conducted on three cast γ' -strengthened nickel-based superalloys.

Tool Wear

ISO-8688 is the international standard that describes methods for conducting tool wear tests [29]. It also describes many different modes of tool wear. The types of wear can be grouped into six major categories as shown in Figure 2.21. Flank wear is a consistent loss of tool material from the portion of the tool's edges (flanks) that are engaged in the cutting action. Crater wear is the formation of a depression (crater) on the rake face of the tool and located away from the cutting edge. Chipping is the breaking away of pieces of the cutting edge. Flaking is the loss of thin pieces of tool material (flakes) from any tool surface. Cracking is a fracture in the tool material (crack) that does not cause immediate breakage of the tool. Catastrophic failure is the immediate breakage of the tool. Another important type of wear is notching, or localized flank wear. It is the loss of tool material along the flanks of the cutting tool in specific locations, generally at the depth of cut and tool nose. It is shown in Figure 2.21a at the a_a depth and near the lower corner of the tool [29].

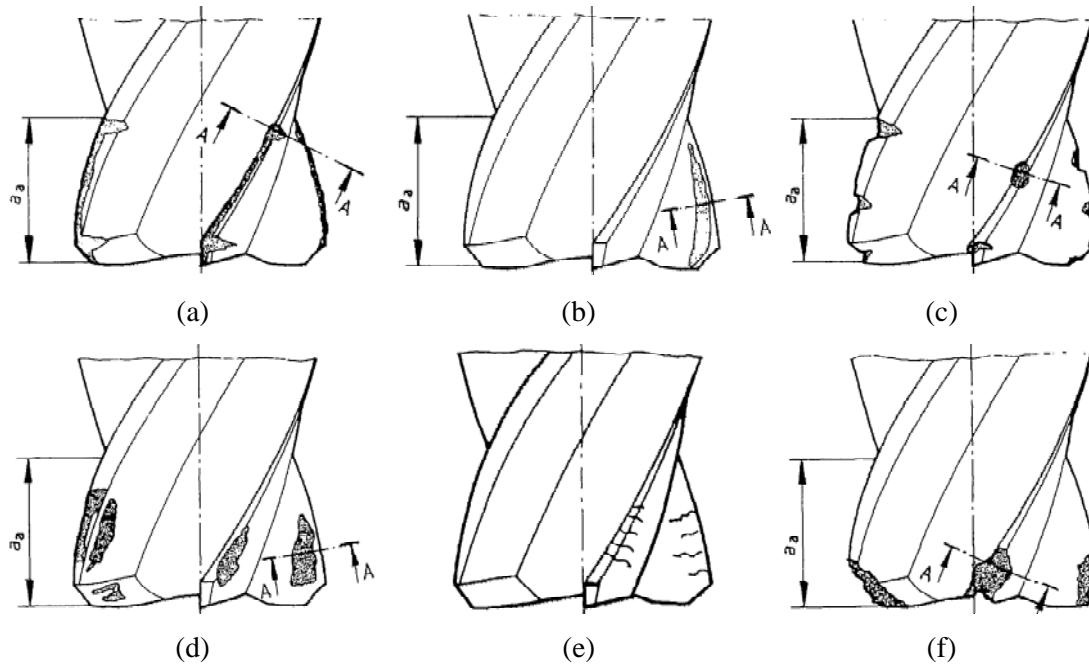


Figure 2.21: Sketches of (a) flank wear, (b) crater wear, (c) chipping, (d) flaking, (e) cracks, and (f) catastrophic failure [29].

Ezugwu, et. al. (1999) describe the primary wear types and their wear mechanisms when machining nickel-based superalloys [4]. Notching, flank wear, chipping, and catastrophic failure are the primary wear types when milling nickel-based superalloys. Explanations for notching include a variety of wear mechanisms and factors. However, a common explanation relates to work hardening of the material and the burrs that form during previous machining operations on a surface. Chipping and flaking are commonly referred to analogously because they are attributed to the same wear mechanisms, adhesion and attrition [30]. Adhesion is the bonding of the workpiece material to the tool material and it leads to attrition, which is the extraction of grains of tool material by the flow of the tool relative to the workpiece [4,30]. Catastrophic failure is related to excessive cutting forces or fatigue due to thermal and/or mechanical cycling [4].

Of the six categories of wear from the ISO standard, cracking and crater wear are not typically observed when milling nickel-based superalloys. The progression of cracking is not observed because the high forces when machining nickel-based superalloys leads any cracking in the tool to immediate catastrophic failure. Figure 2.22 shows the ISO representation for crater wear on a milling tool with the cross-section of the cutting edge. The cross-section shows that the lowest point of the crater is within the rake face of the tool and not near the edge. This is the determining factor for classifying crater wear and if the lowest point is on the cutting edge then the wear is referred to as chipping.

The diffusion wear mechanism is commonly considered to be the cause of crater wear [4,31,32]. The diffusion wear mechanism is a thermochemical process that occurs when atoms of the tool material transfer to the workpiece material [33]. Therefore, crater wear is linked with the temperature profile in the cutting zone. Cook (1973) and Devillez, et. al. (2004), found that crater wear was more prevalent at high speeds because the temperatures became higher on the rake face of the tool away from the cutting edge [31,32]. Due to the low machinability of nickel-based superalloys, high cutting speeds with carbide tooling leads to immediate tool failure. Other researchers have found that the maximum cutting temperatures for nickel alloys occur close to the cutting edge [4,34]. Other research has shown limited crater wear in nickel-based superalloys when machining with coated inserts [35].

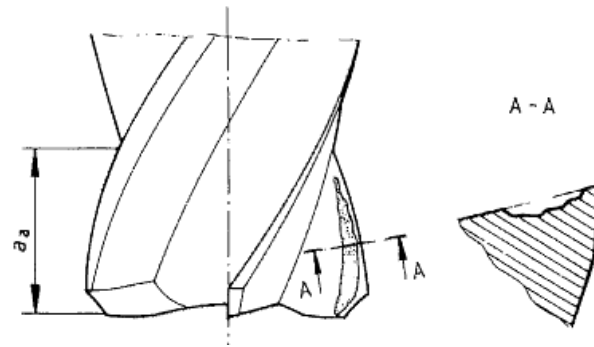


Figure 2.22: Crater wear on tool with cross-section.

Flank wear is present during essentially all cutting and in the presence of multiple other wear types. Figure 2.23 shows multiple views of a cutting edge and indicates flank wear in each view. Flank wear is considered to be the result of one or a combination of adhesion, abrasion, and/or diffusion. As previously described, the adhesion wear mechanism is the formation of bonds between the cutting tool material and the workpiece material followed by the bonds breaking and some particles of material being removed from the tool. The abrasion wear mechanism is the ploughing of the tool material by hard particles within the workpiece material (e.g., carbides). The diffusion wear mechanism is a thermochemical process that occurs when atoms of the tool material transfer to the workpiece material [33].

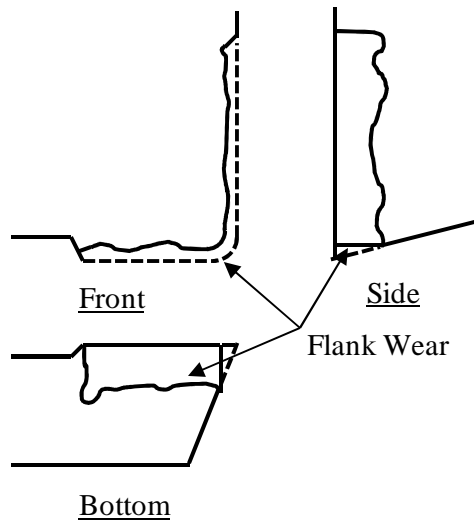


Figure 2.23: Multiple views of flank wear.

Diffusion and adhesion are both related to the temperatures in the cutting zone while abrasion is a purely mechanical mechanism. When milling nickel-based superalloys, abrasion is the result of the tool contacting and sliding against the carbides in the microstructure. Figure 2.24 shows a 2D representation of a tool cutting a workpiece. The grey area indicates the zones of the tool that are in contact with the workpiece and where abrasion wear occurs. When machining nickel-based superalloys, the uncut chip thickness is low in order to keep cutting forces low. When milling, the uncut chip thickness fluctuates as the tooth rotates through the workpiece, as shown in Figure 2.3 and Figure 2.4. Therefore, the amount of contact in the rake face zone is small, close to the cutting edge, and fluctuates. As previously stated, researchers have found that the highest temperatures when machining nickel alloys occurs near the edge of the cutting tool. Therefore, it follows that, when milling nickel-based superalloys, wear will typically occur at the cutting edge. Since abrasion in the flank zone is ever-present and the cutting temperatures are expected to be greatest at the cutting edge, flank wear is the dominant wear mechanism.

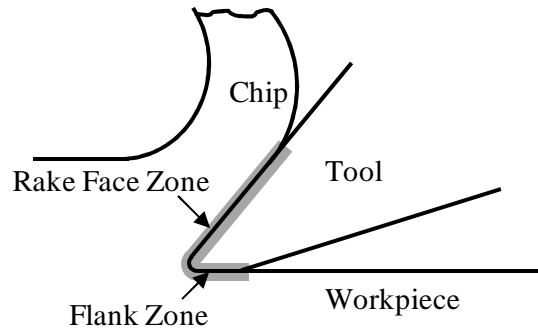


Figure 2.24: Two-dimensional representation of tool cutting the workpiece indicating contact zones.

Tool Wear Modeling

Tool wear has been studied for over 100 years. Modeling started in early 1900s with Taylor's tool life model [36]. This model is represented by equation (2.17),

$$C = VT^n, \quad (2.17)$$

where V is the cutting speed, T is the time of useful tool life, and C and n are empirical constants that depend on tool and workpiece properties, as well as cutting parameters [37]. This is a method of estimating tool life but does not give insight to the progression of wear.

Most analytical tool wear models were developed for the turning operation [33,38-40]. The turning operation is a less complex machining operation than milling. Due to the interrupted nature of milling, the cutting edges of the tools experience force and thermal cycles as they enter and exit the material every revolution. The chip size is varying and therefore the forces are varying even while a given tooth is engaged. Cutter run-out is common in multi-tooth tools and is difficult to control. Therefore, it is common for the individual cutting teeth to experience different forces due to removing different amounts of material. When researchers attempt to model tool wear for a milling process, they generally adopt models from turning research and then modify

them to represent milling behavior. Based on previous research, Teitenberg et al. (1992) assumed that the forces acting on the rake face of the tool do not change as flank wear increases and that the forces on the flank face can be represented by a normal and radial (friction) force. Based on the diagram in Figure 2.25 they determined that the change in flank forces can be represented by equations (2.18) and (2.19),

$$d\vec{F}_{nf}(\theta) = K_{nf}(\theta, \alpha) \vec{n}_f dA_f, \quad (2.18)$$

$$d\vec{F}_{ff}(\theta) = K_{ff}(\theta, \alpha) K_{nf}(\theta) \vec{r}_f dA_f, \quad (2.19)$$

where $d\vec{F}_{nf}$ and $d\vec{F}_{ff}$ are the change in the normal and friction flank force, respectively, \vec{n}_f is the unit vector in the normal direction, dA_f is the change in the area of the flank wear, and K_{ff} and K_{nf} are flank pressure and friction parameters [41]. In other research by Papazafiriou and Elbestawi, (1989) thermal cycling, due to the intermittent milling operation, is incorporated into a diffusion model derived for turning by Koren and Lenz. This model is represented by equation (2.20),

$$VB'(t) = K_d \sqrt{v_c} e^{\left(-\frac{A}{\theta_f + 273} \right)}, \quad (2.20)$$

where $VB'(t)$ is the rate of change in flank wear size with respect to time, v_c is the cutting speed, θ_f is the temperature at the interface between the tool and the workpiece, and K_d and A are constants which depend on the tool and workpiece material [38,42].

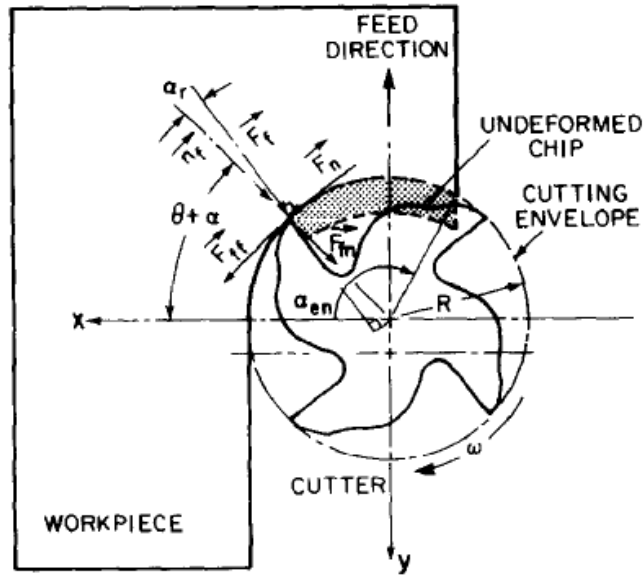


Figure 2.25: Flank face forces in Teitenberg wear model [41].

Tool wear is typically considered to occur in three stages [35,43-46]:

- rapid initial wear of cutting edge,
- gradual, linear, wear increase, and
- rapid breakdown leading to catastrophic tool failure.

These three stages are illustrated in Figure 2.26.

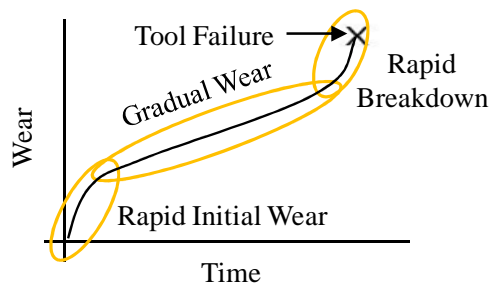


Figure 2.26: Generalization of standard tool wear curve.

The gradual wear stage has been shown to behave more predictably than the initial and final stages and researchers in the past have shown a good correlation between cutting forces and tool wear [47,48]. A common approach for estimating tool wear is to assume a linear wear progression as shown in the gradual wear stage of Figure 2.26 [43,46,47].

Tool Wear Monitoring

A substantial amount of recent tool wear research has focused on using measurement capabilities on the machining centers in order to estimate tool wear, rather than modeling it directly. Liang et al. (2004) provide a summary of techniques for monitoring many aspects of machining processes and includes a good synopsis of tool monitoring [49]. Most research indirectly measures the tool wear. Roth et al. (2010) give an overview of recent improvements in the field of tool condition monitoring. Most of the work presented in that paper deals with improving indirect measurements or mathematical approaches for inferring the tool condition [50]. Much of the past research has focused on inferring tool wear based off of measured forces or spindle torque/power during cutting [46,47,51-54]. Using acoustic emissions to determine tool wear has shown promising results and has been the focus of a number of research projects [55,56]. There have also been systems devised to measure the machined surface of the workpiece in order to determine the tool wear [57,58]. Few systems measure the tool directly. However, Pfeifer, et al. (2000) have achieved promising results through the use of vision systems to capture the tool wear directly from the tool [59]. These vision systems can be intrusive into the machine and are susceptible to damage from coolant. Prickett and Johns (1999) performed a review of the sensors to measure tool condition, various techniques to infer tool condition from signals that are available on machines without adding new hardware, and strategies for allowing the machine tool

to decide when the tool should be changed [60]. There is a system in production today, by Blum, that has the ability to directly measure the tool and detect wear greater than 5 μm . However, it utilizes a laser system to measure the tool.

No previous work was found for using touch probes to measure tool wear in milling. However, Shouszhi, et al. published research in 1995 describing the use of a contact sensor to estimate tool wear in a turning operation [61]. The intent of that work was to estimate tool wear and compensate the turning process in order to control the dimensions of the finished part. In turning there would only be a single edge to consider but in milling there are multiple edges. Also, Shouszhi, et al. were interested in the geometric changes as they affect the cutting depth and not the size of the flank wear itself [61]. Mears et al. (2009) give an overview of some recent developments in measurement capabilities which will lead to further quality and reliability in the machining process. That study also examines the implementation of on-machine coordinate measuring capabilities [62]. The Renishaw tool setting probe used for this set of experiments can be used to detect tool breakage. The Renishaw software uses a given threshold for tool tip difference. If the tool length that is measured at the tip of the cutter differs from the original measurement by more than the given threshold value, the software considers the tool to be broken. This only measures the difference at the bottom of an end mill. It is not able to measure the difference along the side. This technique works only for catastrophic failure of the tool.

Kalman Filter

R. E. Kalman published his approach to linear filtering of discrete-data through a recursive method in 1960 [63]. It has been used in many applications over the years and very frequently used in navigation. It can be applied whenever noisy measurements of a linear system state are being taken. The Kalman filter is the appropriate when state progression can be assumed

as linear and the noise in the system can be approximated as Gaussian [64,65]. The Extended Kalman Filter (EKF) was developed for nonlinear progression of states [64]. An autoregressive moving average (ARMA) has been used to estimate tool wear state based on an acoustic emission (AE) sensor [66]. ARMA requires the memory of multiple previous measurements and in its basic form is univariate.

The Kalman filter uses a predictor model to make an *a priori* estimate of a state. At a particular time step, a measurement from a noisy sensor is input into the filter. The error covariance for the sensor and prediction is used to statistically determine a weighting factor, or Kalman gain, for the measurement *innovation*. The measurement *innovation* is the difference between the model and the measurement. An *a posteriori* state update is made based on the *a priori* estimate plus the Kalman gain multiplied by the measurement *innovation*. Since it is recursive, it does not require the entire measurement history for determining the current estimate. It relies on the knowledge of the covariance in the process and in the measurement, as well as, the error covariance from the previous step to determine the optimal state estimates [65].

The Kalman filter has been applied in a number of machining operations. Altintas and Park (2004) use the Kalman filter to remove structural modes from a novel spindle mounted piezo-electric force sensor [67]. Erkorkmaz and Altintas (2000) use the Kalman filter observe disturbance torque in order to determine a machine tool's drive friction and also estimate position and velocity for the design of a high speed CNC [68,69]. Shouszhi, et al. use it to estimate dimensional errors from tool wear in a turning operation [61]. A significant benefit of the Kalman filter is the ability to utilize the measurements from multiple sensors. Möhring, et al. (2010) and Lou and Lin (1997) used the Kalman filter to integrate the output from multiple sensors for process monitoring [70,71]. The Kalman filter has been extended to non-linear

processes/measurement-process relationships. Park and Malekian (2009) use the extended version of the filter to compensate force measurements in micro end milling [72].

Typical development of the Kalman filter involves the determination of a suitable model, the measurement correlation, and process and measurement covariance matrices. These steps will be presented throughout this work and discussed in detail in the Adaptive Tool Wear Estimation chapter. The general equations of the Kalman filter are presented and described here. The issue addressed by Kalman was to determine a state estimate which minimizes the expected loss in the model shown in equation (2.21),

$$\mathbf{x}_k = \mathbf{A}_k \mathbf{x}_{k-1} + \mathbf{w}_{k-1} , \quad (2.21)$$

where k represents the current step, $k-1$ represents the previous step, \mathbf{x} is the vector of states, \mathbf{A} is the matrix which relates the previous states to the current states, and \mathbf{w} is a random variable representing Gaussian process noise. The general equation for relating the measurements to the states is shown in (2.22),

$$\mathbf{z}_k = \mathbf{H}_k \mathbf{x}_k + \mathbf{v}_k , \quad (2.22)$$

where \mathbf{z} is the vector of measurements, \mathbf{H} is the matrix that relates the states to the measurements, and \mathbf{v} is a random variable representing Gaussian measurement noise. The process and measurement noise have a zero mean and covariances of \mathbf{Q} and \mathbf{R} , respectively. Also noted as shown in equations (2.23) and (2.24),

$$p(\mathbf{w}_k) \sim N(0, \mathbf{Q}_k) \quad (2.23)$$

$$p(\mathbf{v}_k) \sim N(0, \mathbf{R}_k) . \quad (2.24)$$

The covariance matrices \mathbf{Q}_k and \mathbf{R}_k are specified as shown in equations (2.25) and (2.26),

$$\mathbf{Q}_k = E[\mathbf{w}_k \mathbf{w}_k^T] \quad (2.25)$$

$$\mathbf{R}_k = E[\mathbf{v}_k \mathbf{v}_k^T] , \quad (2.26)$$

where E denotes the statistically expected value. The estimate error, \mathbf{e}_k , is defined as shown in equation (2.27),

$$\mathbf{e}_k \equiv \mathbf{x}_k - \hat{\mathbf{x}}_k, \quad (2.27)$$

where $\hat{\mathbf{x}}_k$ is the state estimate. The state estimate is the sum of the estimate without current measurement input, *a priori* estimate, and a residual between the measurement and *a priori* estimate, *innovation*. This is represented in equation (2.28),

$$\hat{\mathbf{x}}_k = \hat{\mathbf{x}}_{k,k-1} + \mathbf{K}_k \left(\mathbf{z}_k - \mathbf{H}_k \hat{\mathbf{x}}_{k,k-1} \right), \quad (2.28)$$

where $\hat{\mathbf{x}}_{k,k-1}$ is the *a priori* state estimate, or the state estimate at k step with only $k-1$ information, and \mathbf{K} is the Kalman gain. The *a priori* state estimate is determined using equation (2.29),

$$\hat{\mathbf{x}}_{k,k-1} = \mathbf{A}_k \hat{\mathbf{x}}_{k-1}. \quad (2.29)$$

The optimal estimate is the one which minimizes the mean-square error. Thus, the Kalman gain matrix, \mathbf{K}_k , is chosen in order to minimize the mean-square error. The mean-square error, MSE_k , is represented by equation (2.30),

$$MSE_k = E \left[\mathbf{e}_k \mathbf{e}_k^T \right]. \quad (2.30)$$

The mean-square error is also the trace of the estimate error covariance matrix, \mathbf{P}_k . The estimate error covariance is specified as shown in equation (2.31),

$$\mathbf{P}_k = E \left[\mathbf{e}_k \mathbf{e}_k^T \right]. \quad (2.31)$$

The product of the error and its transpose is shown in equation (2.32),

$$\begin{aligned} \mathbf{e}_k \mathbf{e}_k^T &= (\mathbf{I} - \mathbf{K}_k \mathbf{H}_k) \mathbf{e}_{k,k-1} \mathbf{e}_{k,k-1}^T (\mathbf{I} - \mathbf{K}_k \mathbf{H}_k)^T \\ &\quad - \mathbf{K}_k \mathbf{v}_k \mathbf{e}_{k,k-1}^T (\mathbf{I} - \mathbf{K}_k \mathbf{H}_k)^T \\ &\quad - (\mathbf{I} - \mathbf{K}_k \mathbf{H}_k) \mathbf{e}_{k,k-1} \mathbf{v}_k^T \mathbf{K}_k^T \\ &\quad + \mathbf{K}_k \mathbf{v}_k \mathbf{v}_k^T \mathbf{K}_k^T. \end{aligned} \quad (2.32)$$

The estimate error covariance is shown in equation (2.33),

$$\begin{aligned}
\mathbf{P}_k &= (\mathbf{I} - \mathbf{K}_k \mathbf{H}_k) E[\mathbf{e}_{k,k-1} \mathbf{e}_{k,k-1}^T] (\mathbf{I} - \mathbf{K}_k \mathbf{H}_k)^T \\
&\quad - \mathbf{K}_k E[\mathbf{v}_k \mathbf{e}_{k,k-1}^T] (\mathbf{I} - \mathbf{K}_k \mathbf{H}_k)^T \\
&\quad - (\mathbf{I} - \mathbf{K}_k \mathbf{H}_k) E[\mathbf{e}_{k,k-1} \mathbf{v}_k^T] \mathbf{K}_k^T \\
&\quad + \mathbf{K}_k E[\mathbf{v}_k \mathbf{v}_k^T] \mathbf{K}_k^T .
\end{aligned} \tag{2.33}$$

The *a priori* error is independent of the measurement noise in the current estimate and therefore the expected value of their product becomes just the product of their expected values. This is shown in equation (2.34),

$$E[\mathbf{v}_k \mathbf{e}_{k,k-1}^T] = E[\mathbf{v}_k] E[\mathbf{e}_{k,k-1}] = 0 . \tag{2.34}$$

The expected measurement noise is 0, by definition, and therefore, the expected value of the measurement noise multiplied by the *a priori* error is zero. The estimate error covariance is determined by substituting the *a priori* estimate error covariance, equation (2.26), and equation (2.34) into equation (2.33), as shown in equation (2.35),

$$\begin{aligned}
\mathbf{P}_k &= (\mathbf{I} - \mathbf{K}_k \mathbf{H}_k) \mathbf{P}_{k,k-1} (\mathbf{I} - \mathbf{K}_k \mathbf{H}_k)^T + \mathbf{K}_k \mathbf{R}_k \mathbf{K}_k^T \\
&= \mathbf{P}_{k,k-1} - \mathbf{K}_k \mathbf{H}_k \mathbf{P}_{k,k-1} - \mathbf{P}_{k,k-1} \mathbf{H}_k^T \mathbf{K}_k^T + \mathbf{K}_k (\mathbf{H}_k \mathbf{P}_{k,k-1} \mathbf{H}_k^T + \mathbf{R}_k) \mathbf{K}_k^T .
\end{aligned} \tag{2.35}$$

Similarly, the *a priori* estimate error covariance is determined as shown in equations (2.36), (2.37), and (2.38):

$$\mathbf{P}_{k,k-1} = E[\mathbf{e}_{k,k-1} \mathbf{e}_{k,k-1}^T], \tag{2.36}$$

$$\mathbf{e}_{k,k-1} \mathbf{e}_{k,k-1}^T = \mathbf{A}_k \mathbf{e}_{k-1} \mathbf{e}_{k-1}^T \mathbf{A}_k^T - \mathbf{w}_k \mathbf{e}_{k-1}^T \mathbf{A}_k^T - \mathbf{A}_k \mathbf{e}_{k,k-1} \mathbf{w}_k^T + \mathbf{w}_k \mathbf{w}_k^T, \tag{2.37}$$

$$\mathbf{P}_{k,k-1} = \mathbf{A}_k \mathbf{P}_{k-1} \mathbf{A}_k^T + \mathbf{Q}_k . \tag{2.38}$$

The goal is to determine a gain, \mathbf{K}_k , which minimizes the mean-square error and as mentioned before, the mean-square error is the trace of the \mathbf{P}_k matrix, $\text{tr}(\mathbf{P}_k)$. Thus, the \mathbf{K}_k which minimizes the mean square error is determined by taking the derivative, with respect to \mathbf{K}_k , of the trace of \mathbf{P}_k and setting it equal to zero. The derivative of $\text{tr}(\mathbf{P}_k)$ with respect to \mathbf{K}_k is shown in equation (2.39),

$$\frac{\partial \text{tr}(\mathbf{P}_k)}{\partial \mathbf{K}_k} = -2\mathbf{P}_{k,k-1}\mathbf{H}_k^T + 2\mathbf{K}_k(\mathbf{H}_k\mathbf{P}_{k,k-1}\mathbf{H}_k^T + \mathbf{R}_k). \quad (2.39)$$

Setting equation (2.39) equal to zero and solving for \mathbf{K}_k results in equation (2.40),

$$\mathbf{K}_k = \mathbf{P}_{k,k-1}\mathbf{H}_k^T(\mathbf{H}_k\mathbf{P}_{k,k-1}\mathbf{H}_k^T + \mathbf{R}_k)^{-1}. \quad (2.40)$$

By substituting equation (2.40) into equation (2.35), the equation for the estimate error covariance is simplified, as shown in equation (2.41),

$$\mathbf{P}_k = (\mathbf{I} - \mathbf{K}_k\mathbf{H}_k)\mathbf{P}_{k,k-1}. \quad (2.41)$$

Equation (2.41) is the last of the necessary equations for implementation of the Kalman filter [63,64,73].

Once the equations have been setup they need to be implemented according to the methodology of the Kalman filter. The order of steps are listed below.

- 0) Estimate the process, measurement, and initial error covariance matrices based on experimental data or inference.
- 1) Determine the *a priori* state estimate by projecting the previous *a posteriori* estimate forward, using equation (2.29).
- 2) Determine the *a priori* estimate error covariance by projecting the previous *a posteriori* estimate error covariance forward, using equation (2.38).
- 3) Determine the Kalman gain using equation (2.40).
- 4) Determine the *a posteriori* state estimate by adding the product of the Kalman gain and *innovation* to the *a priori* state estimate using equation (2.28).
- 5) Determine the *a posteriori* error covariance using equation (2.41).
- 6) Repeat, beginning with 1, for the next step, k .

Force Modeling

Cutting force modeling is common within machining research due to its linkage with part quality, tool life, and cutting power. A wide variety of cutting force models can be found within literature. They range from the purely empirical models to highly complex analytical models.

Empirical

Empirical models are typically simple equations which are based off of data gathered from experiments. These are generally accurate for the given machining conditions, workpiece, and tool geometry.

Empirical methods were used by Choudhury and Rath (2000) and Sarhan et al. (2001) for finding the relationship between the cutting parameters and the cutting forces generated, used later for monitoring the tool wear [46,54]. An experimental method was also used by Alauddin et al. (1996) for determining the cutting forces in machining of superalloys, which are generally higher because of the high shear stresses in the material. The authors developed a mathematical model for the average cutting force in slot milling of Inconel 718. The equation derived for average cutting force, determined by using response surface methodology, is given as follows:

$$\hat{F}_{ta} = 2370 f_z^{0.87} a_a^{1.12}, \quad (2.42)$$

where \hat{F}_{ta} is the predictive average tangential cutting force, f_z is the feed per tooth (mm/tooth), and a_a is the axial depth of cut (mm). This model was statistically shown to be valid for end milling Inconel 718, with carbide inserts, under dry conditions, at a cutting speed of 20 m/min, and for a feed of 0.06 – 0.088 mm/tooth and an axial depth cut of 0.5 – 2.0 mm [74]. For this model it is assumed that the effects of cutting speeds are negligible when calculating the average cutting forces. However, Arunachalam et al. (2000) shows that average cutting forces decreases with increased cutting speeds, which is in accordance with the observations from high speed

machining (HSM) [75]. Real-time parameter estimation on such models has been successfully implemented in grinding of hardened steels [76-79]. Modified versions of these techniques are applicable to superalloy milling.

Semi-empirical (Mechanistic)

The semi-empirical models are based on physical principles with experimentally determined factors. This type of model is very common in machining research. It was developed from the theory that a given material will have an associated specific cutting force (K) [9,80]. This specific cutting force is the cutting force per unit of chip area. Therefore, the cutting force can be calculated using equation (2.43).

$$F = Kbh, \quad (2.43)$$

where F is the cutting force, b is the axial depth of cut, and h is the chip thickness. These parameters are shown in Figure 2.3, which also shows the radial depth of cut (DOC_r). The chip thickness varies with time and can be approximated using equation (2.44).

$$h = f_t \sin(\theta), \quad (2.44)$$

where f_t is the feed per tooth and θ is the angle of rotation of cutting edge. This approach is semi-empirical because, as stated, the K is an experimentally determined factor. It is still dependent on the nature of the cut, the geometry of the tool, the material of the workpiece. This model is discussed further in the Force Model Development chapter.

Analytical

An early attempt to develop an analytical cutting force model was published by Merchant in 1944. He developed the orthogonal cutting model which is applicable in two dimensional cutting operations and he expanded it into three dimensions via the oblique cutting force model.

A sketch of the orthogonal cutting force model is shown in Figure 2.27. This model relates cutting forces to the rake angle of the tool, friction effects of the chip moving along the rake face of the tool, and the angle of the shear plane in relation to the cut surface [81]. The shear angle is the focus of significant research since Merchant published his model [82-84]. Due to the complexity and interrelationships of cutting forces and temperatures and variability in tooling design and cutting paths, a completely analytical force model for milling is not practical for a production environment.

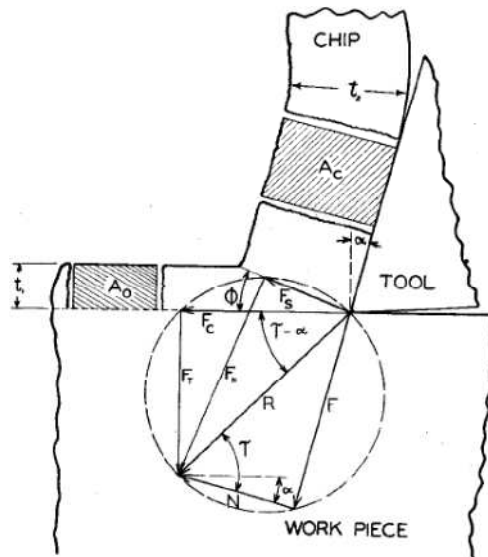


Figure 2.27: Orthogonal cutting model proposed by Merchant [85].

Finite Element

A significant step in attempting to develop a finite element model of a cutting process is to adopt a constitutive model for the workpiece material. For a large range of materials, the constitutive law is based on the Johnson-Cook (J-C) model [86]. The J-C model accounts for the material strain hardening, strain rate hardening, and thermal softening during the cutting process:

$$\sigma = \left(A + B\varepsilon^n \right) \left(1 + C \ln \frac{\dot{\varepsilon}}{\dot{\varepsilon}_0} \right) \left(1 - \left(\frac{T - T_r}{T_m - T_r} \right)^m \right), \quad (2.45)$$

where: σ is the equivalent flow stress, ε is the equivalent plastic strain, $\dot{\varepsilon}$ is the equivalent plastic strain rate, $\dot{\varepsilon}_0$ is the reference equivalent plastic strain rate, T is the workpiece temperature, T_m is material melting temperature and T_r is room temperature. Such models have been employed on a variety of high temperature materials [87]. For nickel-based alloys, that are designed to have an almost uniform flow stress until certain high temperatures, a new model is formulated. A ‘piece-wise’ J-C model was proposed by Ranganath et al. to represent the plasticity behavior of a commercial IN100 nickel-based superalloy, by combining multiple separate J-C equations [11]. Figure 2.28b shows that the piecewise model captures the strength of the nickel-based superalloy at higher temperatures. In other work on cast γ' -strengthened nickel-based superalloys, Chen et al. present results from orthogonal cutting tests and show that current constitutive models do not accurately reflect the properties of the material and therefore an improved model for these materials needs to be generated before accurate finite element analysis results can be obtained [88].

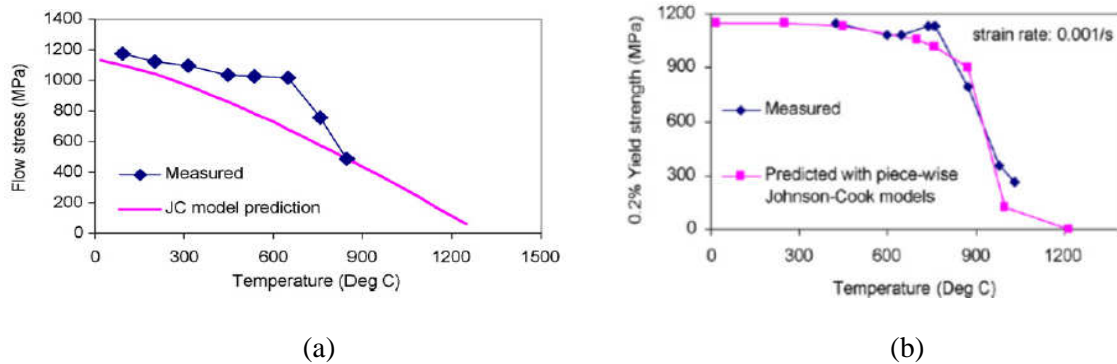


Figure 2.28: (a) J-C prediction and measured flow stress for Inconel 718, (b) Predicted using the new model and measured yield stress for IN100 [11].

Analytical and numerical models are very detailed but not practical for process control because of the computational intensity and lack of processing power at the machining center. Shi et al. (2010) used finite element modeling to develop and validate the constitutive data for material models of copper, steel, and Inconel. The constitutive model was later used to predict the cutting forces which were validated through experiment [89]. Typically the constitutive model for the material is determined and then used to determine the forces required to shear and deform the material [89].

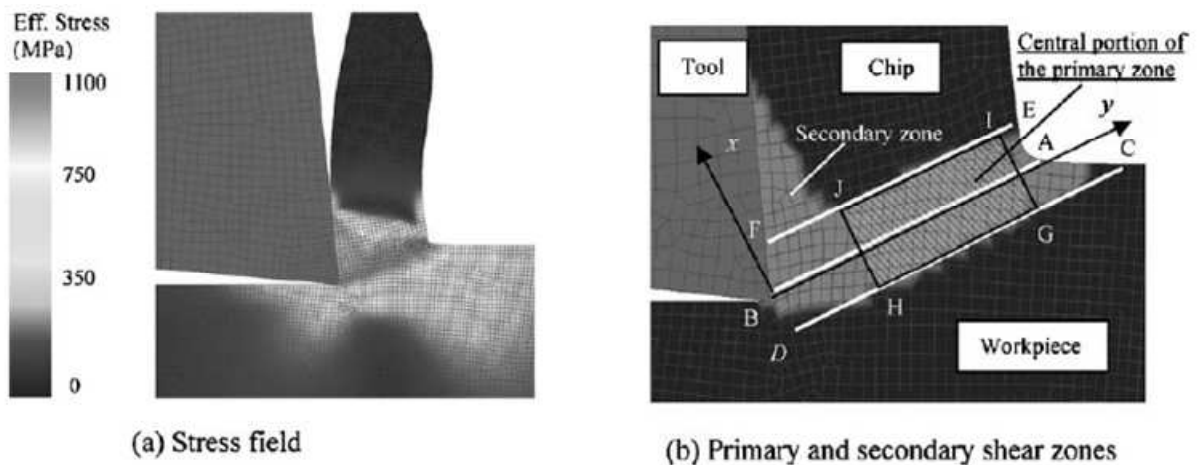


Figure 2.29: Typical results of a finite element simulation [89].

Concluding Remarks

A significant research gap exists in the work related to milling γ' -strengthened nickel-based superalloys. The machinability reviews by Ezugwu, et al. (1998 and 2003) provide some discussions on the machining difficulties and heuristics for developing the machining operation. However, it does not address the development of process models or specific techniques for the progression or advancement of the milling of these materials. Process models will provide

enhanced predictions for setup and planning, estimations for control, and improved fundamental understanding.

Tool wear is stochastic process with many complex interactions, especially within milling. An adaptive measurement approach that captures the effects of the tool wear while providing some understanding of the process is a robust method for determining in-process tool wear. The Kalman filter has been used effectively for estimating states from noisy data in multiple machining applications and there is a lot of work to build upon. The Kalman filter also provides a platform for building a network of sensors for providing feedback. Analytical cutting models are complex by nature and when they are adapted to milling or more specifically the milling of very difficult to machine alloys (i.e., nickel-based superalloys) they become excessively complex. The semi-empirical cutting force model provides an equilibrium between the fundamental physics involved in the cutting process and computational tractability. Given the computational power of the controllers on modern machine tools, this model may be employed in real-time for process control. Therefore, the semi-empirical cutting force model is the platform chosen as the basis for the estimation approach formulated in this research.

CHAPTER THREE

TOOL WEAR ESTIMATION

As discussed in the Background chapter, cast γ' -strengthened nickel-based superalloys are extremely difficult to machine and, therefore, induce rapid wear on cutting tools under all machining conditions. This rapid tool wear is evident in the cutting forces, as shown in Figure 2.19 and Figure 2.20. The objective of this research is to develop a real-time, adaptive, cutting force model for milling nickel-based superalloys. In order to do this, tool wear must be accounted for. In this chapter, modeling and measurement considerations for tool wear while milling nickel-based superalloys will be discussed.

Determination of Wear Model

As discussed in the Background chapter, tool wear is typically considered to occur in three stages, as shown in Figure 2.26. When milling cast γ' -strengthened nickel-based superalloys, the initial and final stages of wear occur so rapidly that the progression in these stages becomes undetectable under most conditions. Therefore, the primary focus in this research is the middle, linear, stage. Since the wear in this stage progresses linearly, it is appropriate to model it using a linear relationship. A generalized representation of a linear model on a typical wear curve is shown in Figure 3.1. The equation of the time based form of the model is shown in (3.1),

$$VB(t) = VB_0 + VB' \cdot t \quad (3.1)$$

where VB is the size of the flank wear, VB_0 is the “initial” size of the flank wear, VB' is the rate of change of tool wear with respect to time, and t is machining time. VB_0 is not a true initial size of the flank wear because the true initial flank wear size is zero with a new insert. This value is the

amount of flank wear that would be present if the linear portion of the wear curve were extrapolated to $t = 0$, as shown in Figure 3.1.

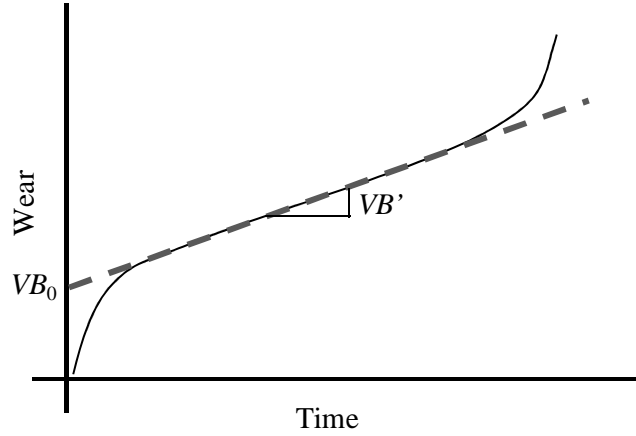


Figure 3.1: Generalized wear model on a typical wear curve.

Machining time, distance traveled by the cutter, and volume of material removed are directly proportional to one another for a given set of operating parameters, equation (3.1) can be rewritten in terms of either of these parameters. These alternative relationships are shown in equation (3.2),

$$VB(x) = VB_0 + VB' \cdot x : \quad \left\{ VB' = \frac{dVB}{dx} \right\} \quad (3.2)$$

with respect to distance, x , and in equation (3.3),

$$VB(V_{mr}) = VB_0 + VB' \cdot V_{MR} : \quad \left\{ VB' = \frac{dVB}{dV_{MR}} \right\} \quad (3.3)$$

with respect to the cumulative volume of material removed, V_{MR} . The goal of a machining process is to remove volumes of material. The volume of material removed is the metric which is not

ambiguous in terms of the process goal and is the best metric to use for analyzing and comparing tool life. Therefore, equation (3.3) is the tool wear model in this research.

Experiment Design

Milling experiments were conducted and data was collected in order to determine model parameters and validate the research approach. The machining tests were conducted using a single set of parameters and the test was conducted three times in succession to get a sense of the repeatability. The layout of the passes is shown on a diagram of the workpiece in Figure 3.2. The top view of the workpiece shows that the tool started in front of the workpiece and fed across in the y-direction. The front view shows that the passes were made in succession from left to right and that between each test the workpiece was faced in order to create a new consistent top surface. Passes labeled with the number one were the first passes with a new cutting edge. A flow chart showing the progression of steps for the entire experiment is shown in Figure 3.3.

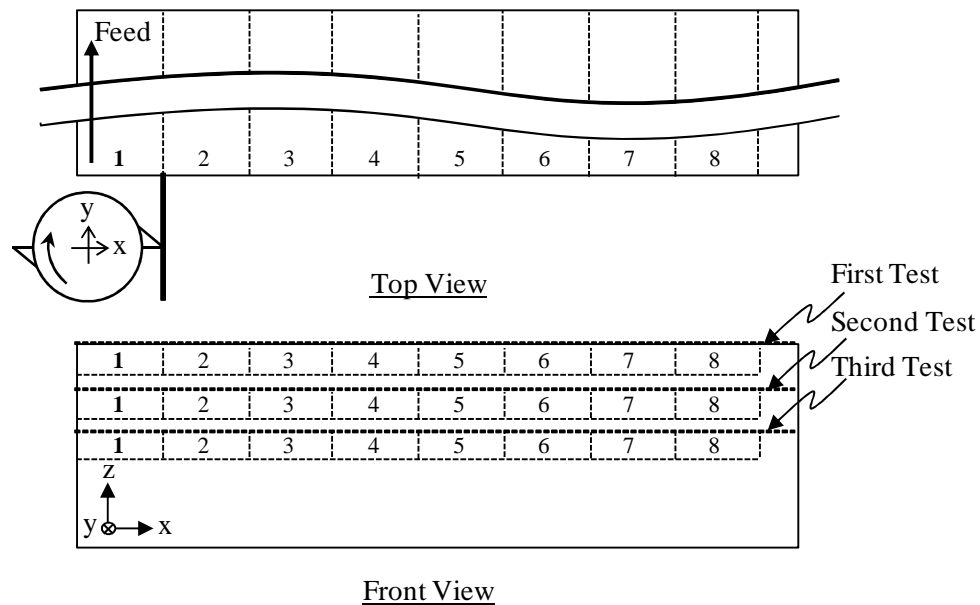


Figure 3.2: Schematic of the test cuts.

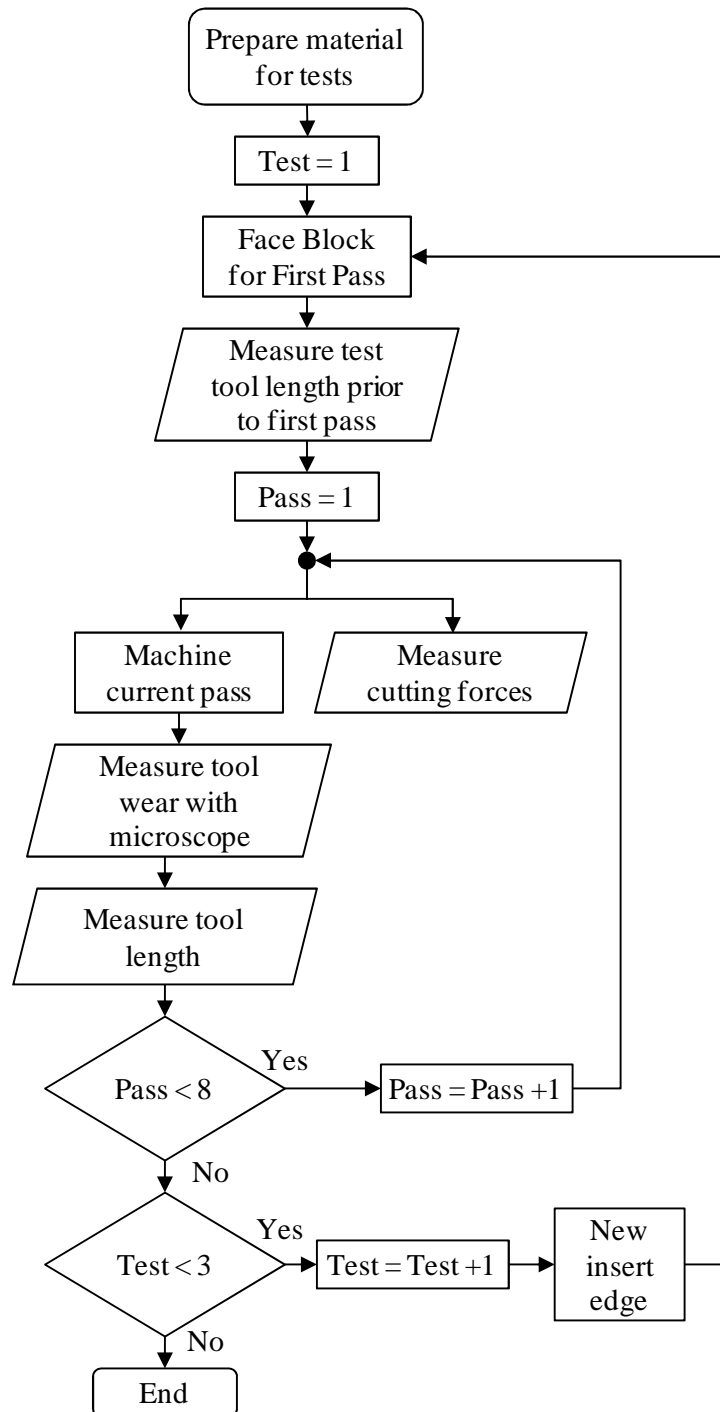


Figure 3.3: Flow chart of the cutting experiment.

The cutting parameters are shown in Table 3.1. The results of the DOE tests described in the Machinability section of the Background chapter provided a range of tool life and cutting force data. The cutting parameters for this tool wear experiment were chosen, from the DOE tests, because they result in good tool wear resolution within the useful operating range of the tool. These parameters allow multiple cutting passes prior to tool failure and substantial wear within the constraints of the machining setup. The in-process wear measurements were made via touch probes and a digital microscope between each pass. The microscope measurements were used to determine the accuracy of the probe measurements for each wear test and determine the wear model to be used in the Kalman filter. The force data were collected to determine the accuracy of updated force model.

Table 3.1: Cutting parameters for tool wear test.

Feed Rate [mm/rev/tooth]	0.05
Cutting Speed [m/min]	50
Depth of Cut [mm]	0.25
Radial Depth of Cut [mm]	9.5
Pass Length [mm]	61

Estimation from Probe Measurements

The tool and insert geometry is shown in Figure 3.4. The change in tool length, ΔL , was measured directly by the tool setting probe or indirectly by the spindle touch probe. VB is the measured flank wear from analysis of the inserts under a microscope. The actual worn insert illustrating ΔL and VB is shown in Figure 3.5. A mathematical relationship for VB in terms of ΔL was determined by applying trigonometric relationships to the geometry shown in Figure 3.4. This relationship is shown in equation (3.4),

$$VB = \Delta L \left(\frac{1}{\tan(\psi)} - \tan(\lambda_s) \right). \quad (3.4)$$

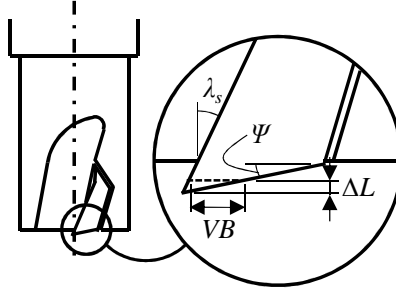


Figure 3.4: The insert and tool geometry at the bottom of the cutting edge.

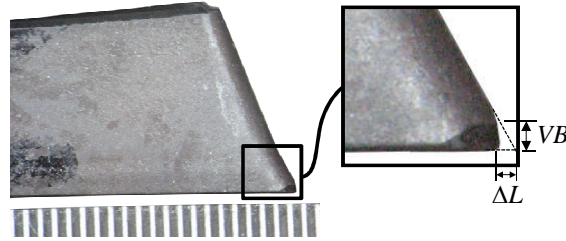


Figure 3.5: A worn insert depicting flank wear and the probe measurement.

For the particular tool and inserts used in these experiments, λ_s and Ψ were found by using specifications from the manufacturer and measuring the actual inserts under the microscope. The angles, λ_s and Ψ , were found to be 18.5° and 6.5° , respectively. Therefore, the measured flank wear is expected to be 8.5 times larger than the measured change in tool length.

When measuring the flank wear with a microscope, important considerations must be made. The relative angle between the eyepiece/camera and the insert edge can introduce significant error. This is shown in Figure 3.6. The dashed lines represent the progression of wear

and the edge radius. VB_A and VB_B represent the flank wear measurements based on viewing angle A or B, respectively. There is an additional error associated with the 'B' measurement due to the inability of a microscope to focus on the entire edge within the field of view. Therefore, some estimation by the user is necessary to determine the edge location. Measurement 'A' is considered to be more accurate because this is from the perpendicular view of the flank wear and thus the realistic measurement of the flank wear size. There are other nuances in regards to location of measurements associated with the complex geometries of cutting edges. Therefore, setting a default standard for all cutter geometries is not practical. For purposes of correlating other measurements to microscope measurements, consistency in microscope measurements is key. Measurements were taken along the entire length of the bottom edge of the insert and were averaged for each tooth. Figure 3.7 shows the wear on the bottom edge of an actual insert. The yellow bars represent the average wear measurement.

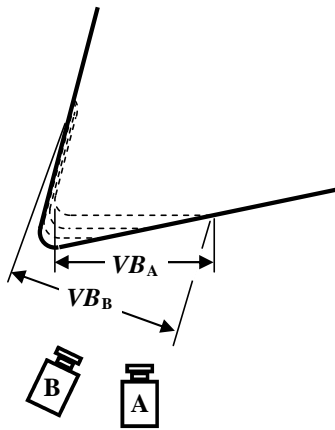


Figure 3.6: Sketch of cross-section of bottom of insert with wear progression and viewing angles.

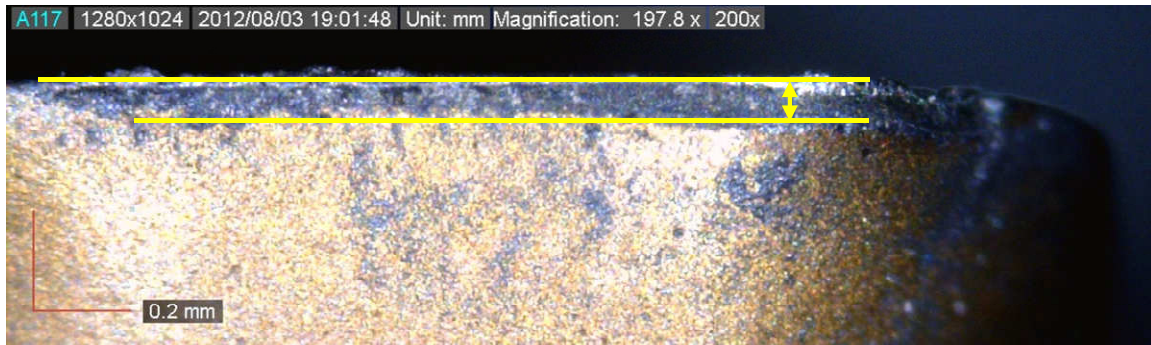


Figure 3.7: Picture of tool's end wear showing measurement location.

Due to the shallow depth of cut used in this set of experiments, this method was only applied to the bottom edge of the inserts. However, a similar methodology can be used to apply this to the side edge of an insert. The tool set station has the ability to measure tool radius and the spindle probe can be used to measure side walls of a part. Care must be taken when measuring the radius of the insert to be sure that only the wear area is in contact with the stylus of the probe.

Data Analysis

The touch probe was used to measure the length of the tool. Three tool length measurements were made between each pass and the measurements were written to a text file on the machine's controller. A truncated set of raw data from the touch probe are shown in Table 3.2. The point IDs designate the pass that the measurement was taken after and the letter indicates the different measurement. The data were processed and condensed by calculating the mean of all three measurements per pass and then calculating the difference between each passes average and the initial average. For example, the change in tool length for pass 1 was calculated by subtracting the mean of the 1a-1c data and subtracting that from the mean of the 0a-0c data. These results are shown in Table 3.3.

Table 3.2: Truncated raw touch probe data from tool wear tests.

Point ID	Test 1	Test 2	Test 3
	L [mm]	L [mm]	L [mm]
0a	120.335	120.344	120.334
0b	120.336	120.341	120.336
0c	120.336	120.342	120.333
1a	120.332	120.338	120.33
1b	120.331	120.338	120.33
1c	120.331	120.336	120.33
2a	120.328	120.334	120.328
\vdots	\vdots	\vdots	\vdots
8c	120.325	120.328	120.324

Table 3.3: Processed tool setting touch probe data.

Pass	Test 1		Test 2		Test 3	
	Mean L [mm]	ΔTS [mm]	Mean L [mm]	ΔTS [mm]	Mean L [mm]	ΔTS [mm]
0	120.336	0.000	120.342	0.000	120.334	0.000
1	120.331	0.005	120.337	0.005	120.330	0.004
2	120.330	0.006	120.333	0.009	120.328	0.006
3	120.328	0.008	120.332	0.010	120.329	0.005
4	120.328	0.008	120.332	0.010	120.327	0.007
5	120.329	0.007	120.331	0.011	120.327	0.007
6	120.329	0.007	120.330	0.012	120.326	0.008
7	120.326	0.010	120.329	0.013	120.325	0.009
8	120.326	0.010	120.329	0.013	120.325	0.009

Figure 3.8 shows the average and standard deviation of the flank wear measurements made with the microscope on both inserts after each pass during the three tool wear experiments. The dashed line represents the best linear fit for the wear measurements. The R^2 value for the linear fit is 0.977 which indicates a good fit and it can be seen from the data that the linear

assumption is valid. Since all of the data are linear, it shows that by the end of the first pass, the tool has already been worn beyond the initial wear stage. It also shows that the inserts are not utilized until fracture, thus there is no rapid breakdown at the end.

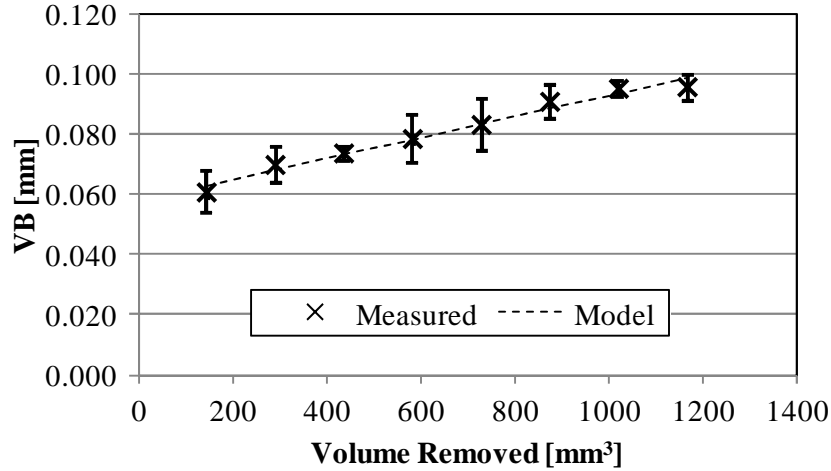


Figure 3.8: Flank wear versus the volume of material removed.

From a least squares fit of the average flank wear measurements made with the microscope, the values of VB_0 and VB' were determined to be 0.058 mm and $3.48 \times 10^{-5} \text{ mm}_{\text{wear}}/\text{mm}^3$, respectively. For comparison, a representative wear rate for turning AISI 4340 steel with a carbide insert is $\sim 4 \times 10^{-8} \text{ mm}_{\text{wear}}/\text{mm}^3$ [90]. This is nearly a 1000X difference. This is not a direct comparison because turning is a steady cut with a single cutting edge removing all of the material, whereas milling is an interrupted cut with multiple inserts removing material. Due to no interruptions in the cut and therefore no shock on the cutting edge a turning tool will typically wear slower than a single milling insert but when multiple inserts are involved the overall wear rate on a milling tool may be slower. To illustrate the difference between these wear rates, Figure 3.9 shows a plot of VB as a function of volume of material removed for a cast

γ' -strengthened nickel-based superalloy and AISI 4340 Steel. The plotted lines represent model estimations for both materials. The plot shows that within 4 cm³ of material removed the carbide tool would incur ~200 μ m of flank wear when machining the cast γ' -strengthened nickel-based superalloy, whereas the tool wear would remain constant when machining the AISI 4340 Steel. A carbide tool could remove nearly 3600 cm³ of steel before incurring 200 μ m of flank wear. That is approximately 28 kg (62 lbs.) more steel than superalloy.

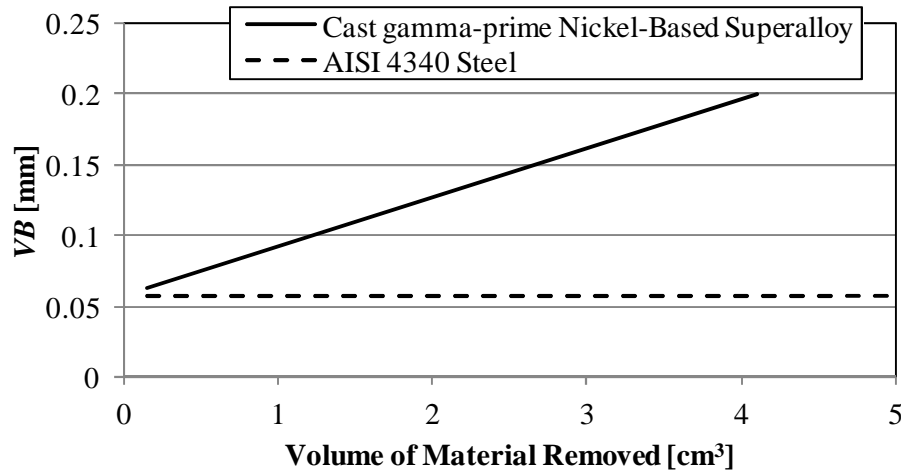


Figure 3.9: Wear rate comparison between a γ' -strengthened nickel-based superalloy and AISI 4340 Steel.

The measured change in tool length for each of the three tests is shown in Figure 3.10. This plot is also similar to the typical wear curve. The data show a difference in the measurements between Test 2 and the other two tests. The data indicate that initially more wear develops on the inserts in the second test than in the first or third but eventually the wear rate in the second test stabilized and progresses at a similar rate as in the first or third test. The difference was due to run-out that was induced during the installation of new inserts. As mentioned in the

Milling Process section of the Background chapter, run-out in milling causes one tooth to remove more material than the other(s). The run-out caused one of the inserts to wear at a more rapid rate until the tools equalized and began wearing at a similar rate as the other tests.

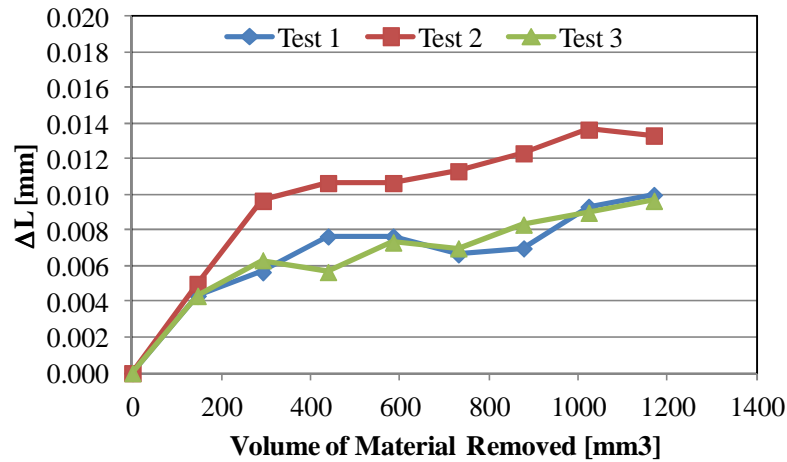


Figure 3.10: Change in measured tool length from pass-to-pass during tool wear tests.

By considering the possible combinations of radial run-out and axial run-out, four general scenarios of cutter run-out are determined and shown in Figure 3.11. The first scenario represents the case when run-out is present in the radial direction but not the axial direction. The second scenario represents the case when run-out is present in the axial direction but not the radial direction. The third scenario represents the case when run-out is present in both the axial and radial directions and a single insert. The fourth scenario represents the case when radial run-out is present on one insert and axial run-out is present on the other.

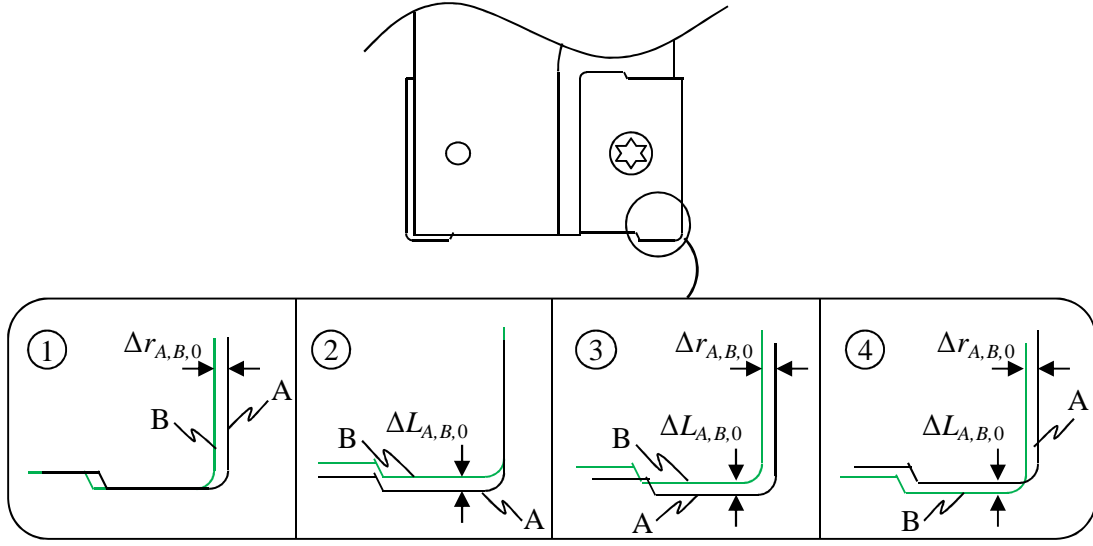


Figure 3.11: Four general scenarios of cutter run-out.

By assuming that a single insert in milling wears at a rate of VB'_{single} , then the flank wear, with as a function of time, for insert A, $VB_A(t)$, is shown in equation (3.5),

$$VB_A(t) = VB'_{\text{single}} V_{MR,A}(t) + VB_{0,\text{single}}, \quad (3.5)$$

and for insert B, $VB_B(t)$, is shown in equation (3.6),

$$VB_B(t) = VB'_{\text{single}} V_{MR,B}(t) + VB_{0,\text{single}}, \quad (3.6)$$

where $VB_{0,\text{single}}$ is the initial wear for a single insert and $V_{MR,A}(t)$ and $V_{MR,B}(t)$ are the cumulative volumes of material removed as functions of time for the respective inserts. If deflection of the tool is assumed to be negligible, then the cumulative volume of material removed for insert A is shown in equation (3.7),

$$V_{MR,A}(t) = \int_0^t b_A(t) A_{c,A}(t) dt, \quad (3.7)$$

and for insert B in equation (3.8),

$$V_{MR,B}(t) = \int_0^t b_B(t) A_{c,B}(t) dt. \quad (3.8)$$

where $b_A(t)$ and $b_B(t)$ are the depth of cut for inserts A and B, respectively, when time is t and $A_{c,A}(t)$ and $A_{c,B}(t)$ are the area of the uncut chip for inserts A and B, respectively, when time is t . The change in the cut dimensions with respect to time is shown in regards to a machined pass in Figure 3.12.

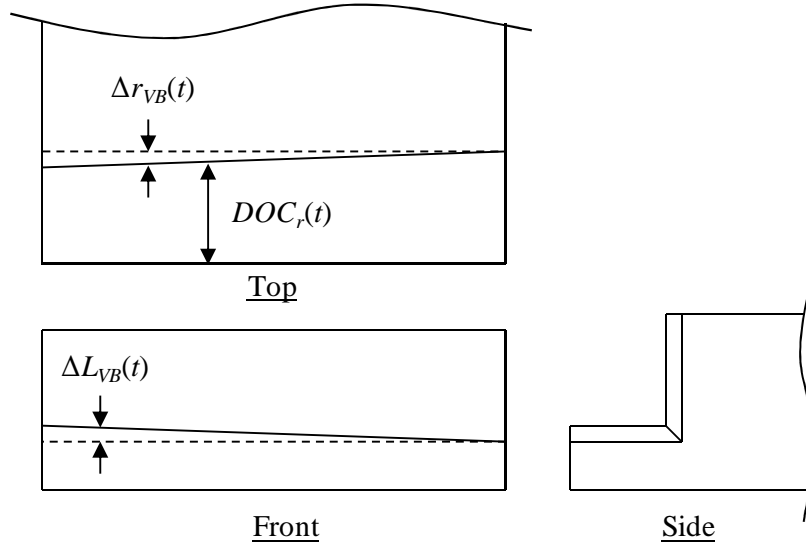


Figure 3.12: Top, front, and side views of a machined pass showing changes due to tool wear.

The depth of cut as a function of time for insert A is shown in equation (3.9),

$$\begin{aligned} b_A(t) &= b_{A,0} - \Delta L_A(t) \\ &= b_{A,0} - \left(\frac{1}{VB_{corr}} \right) \left(VB_{A,0} + VB'_{single} V_{MR,A}(t) \right), \end{aligned} \quad (3.9)$$

where $b_{A,0}$ is the initial depth of cut for insert A, $\Delta L_A(t)$ is the change in tool length due to tool wear for insert A as a function of time, and VB_{corr} is the correlation factor for the flank wear with respect to ΔL of the tool. The equation for $b_B(t)$ is identical to equation (3.9) but with respect to insert B. The radial depth of cut as a function of time for insert A is shown in equation (3.10),

$$\begin{aligned}
DOC_{r,A}(t) &= DOC_{r,A,0} - \Delta r_A(t) \\
&= DOC_{r,A,0} - \left(\frac{1}{VB_{corr}} \right) (VB_{A,0} + VB'_{single} V_{MR,A}(t)),
\end{aligned} \tag{3.10}$$

where $DOC_{r,A,0}$ is the initial uncut chip thickness for insert A, $\Delta r_A(t)$ is the change in cut radius of insert A due to tool wear as a function of time, and VB_{corr} is the same correlation factor as in the depth of cut equation. The flank wear and VB_{corr} is assumed constant around the entire cutting edge. Therefore, the VB_{corr} for the change in radius is the same as for the change in tool length. The equation for $h_B(t)$ is identical to equation (3.13) but with respect to insert B.

The areas of the uncut chips are shown in Figure 3.13. The machine moves the tool at a constant rate in the lateral direction and the amount of wear on a tooth from one rotation to the next is considered negligible. Therefore, the nominal uncut chip thickness is constant, regardless of wear. However, when radial run-out is present, one tooth will remove more material than the other. The uncut chip thickness relationships are shown in Figure 3.13 and, from this figure, the relationship between the nominal feed per tooth, $f_{t,nom}$, and the feed per tooth for inserts A and B is derived, as shown in equation (3.11),

$$2f_{t,nom} = f_{t,A}(t - \tau) + f_{t,B}(t). \tag{3.11}$$

where $f_{t,A}$ and $f_{t,B}$ are the feed per tooth for inserts A and B, respectively, and τ is the time for the tool to rotate 180°. The relationship for τ is shown in equation (3.12),

$$\tau = \frac{180 \cdot 60}{360N} = \frac{30}{N}. \tag{3.12}$$

The feed per tooth for insert B is shown in equation (3.13),

$$f_{t,B}(t) = 2f_{t,nom} - f_{t,A}(t - \tau). \tag{3.13}$$

The previous equations can be written identically with respect to insert A. From equation (2.8), the uncut chip thickness as a function of time for insert A is shown in equation (3.14),

$$h_A(t) = f_{t,A}(t) \sin(6Nt) g(t) \quad (3.14)$$

The area of the uncut chip for insert A is the integral of the difference between the current swept radius of insert A and the previous swept radius of insert B. This is shown in equation (3.15),

$$A_{c,A} = \int_{\theta_s}^{\theta_e} \int_0^r (r_{c,A,t}^2 - r_{c,B,t-\tau}^2) dr d\theta. \quad (3.15)$$

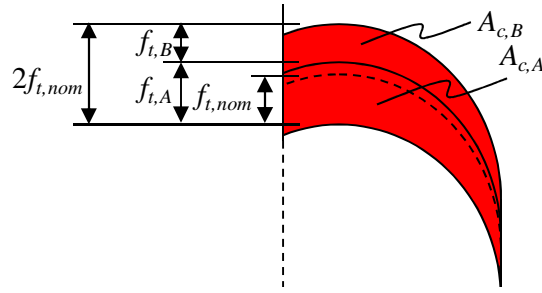


Figure 3.13: Uncut chip thicknesses when run-out is present.

The radial run-out, or difference in the cut radius from insert A to B, as a function of time, $\Delta r_{A,B}(t)$, is shown in equation (3.16),

$$\begin{aligned} \Delta r_{A,B}(t) &= \Delta r_{A,B,0} + \left(\frac{1}{VB_{corr}} \right) (VB_B(t) - VB_A(t)) \\ &= \Delta r_{A,B,0} \\ &\quad + \left(\frac{1}{VB_{corr}} \right) (VB'_{single} V_{MR,B}(t) + VB_{0,single} - VB'_{single} V_{MR,A}(t) - VB_{0,single}) \\ &= \Delta r_{A,B,0} + \left(\frac{VB'_{single}}{VB_{corr}} \right) (V_{MR,B}(t) - V_{MR,A}(t)), \end{aligned} \quad (3.16)$$

where $\Delta r_{A,B,0}$ is the initial radial run-out. The axial run-out, or difference in the cutter length from insert A to B, as a function of time, $\Delta L_{A,B}(t)$, is shown in equation (3.17),

$$\begin{aligned}
\Delta L_{A,B}(t) &= \Delta L_{A,B,0} + \left(\frac{1}{VB_{corr}} \right) (VB_B(t) - VB_A(t)) \\
&= \Delta L_{A,B,0} \\
&\quad + \left(\frac{1}{VB_{corr}} \right) (VB'_{single} V_{MR,B}(t) + VB_{0,single} - VB'_{single} V_{MR,A}(t) - VB_{0,single}) \\
&= \Delta L_{A,B,0} + \left(\frac{VB'_{single}}{VB_{corr}} \right) (V_{MR,B}(t) - V_{MR,A}(t)), \tag{3.17}
\end{aligned}$$

where $\Delta L_{A,B,0}$ is the initial axial run-out. The run-out is considered to equalize when $\Delta r_{A,B}(t)$ and $\Delta L_{A,B}(t)$ are zero or at a time, t_{eq} , as shown in equation (3.18),

$$\Delta L_{A,B,0} = \left(\frac{VB'_{single}}{VB_{corr}} \right) (V_{MR,A}(t_{eq}) - V_{MR,B}(t_{eq})). \tag{3.18}$$

An iterative approach is necessary to solve equation (3.18) because the change in the cutting parameters are functions of the volume of material removed and the volume of material removed is a function of the change in the cutting parameters. In this research, the run-out in the second test is assumed to have equalized by the end of the fourth pass since the wear progresses at a similar rate, beyond that pass, as it does in the other tests.

The measurements made with the tool-setting probe indicated that there was a greater difference in the tool's length and diameter for the second test than the first and third. The wear measurements showed a larger difference for the first two passes of the second test than for the first two passes of the first or third test. Run-out becomes apparent when analyzing the cutting forces because one tooth is removing more material than the other during each pass and it is incurring greater cutting forces. The tooth which removes the most material is the dominant tooth. Figure 3.14 shows the resultant of the x-, y-, and z-forces during the first pass of Tests 1 and 2. Six peaks can be seen in the figure. The peaks represent the engagement of a tooth in the material. Since there are two teeth on the cutter, the data represent three rotations of the tool. The difference in run-out can be seen in the data by examining the change in the peak force from one

tooth to the next, or from the first peak to the second peak, and so on. It can be seen that there is a greater change from peak to peak in the forces for the second test than the first test, which indicates greater run-out. Figure 3.15 also shows the resultant force data for three tool rotations of Tests 1 and 2 but for the fifth pass instead of the first pass. From Figure 3.10 it can be seen that the wear rate has stabilized by the fifth pass and is similar for all three tests. As previously discussed, when run-out is present, the dominant tooth wears faster than the non-dominant tooth in the initial passes because it is bearing a greater load. Eventually, the dominant tooth wears to a point when both teeth remove similar amounts of material. At that point the wear rate will stabilize. The change from peak to peak in the data in Figure 3.15 shows that run-out in the fifth pass of the second test is essentially the same as the run-out for the first test. Therefore, the initial difference between Tests 2 and 1 was eliminated because the dominant tooth has been worn to a point that it is removing the same amount of material as the non-dominant tooth.

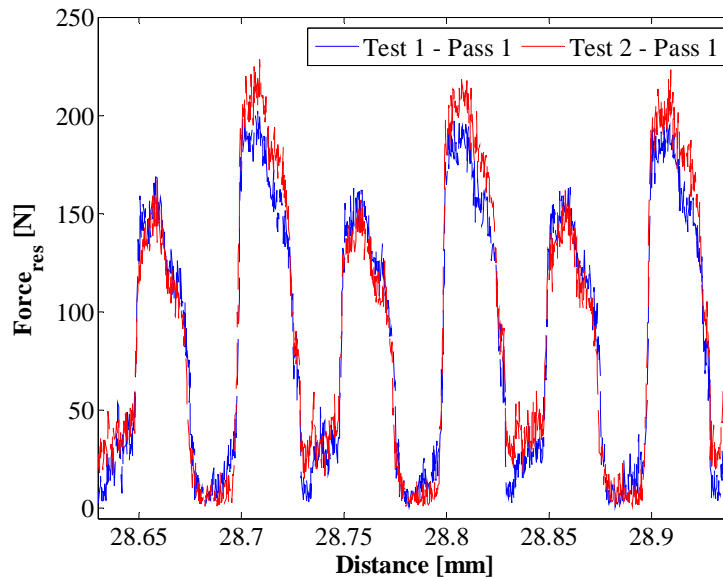


Figure 3.14: Resultant cutting forces for three tool rotations during pass 1 of Test 1 and Test2.

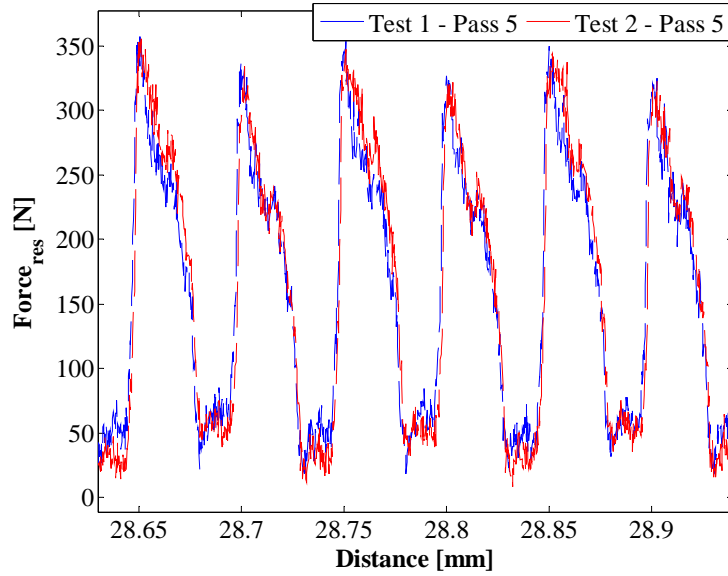


Figure 3.15: Resultant cutting forces for three tool rotations during pass 5 of Test 1 and Test2.

The probe, ΔL , to wear, VB , correlation factor, VB_{corr} , of 8.5 from the Estimation from Probe Measurements section was used to calculate the estimate of VB for each pass in each test. The average and standard deviation for each of the passes in the three tests is represented by the error bar plot in Figure 3.16. The microscope measurements are shown again in this figure to show the correlation between the probe measurements and microscope measurements. The average standard deviation for the probe estimates is $19.3 \mu\text{m}$. This is considered large since, within these tests, the measured VB , typically, ranges from $60 \mu\text{m}$ to $100 \mu\text{m}$. However, the estimates from the probe measurements do increase with a similar rate and the average estimations are within $12 \mu\text{m}$ of the average measurements. The averages of the probe estimates showed the same trend as and are all less than the averages of the microscope measurements by a consistent amount. This could represent an issue with the calculated correlation factor between

the probe measurements and the actual flank wear. As mentioned previously, the probe, ΔL , to wear, VB , correlation factor was determined by measuring angles of the insert under a microscope and correlating with angles provided on the supplier's website. Due to the complex geometry of the insert and the inability to ensure exact alignment of the microscope with the insert while mounted in the cutter body, precise angle measurements were not possible. Also, the supplier was not willing to provide exact geometry of the insert because it was considered proprietary information. However, dividing the microscope measurement by the measured change in tool length and averaging the values resulted in a probe, ΔL , to wear, VB , correlation factor of 10. If the error in the probe estimate is defined as the difference between the average probe estimate and the average microscope measurement, then the average error decreases from $11\mu\text{m}$ to $2\mu\text{m}$ by using a VB_{corr} of 10, rather than 8.5. The results of using the new correlation factor are shown in Figure 3.17. This new correlation factor was used for the calculation of probe estimates through the rest of this work.

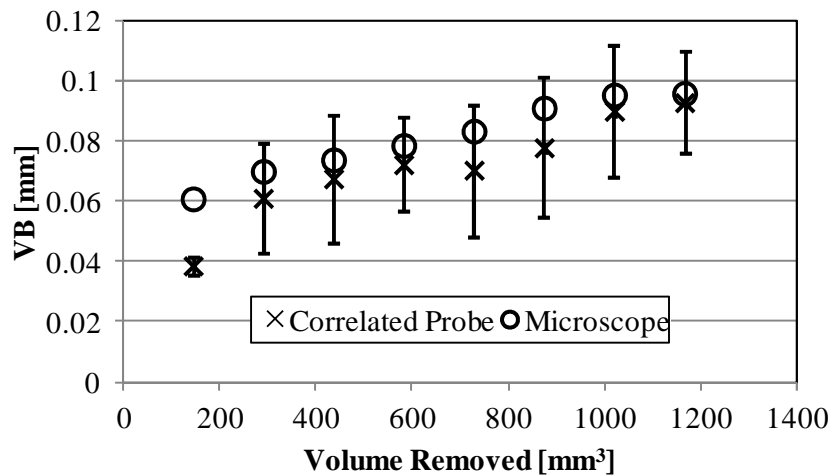


Figure 3.16: Microscope measurements and error bar plot of VB estimates from probe measurements.

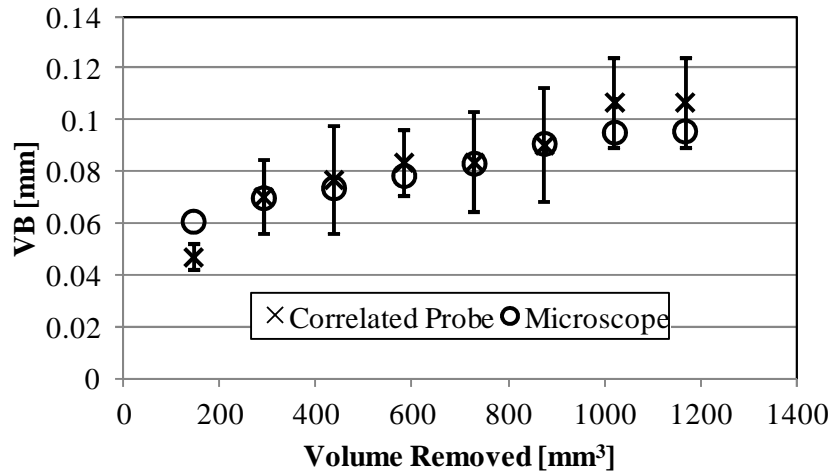


Figure 3.17: Microscope measurements and error bar plot of VB estimates from probe measurements with new correlation factor.

Uncertainty

Since the measurements made in this set of experiments are on the order of micrometers and this is close to the accuracy/precision limits of many machine tools and on-machine probing systems, an uncertainty analysis has been included. The data for the machine tool were taken from a record of the accuracy tests that the manufacturer (Okuma) performed on the particular machine used for these experiments. The data for the probes were found in specifications published by the probe manufacturer (Renishaw). A repeatability study was also conducted on both probes in the machine. The repeatability study was conducted for the spindle probe by measuring a point on a flat surface, then moving the probe out of position and issuing the command for it to measure the same point on the same surface. This was completed 30 times in total and the standard deviation was calculated from the measured values. This standard deviation is the “Measured On-machine” value shown in the list below. A similar method was completed with the tool set station. A tool length was measured, then the tool was moved out of position, the

measurement command was issued to the machine again, and the measurement was recorded. This was also completed 30 times and the standard deviation was calculated from the measured values. All of the data from these sources are summarized in the following list.

- Machine tool coordinate errors [91]
 - Positioning Accuracy (Okuma test results):
 - x-axis: ± 0.0010 mm (Full Travel)
 - y-axis: ± 0.0010 mm (Full Travel)
 - z-axis: ± 0.0010 mm (Full Travel)
 - Repeatability of Positioning (Okuma test results):
 - x-axis: ± 0.0005 mm (per 100 mm)
 - y-axis: ± 0.0005 mm (per 100 mm)
 - z-axis: ± 0.0005 mm (per 100 mm)
- Probe repeatability [20,21]
 - Tool Set Station:
 - Manufacturer Specification: ± 0.001 mm
 - Measured On-machine: $\pm \mathbf{0.002}$ mm
 - Spindle Probe:
 - Manufacturer Specification: ± 0.001 mm
 - Measured On-machine: $\pm \mathbf{0.001}$ mm

These measured repeatability values for the probes indicate that there are 2 μm and 1 μm of uncertainty in the tool set station and spindle probe measurements, respectively. Therefore, when the size of the flank wear is small, the uncertainty can be as much as the measurement itself, thus these measurements made with the probes can lead to significant error in the wear calculations. Even at larger wear sizes (~ 100 μm), the uncertainty is nearly 20% of the measurement for the tool set station. Also, as stated at the end of the previous section, the average of the sample standard deviations for each pass in the tests was 19.3 μm . Accounting for the measured repeatability of the tool set station and VB_{corr} , the expected standard deviation would be

20 μm . The average of the sample standard deviations calculated from the test measurements is within 5% of the expected standard deviation from the probe repeatability. Therefore, these values are logical.

Concluding Remarks

This chapter described the considerations for determining a wear model for use in the Kalman filter. The methods of data collection and test development were also discussed. The expected correlation was developed based on geometric principles, the data from the experiments were analyzed, and the error in the measurement system was discussed. The correlation factor that was originally determined was concluded to be inaccurate and an improved factor was determined from the data and shown to provide better estimates. The error was found to be substantial and it was discussed that there are other factors which should be considered (i.e., run-out). One factor that was not mentioned was the inability of this method to detect notching in the insert's corner and it will be seen in the force modeling chapter that this is significant.

A consideration for implementing this in an actual manufacturing process will be the frequency of measurements. This will be directly tied to material wear rates. As shown in the Data Analysis section of this chapter, a carbide tool would machine a significantly higher volume of steel than nickel-based superalloy before incurring the same amount of wear. Probe measurements increase the cycle time of a machining operation because the tool is not removing material during this time. This must be balanced with the number of measurements necessary to adequately capture the wear progression. This will be application specific. However, the interval between measurements will be longer when machining steel than when machining a γ' -strengthened nickel-based superalloy because the probe is only capable of detecting significant changes in the tool length.

CHAPTER FOUR

ADAPTIVE TOOL WEAR ESTIMATION

The adaptive tool wear estimation was incorporated in this research to provide robust wear estimations. The adaptive estimation is robust because tool wear is stochastic and, as shown in the previous chapter, the touch probe measurement method contains significant variability. An adaptive approach incorporates sensor measurements in conjunction with state predictions from a model and to reflect the actual process when it deviates from the modeled expectation. This is extremely important when machining a γ' -strengthened nickel-based superalloy because process changes occur often and rapidly. Capturing the process deviations due to tool wear allows the deviations to be reflected in other models (i.e., force modeling) and leads to higher accuracy in those models.

Derivation of Specific Kalman Filter Equations

The Kalman filter is often explained from a Bayesian point of view [65]. Bayes theorem uses an assumption to make a prediction about a future event, then uses feedback after the event to improve the assumption, thus refining the assumption over time. This is very similar to the operation of the Kalman filter. The Kalman filter begins with an *a priori* estimate of a state based on a process model. A measurement of the state is made. The measurement is compared to the *a priori* estimate to determine the measurement *innovation*, or residual between measurement and estimate. An *a posteriori* state update is calculated by multiplying the *innovation* by the Kalman gain and adding this to the *a priori* estimate. The Kalman gain is the factor that minimizes the *a posteriori* error covariance. This is accomplished by minimizing the trace of the *a posteriori* error covariance. These steps provide an improved state estimate and allow for a recursive estimate, measure, and improve approach.

The states being estimated in this research were the flank wear, VB , and flank wear rate with respect to the change in volume of material removed, VB' . The state vector, \mathbf{x} , is shown in equation (4.1),

$$\mathbf{x} = \begin{Bmatrix} VB \\ VB' \end{Bmatrix}. \quad (4.1)$$

For this implementation of the Kalman filter the process and measurement covariances were assumed to be constant. In many cases the covariance matrices are considered to be tunable parameters of the Kalman filter. However, in this research they will be estimated based on experimental data. The variance in the tool setting touch probe, σ_{TS}^2 , was determined to be $4 \mu\text{m}^2$ from the probe repeatability study discussed in the Tool Wear Estimation. However, by taking into account the correlation factor between the tool set station measurement and the tool's flank wear, the standard deviation of the measurement would be $20 \mu\text{m}$ and the measurement variance, σ_m^2 , would be $400 \mu\text{m}^2$. The process noise covariance was estimated from the data gathered during this research and previous experimentation. The data have shown that, for a given set of machining conditions, the wear rate is independent of the actual wear amount (Figure 3.10). Therefore, the covariance between VB and VB' is 0. The VB process noise variance was determined by calculating the sample standard deviation of the VB measurements from the microscope. The VB' process noise variance was calculated by determining the sample standard deviation of the VB' from the least squares regression on each set of tool wear test data. The VB process noise variance, σ_{VB}^2 , was estimated to be $36 \mu\text{m}^2$ and VB' process noise variance, $\sigma_{VB'}^2$, was estimated to be $0.01 \mu\text{m}^2/\text{mm}^6$. These values are used in the covariance matrices from equations (2.25) and (2.26) as indicated in equations (4.2) and (4.3),

$$\mathbf{Q} = E[\mathbf{w}_0 \mathbf{w}_0^T] = \begin{pmatrix} \sigma_{VB}^2 & 0 \\ 0 & \sigma_{VB}^2 \end{pmatrix} \quad (4.2)$$

$$\mathbf{R} = E[\mathbf{v}_0 \mathbf{v}_0^T] = (\sigma_m^2). \quad (4.3)$$

Equation (2.29) was used to determine the *a priori* estimate of states. Since the flank wear rate has been observed to be nearly constant in the gradual wear portion of the tool's life, the flank wear rate in the *a priori* estimate is assumed to be constant from the last step to the current step. The *a priori* state estimate is shown with the specific variables for this research in equation (4.4),

$$\hat{\mathbf{x}}_{k,k-1} = \mathbf{A} \hat{\mathbf{x}}_{k-1} = \begin{Bmatrix} VB_{k,k-1} \\ VB'_{k,k-1} \end{Bmatrix} = \begin{pmatrix} 1 & \Delta V_{MR} \\ 0 & 1 \end{pmatrix} \begin{Bmatrix} VB_{k-1} \\ VB'_{k-1} \end{Bmatrix} \quad (4.4)$$

where ΔV_{MR} was the change in volume of material removed from one pass to the next (e.g., volume of material removed per pass), and VB_{k-1} and VB'_{k-1} were the *a posteriori* state estimates from the previous iteration of the filter. VB_{k-1} and VB'_{k-1} needed to be assumed before the first estimation. They were determined based on microscope measurements as discussed in the Data Analysis section of the Tool Wear Estimation chapter. VB and VB' changed with each iteration of the filter as the improved state estimates were determined. The framework of the model from the previous section was used in the development of equation (4.4) but the values derived from the linear fit were only used for the initialization of the Kalman filter.

The measurement equation (2.22) is shown with specific variables for this implementation in equation (4.5),

$$\mathbf{z}_k = \mathbf{H} \mathbf{x}_k + \mathbf{v}_k = \Delta TS_k = \begin{Bmatrix} 1/VB_{corr} & 0 \end{Bmatrix} \begin{Bmatrix} VB_k \\ VB'_k \end{Bmatrix} + \mathbf{v} \quad (4.5)$$

where ΔTS was the change in tool length measured by the tool set station, and VB_{corr} was the correlation factor between the tool set station measurement and the tool's flank wear.

The last filter parameter to determine before implementing the filter was the initial estimate error covariance, \mathbf{P}_0 . If the estimate error covariance was initialized with high values then the Kalman gain would put more weight on the *innovation* and therefore put more weight on the measurement. However, the model estimation would be weighted more heavily if \mathbf{P}_0 were initialized with high values. The initialization would skew the first measurements in one direction or another for the first few iterations but the filter would settle during operation. When machining γ' -strengthened nickel-based superalloys, the tool wear occurs very rapidly and it is not possible to make multiple measurements. With this being the case, the estimate error covariance should be reasonably approximated. To approximate the estimate error covariance matrix, the initial errors between the microscope measurements and model estimates were calculated, averaged, and multiplied per the matrix multiplication as shown in equation (4.6),

$$\mathbf{P}_0 = E[\mathbf{e}_0 \mathbf{e}_0^T] = E \left[\begin{Bmatrix} e_{VB,0} \\ e_{VB',0} \end{Bmatrix} \begin{Bmatrix} e_{VB,0} & e_{VB',0} \end{Bmatrix} \right] = E \begin{bmatrix} e_{VB,0}^2 & e_{VB,0} e_{VB',0} \\ e_{VB',0} e_{VB,0} & e_{VB',0}^2 \end{bmatrix}, \quad (4.6)$$

where $e_{VB,0}$ is the first *VB* state error and $e_{VB',0}$ is the first *VB'* state error. The first *VB* state error was 7 μm , and the first *VB'* state error was $5\text{E-}9 \mu\text{m}/\text{mm}^3$. After determining all of the specific equations, initializing the covariance matrices, and initializing the states, the order of steps from the Kalman filter section of the Literature Review was followed.

Results and Discussion

The equations and algorithm from the previous section were used in conjunction with the data gathered during the tool wear tests described in the Tool Wear Estimation chapter. The resulting filtered estimation, microscope measurements, model estimation, and correlated probe measurements are shown in Figure 4.1, Figure 4.2, and Figure 4.3 for tests 1, 2, and 3, respectively. The filter results for tests one and three have a maximum percent difference of

12.7% and 6.8%, respectively, from the microscope measurements. However, the filtered estimates for test 2 overestimate the measured width of flank wear by a maximum percent difference of 32.4%. This is expected because of the run-out issue for test 2 described in the previous chapter. The filtered data were calculated to be between the probe correlation and the wear model, which was by design. The wear model was adapted every iteration based on the previous model estimate, the measurement, and the Kalman gain. The variance is filtered and the result reflects the estimate with the lowest variance. The model is weighted more heavily than the correlated probe measurement due to the variance in the probe measurement as compared to the variance in the process and, therefore, the estimate will trend more closely with the model. However, a significant change in the probe measurement will cause a response in the filtered data but it will lag to the next iteration of the filter.

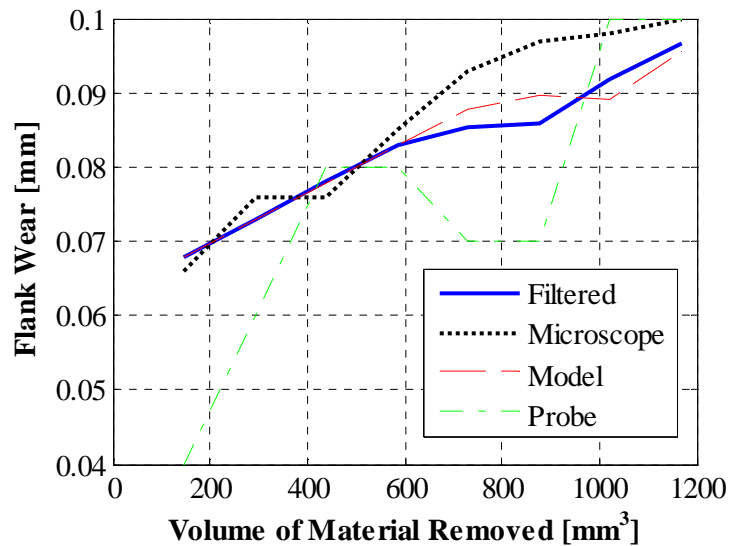


Figure 4.1: Results of the Kalman filter on the data from Test 1.

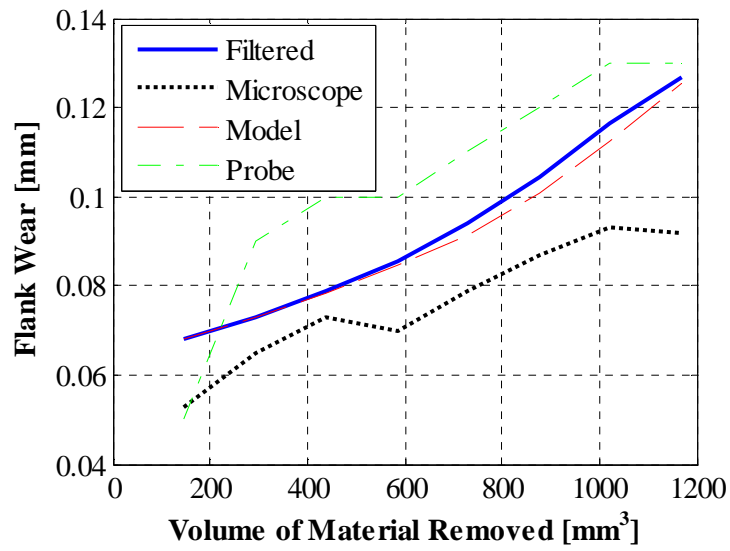


Figure 4.2: Results of the Kalman filter on the data from Test 2.

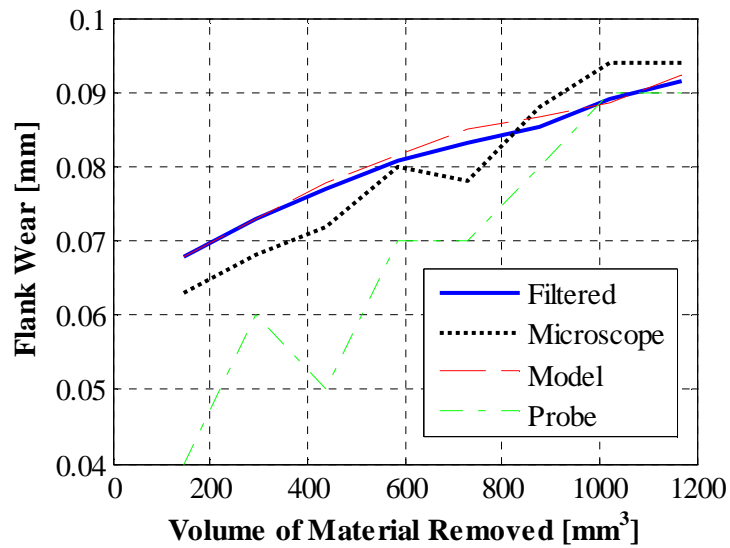


Figure 4.3: Results of the Kalman filter on the data from Test 3.

As mentioned, the overestimation in regards to the second test's data was due to the cutter run-out that was discussed in the Tool Wear Estimation chapter. The run-out caused accelerated wear of one tooth in the initial passes of the test. This was detected by the tool-setting touch probe because the tooth that was removing the most material and therefore experiencing the higher wear rate was the tooth that was driving the maximum length measured by the probe. The accelerated wear on the tooth that was bearing a greater load eventually caused the material removal of the two teeth to equalize and the wear rate became similar to the wear rates in the other tests; however, the change in tool length measurements were already high due to the change during the first couple of passes. Thus, the probe measurements caused the filter to continue predicting at an accelerated rate even though the tool was not actually wearing at that rate.

Concluding Remarks

The Kalman filter was used to integrate a tool wear model and touch probe measurements into an adaptive wear estimation. The necessary equations and relationships were developed and applied to the data collected during three identical tool wear tests. The error of the estimations was determined by examining the difference between the filter estimates and the independent observations from the microscope. The filter estimation error was 12.7% and 6.8% for the first and third tool wear tests, respectively. It was concluded that more run-out was present in the initial passes of the second test and this led to significant error (32.4%) in the last estimate of that test. The mean absolute error in the estimates from the probe measurements for each pass in each test, without the filter, was 17 μm . However, mean absolute error of the filter estimates was 8 μm . Therefore, the Kalman filter reduced the error in the flank wear estimates from the on-machine touch probes by 53%.

A benefit of using a Kalman filter approach is that it is expandable to multiple sensors. Multiple researchers have used the Kalman filter to integrate the output from multiple sensors for

process monitoring [70,71]. In the method presented in this research, a power monitor would be a logical addition. Many researchers have shown the applicability of using power to estimate where a tool is in its life [46,47,51-54]. Similar to touch probes, power monitors are also inexpensive and easily installed a machine tool. The power monitoring approach does not provide any information regarding the actual physical changes of the tool as it wears; however, it does give an indication of the development of a different type wear which the touch probe does not detect and the power monitor is able to measure while the cutting action is taking place. As mentioned in the previous chapter, the touch probe does not detect a notch developing on the inserts edge but the power monitor could. It is assumed that a similar measurement to flank wear correlation is appropriate for measurements with the power monitor as with the tool set station. With this assumption, the Kalman filter measurement equation is written to include a second measurement, as shown in equation (4.7),

$$\mathbf{z}_k = \mathbf{H}\mathbf{x}_k + \mathbf{v}_k = \begin{Bmatrix} \Delta TS_k \\ \Delta P_k \end{Bmatrix} = \begin{bmatrix} 1/VB_{corr,TS} & 0 \\ 1/VB_{corr,P} & 0 \end{bmatrix} \begin{Bmatrix} VB_k \\ VB'_k \end{Bmatrix} + \mathbf{v}, \quad (4.7)$$

where ΔP_k is the change in spindle power from nominal cutting power to the current cutting power at step k , $VB_{corr,TS}$ is the tool set station measurement to flank wear correlation factor, and $VB_{corr,P}$ is the power measurement to flank wear correlation factor. The measurement covariance, \mathbf{R} , becomes a 2x2 matrix. The measurements made with the two sensors are not related to one another and, therefore, the covariance of the two measurements is zero. The measurement covariance is shown in equation (4.8),

$$\mathbf{R} = E[\mathbf{v}_0 \mathbf{v}_0^T] = \begin{bmatrix} \sigma_{TS}^2 & 0 \\ 0 & \sigma_P^2 \end{bmatrix}, \quad (4.8)$$

where σ_{TS}^2 is the variance of the tool set station measurement and σ_P^2 is the variance of the power measurement. All other equations in the derivation of the Kalman filter remain unchanged.

CHAPTER FIVE

FORCE MODEL DEVELOPMENT

The mechanistic force model is based on physical principles and it is manageable from a computation standpoint. It gives insight and understanding into the effects of physical changes on milling forces while also being able to calculate estimates in real-time with limited computational resources. This chapter discusses the feasibility of this model when machining multiple materials, including γ' -strengthened nickel-based superalloys, and presents a new approach for updating a force model which incorporates the physical changes of the tool as it wears allowing rapid tool changes to be captured and resulting forces to be estimated.

Investigate Feasibility of Mechanistic Force Model

This section describes an adaptation of the model including ‘edge effects’ and an approach for determining the cutting coefficients [9]. The edge effects component captures the effects of the tool rubbing on the workpiece and the ploughing effect. The rubbing effect includes the friction between the tool and the workpiece. Figure 5.1 shows a tool engaging the workpiece. The dashed line represents a separation of material that is sheared away and material that was ploughed or pushed. The ploughed material is plastically deformed and remains on the machined surface of the workpiece. The edge effects are constant during the cut of a tooth. This model has been applied to aluminum, steel, and a γ' -strengthened nickel-based superalloy.

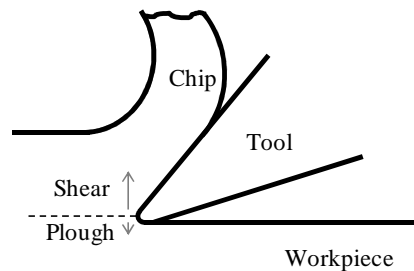


Figure 5.1: Tool engaging the workpiece.

Current Mechanistic Force Model

Figure 5.2 illustrates the normal and tangential cutting forces on the cutter. Equation (2.43) is expanded to normal and tangential components of the cutting force, F_n and F_t respectively, by substituting k_n and k_t for K . The normal force relationship is shown in equation (5.1),

$$F_n = k_n bh \quad (5.1)$$

where k_n is the normal specific cutting force coefficient. The tangential force relationship is shown in equation

$$F_t = k_t bh \quad (5.2)$$

where k_t is the tangential specific cutting force coefficient. Figure 5.3 illustrates the slot milling process and identifies the nomenclature that will be used in the equations throughout this chapter.

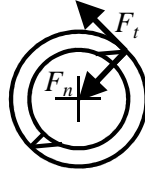


Figure 5.2: Normal and tangential forces on the cutter.

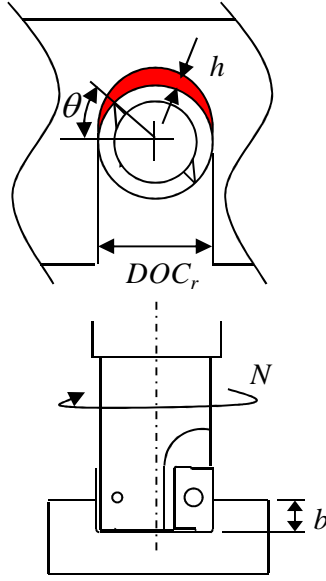


Figure 5.3: Sketch of slot milling process.

The accuracy of the model was improved by the addition of edge effects to the basic equation. As discussed, edge effects were due to the tool rubbing the workpiece and, in this example, were only dependent on the depth of cut because the effect was assumed to be constant in relation to the amount of cutting edge engaged in the cut. The improved model equations are shown below.

$$F_n = k_n b h + k_{ne} b, \quad (5.3)$$

$$F_t = k_t b h + k_{te} b, \quad (5.4)$$

where k is the specific cutting force and the subscript n denotes ‘normal’, t denotes ‘tangential’, and e denotes ‘edge effects’ [9].

In slot milling, when the radial immersion of the tool is 100%, the specific cutting forces can be calculated from the measured x , y , and z components of the cutting force data. The orthogonal components are given by the following equations:

$$F_x = \left(k_t b f_t \frac{\sin 2\theta}{2} + k_{te} b \cos \theta + k_n b f_t \frac{(1 - \cos 2\theta)}{2} + k_{ne} b \sin \theta \right) \cdot g(\theta), \quad (5.5)$$

$$F_y = \left(k_t b f_t \frac{(1 - \cos 2\theta)}{2} + k_{te} b f_t \frac{\sin 2\theta}{2} - k_{ne} b \cos \theta \right) \cdot g(\theta), \quad (5.6)$$

$$F_z = (-k_a b f_t \sin \theta - k_{ae} b) \cdot g(\theta), \quad (5.7)$$

where $g(\theta)$ is a switching function which is one when θ is between θ_s and θ_e , and zero when it is outside the interval.

The methodology for determining the specific cutting coefficients is discussed by Schmitz and Smith (2009) [9]. The average cutting forces in the x-, y-, and z-directions were determined by integrating equations (5.5) - (5.7) with respect to theta, as shown in equations (5.8) - (5.10),

$$\begin{aligned} \bar{F}_x &= \frac{N_t b}{4\pi} \int_{\theta_s}^{\theta_e} (k_t f_t \sin 2\theta + 2k_{te} \cos \theta + k_n f_t - k_n f_t \cos(2\theta) + 2k_{ne} \sin \theta) d\theta \\ &= \frac{N_t b}{4\pi} \left[-\frac{k_t}{2} f_t \cos 2\theta + 2k_{te} \sin \theta + k_n f_t \theta - \frac{k_n}{2} f_t \sin(2\theta) + 2k_{ne} \cos \theta \right]_{\theta_s}^{\theta_e}, \end{aligned} \quad (5.8)$$

$$\begin{aligned} \bar{F}_y &= \int_{\theta_s}^{\theta_e} \left(k_t b f_t \frac{(1 - \cos 2\theta)}{2} + k_{te} b f_t \frac{\sin 2\theta}{2} - k_{ne} b \cos \theta \right) d\theta \\ &= \left[\frac{N_t b f_t}{8\pi} (k_t (2\theta - \sin 2\theta) + k_n \cos 2\theta) - \frac{N_t b}{2\pi} (k_{te} \cos \theta) + k_{ne} \sin \theta \right]_{\theta_s}^{\theta_e}, \end{aligned} \quad (5.9)$$

$$\begin{aligned} \bar{F}_z &= \int_{\theta_s}^{\theta_e} (-k_a b f_t \sin \theta - k_{ae} b) d\theta \\ &= \left[\frac{N_t b}{2\pi} (k_a f_t \cos \theta - k_{ae} \theta) \right]_{\theta_s}^{\theta_e}. \end{aligned} \quad (5.10)$$

In a slot milling operation θ_s is 0° and θ_e is 180° . The following equations result from using these limits slot milling limits for θ_s and θ_e in equations (5.8) - (5.10):

$$\bar{F}_x = \frac{N_t b k_n}{4} f_t + \frac{N_t b k_{ne}}{\pi} \quad (5.11)$$

$$\bar{F}_y = \frac{N_t b k_t}{4} f_t + \frac{N_t b k_{te}}{\pi} \quad (5.12)$$

$$\bar{F}_z = -\frac{N_t b k_a}{\pi} f_t - \frac{N_t b k_{ae}}{2} \quad (5.13)$$

The general form of these equations is the equation of a line with the feed per tooth (f_t) as the independent variable and the average force (\bar{F}) as the dependent variable. The equations for the specific cutting force coefficients were derived from equations (5.11) - (5.13) and are given by equations (5.14) - (5.19).

$$k_n = \frac{4a_{1x}}{N_t b}, \quad (5.14)$$

$$k_{ne} = \frac{\pi a_{0x}}{N_t b}, \quad (5.15)$$

$$k_t = \frac{4a_{1y}}{N_t b}, \quad (5.16)$$

$$k_{te} = \frac{\pi a_{0y}}{N_t b}, \quad (5.17)$$

$$k_a = -\frac{\pi a_{1z}}{N_t b}, \quad (5.18)$$

$$k_{ae} = -\frac{2a_{0z}}{N_t b}, \quad (5.19)$$

where N_t is the number of teeth on the cutter, a_1 is the slope of a line which is fit to the average force versus feed per tooth points from the measured data, and a_0 is the extrapolated cutting force at a feed rate of zero, for all three orthogonal force components. Figure 5.4 shows a_1 and a_0 in relation to the average force and feed per tooth [9].

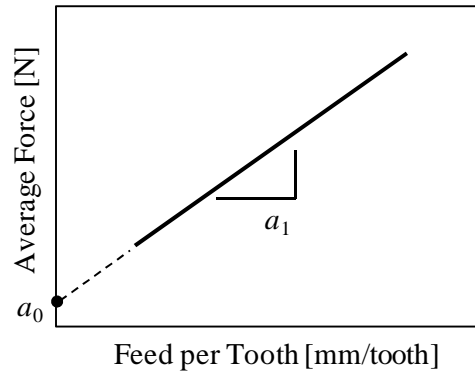


Figure 5.4: Graph showing a_1 and a_0 .

Preliminary Model Investigation

The model was validated using slot milling tests on Aluminum 6061-T6 and Steel 4140. An indexable, 15.875 mm diameter, two insert end mill was used for both sets of tests. APKT style inserts were used, but a more wear resistant insert material and coating was used for the steel test than was used for the aluminum test. The cutting parameters for the tests are shown in Table 5.1 and Table 5.2.

Table 5.1: Cutting parameters for the Aluminum slot milling tests.

Test #	Feed Rate [mm/tooth]	Surface Speed [m/min] ([rev/min])	Axial Depth of Cut [mm]
1	0.025	200 (4010)	0.5
2	0.075	200 (4010)	0.5
3	0.125	200 (4010)	0.5

Table 5.2: Cutting parameters for the Steel slot milling tests.

Test #	Feed Rate [mm/tooth]	Surface Speed [m/min] ([rev/min])	Axial Depth of Cut [mm]
1	0.025	30 (600)	0.5
2	0.075	30 (600)	0.5
3	0.125	30 (600)	0.5

Figure 5.5 shows the average force as a function of feed per tooth with lines fit to the points for the aluminum slot milling tests. A least squares fit was used to determine the a_1 and a_0 parameters from the average force versus feed per tooth for each force direction. The parameters were used to determine the cutting force coefficients (Table 5.3). The modeled forces using these coefficients are shown in Figure 5.6 and compared to the experimental results. The resultant force represents the each direction of the cutting forces and the maximum error between the model and measured forces is 6.7%.

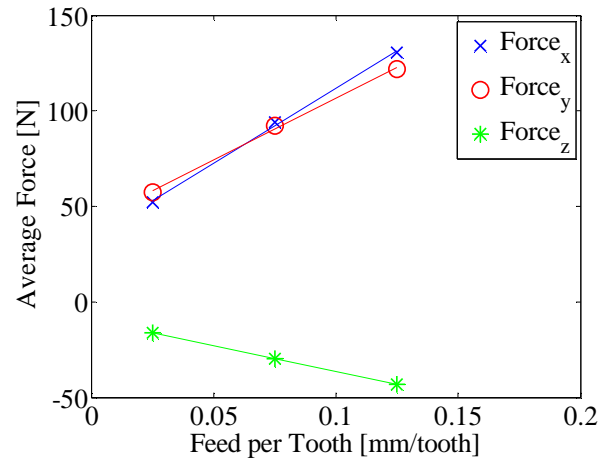


Figure 5.5: Average force versus feed per tooth for Aluminum.

Table 5.3: Cutting force coefficients for Aluminum slot tests.

Coefficients [units]	Values
k_n [N/mm ²]	2580
k_{ne} [N/mm]	133
k_t [N/mm ²]	3140
k_{te} [N/mm]	105
k_a [N/mm ²]	844
k_{ae} [N/mm]	19.1

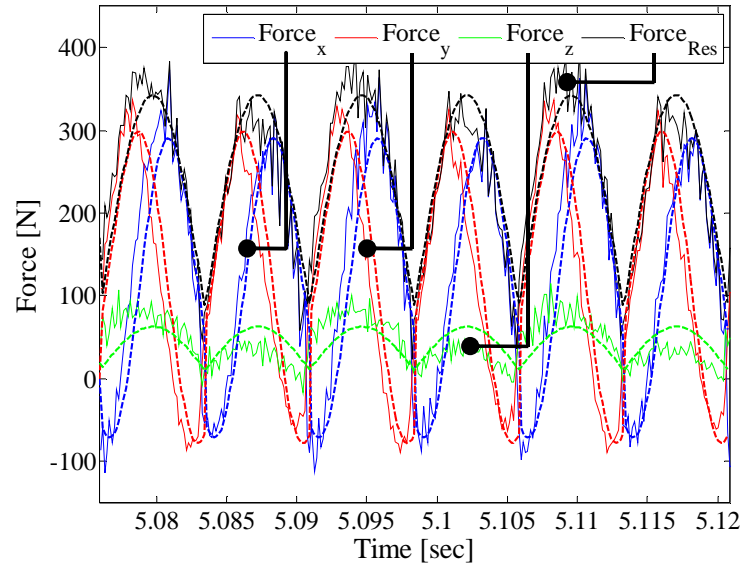


Figure 5.6: Model on real data for three tool rotations during slot milling of Aluminum (test 3).

Similar modeling was performed for forces during the milling of steel. Figure 5.7 shows the average force as a function of feed per tooth with lines fit to the points for the steel slot milling tests. As with aluminum, the cutting force coefficients were calculated for the steel slot milling tests and the force model was generated. The cutting force coefficients are shown in Table 5.4. The experimental data and the model are shown in Figure 5.8, and the maximum error between the measured and modeled resultant forces was 22.2%.

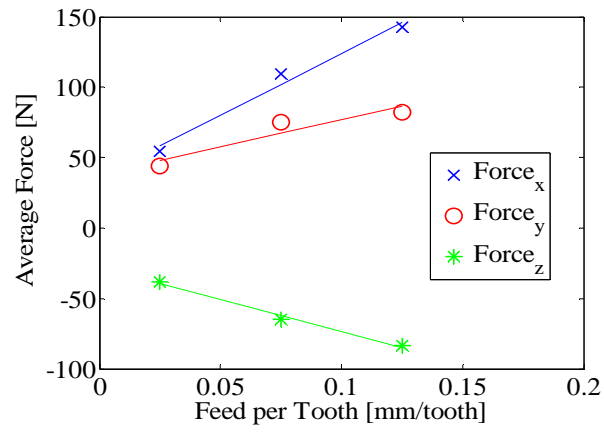


Figure 5.7: Average force versus feed per tooth for Steel.

Table 5.4: Cutting force coefficients for steel slot milling tests.

Coefficients [units]	Values
k_n [N/mm ²]	1530
k_{ne} [N/mm]	121
k_t [N/mm ²]	3520
k_{te} [N/mm]	113
k_a [N/mm ²]	1430
k_{ae} [N/mm]	56.3

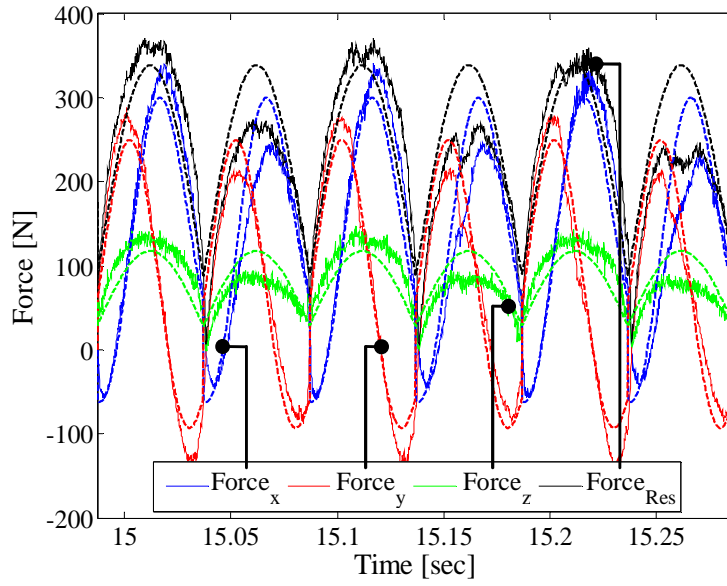


Figure 5.8: Model on real data for three tool rotations during slot milling of Steel (test 3).

Similar tests were conducted on the nickel-based superalloy. The same cutter and insert shape, but with PVD coating, were used and the cutting parameters are shown in Table 5.5. The parameters are less aggressive than the parameters for steel and aluminum. They were chosen based on experience machining these materials. The cutting parameters shown in the table provide relevant force data for the duration of the cutting experiment.

Table 5.5: Cutting parameters for the slot milling tests performed on the nickel-base superalloy.

Test #	Feed Rate [mm/tooth]	Surface Speed (RPM) [m/min] ([rev/min])	Axial Depth of Cut [mm]
1	0.025	25 (501)	0.25
2	0.035	25 (501)	0.25
3	0.04	25 (501)	0.25
4	0.05	25 (501)	0.25

A least squares fit was used to determine the a_1 and a_0 parameters for the nickel-based superalloy milling tests. The line was plotted with the data points and is shown in Figure 5.9. The cutting force coefficients for the first test are shown in Table 5.6.

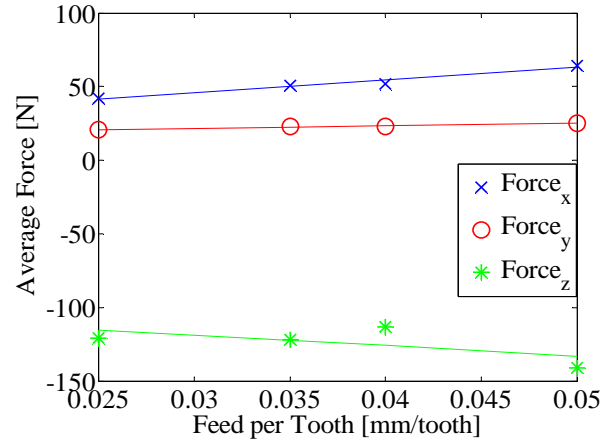


Figure 5.9: Average forces versus feed per tooth for each slot milled in the superalloy.

Table 5.6: Cutting coefficients for superalloy (test 1).

Coefficients [units]	Values
k_n [N/mm ²]	2970
k_{ne} [N/mm]	60.4
k_t [N/mm ²]	7240
k_{te} [N/mm]	83.0
k_a [N/mm ²]	5750
k_{ae} [N/mm]	245

The model prediction was compared with the experimental data, for three consecutive rotations of the tool in the beginning of a pass in Figure 5.10. Cutter run-out is observed in the experimental data, thus the forces vary from one tooth to the other, while the model remains the same. This is considered to be a good model fit because it is a good correlation to the average

force of the two teeth and the model is considered to be applicable to this nickel-based superalloy. The effects of run-out are more apparent due high strength of the nickel-based superalloy and a slight variation in the chip load on the cutting tooth results in a significant force difference. The maximum percent difference between the resultant force measurement and model is 20% but the error between the average measured resultant force and the model is 2%, in the beginning of the pass as shown in Figure 5.10. However, maximum percent difference between the resultant force measurement and model is 33% and the error between the average measured resultant force and model is 20%, in the end of the pass as shown in Figure 5.11. This reinforces the need for an improved cutting force model that accounts for the rapid tool wear incurred when milling nickel-based superalloys.

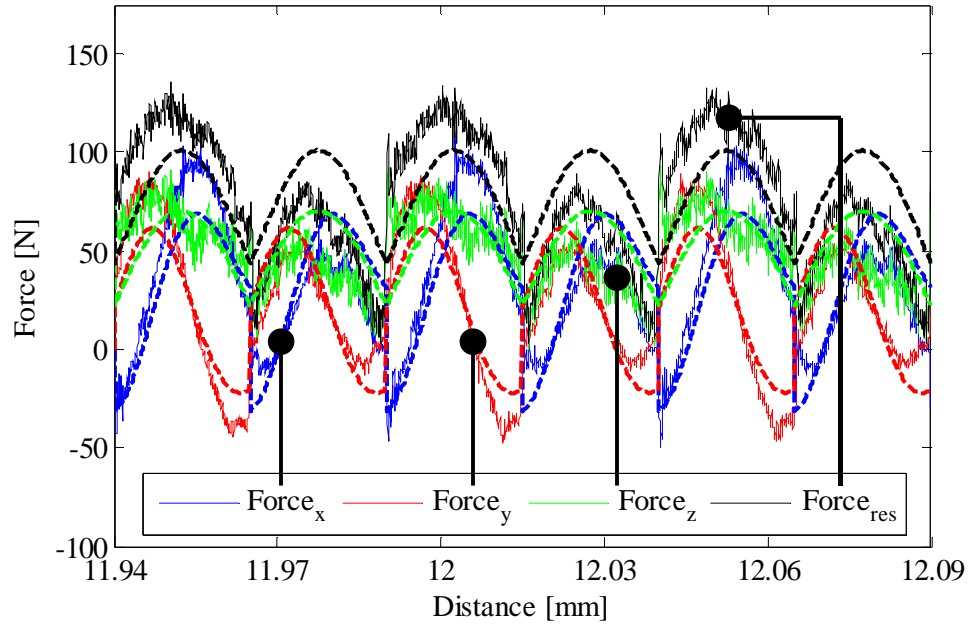


Figure 5.10: Model on real data for three tool rotations during milling of superalloy (beginning).

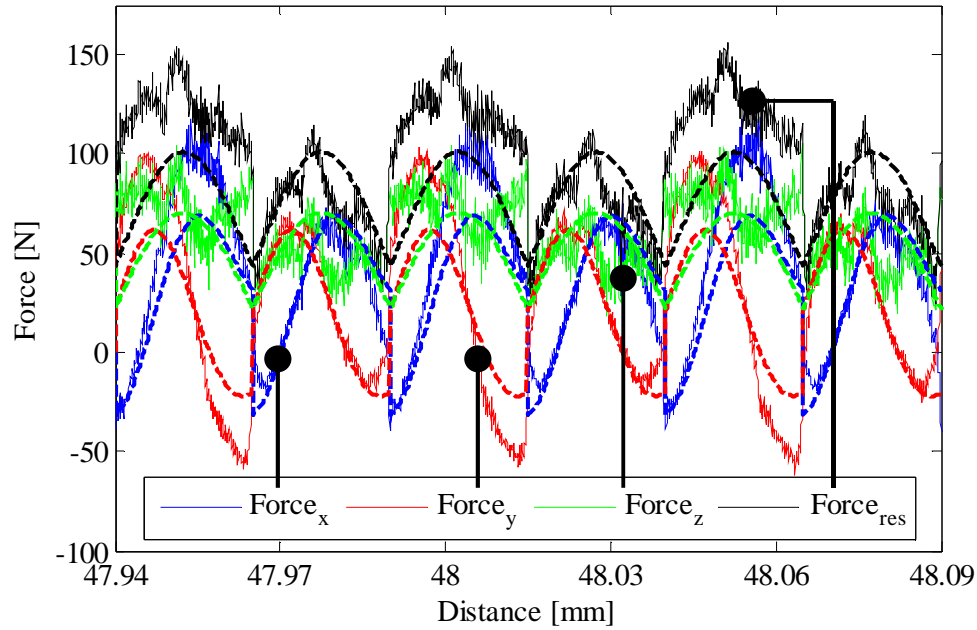


Figure 5.11: Model on real data for three tool rotations during milling of superalloy (end).

Incorporate Wear into the Force Model

Figure 5.12 shows the average cutting forces for the fourth nickel-based superalloy test. As previously stated, it can be seen from this figure that the forces at the end of the pass are significantly higher than the forces at the start. To observe the effect of this change on the cutting force model for multiple cutting parameters, further testing was completed using the parameters in Table 5.7. These parameters encompass a broad range of cutting forces. Subsets, or windows, of data were used to determine the cutting coefficients in the beginning, middle, and end of the cutting pass. The subsets of data consisted of the cutting forces from 80 tool rotations and were extracted from the same beginning, middle, and end locations for each pass. Examples of the beginning, middle, and end subsets are shown as orange boxes in Figure 5.12. The average cutting forces for each, beginning, middle, and end, location were plotted with respect to the feed

rate for each particular cutting speed and depth of cut combination. The specific cutting coefficients were calculated by determining a_0 and a_1 using the least squares fitting method as previously discussed in this section. This methodology is shown in the flow chart in Figure 5.13. The effects of the progression of wear on cutting forces are reflected in the change of these cutting parameters.

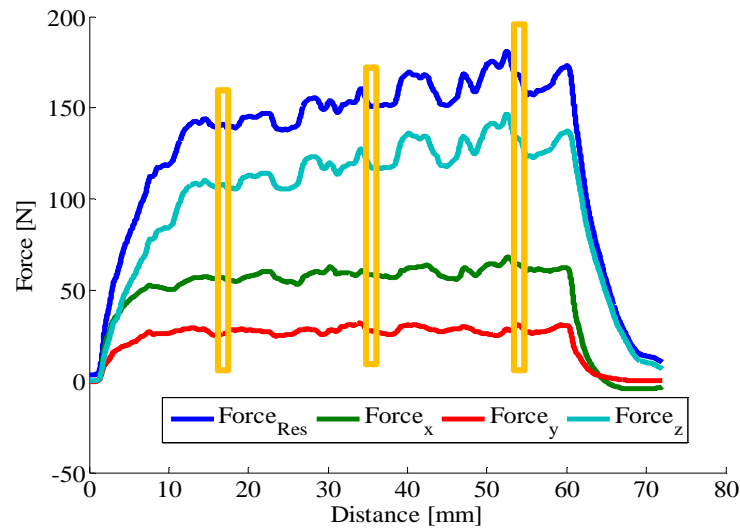


Figure 5.12: Average cutting forces during the fourth nickel-based superalloy test.

Table 5.7: Cutting parameters for

Test #	Feed Rate [mm/tooth]	Surface/spindle speed [m/min]/[rev/min]	Axial depth of cut [mm]
1,2,3	0.025, 0.375, 0.05	25 (501)	0.25
4,5,6			0.50
7,8,9		50 (1002)	0.25
10,11,12			0.50

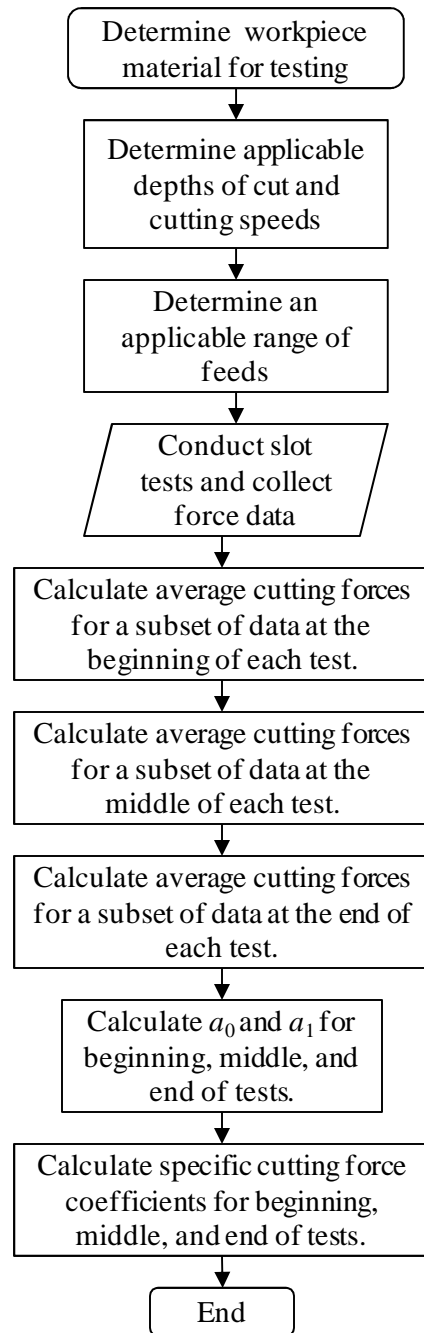


Figure 5.13: Flow chart for determining tool wear effect on force coefficients.

The methodology, shown in Figure 5.13, for determining the specific cutting forces at the beginning, middle, and end of the cutting pass was followed and the chip area coefficient and edge-effect coefficients were determined for multiple spindle speeds and depths of cut over a range of volumes of removed material [92]. Tool wear increases as the volume of material removed increases. The change in chip area and edge-effect coefficients with respect to the volume of material removed is shown in Figure 5.14.

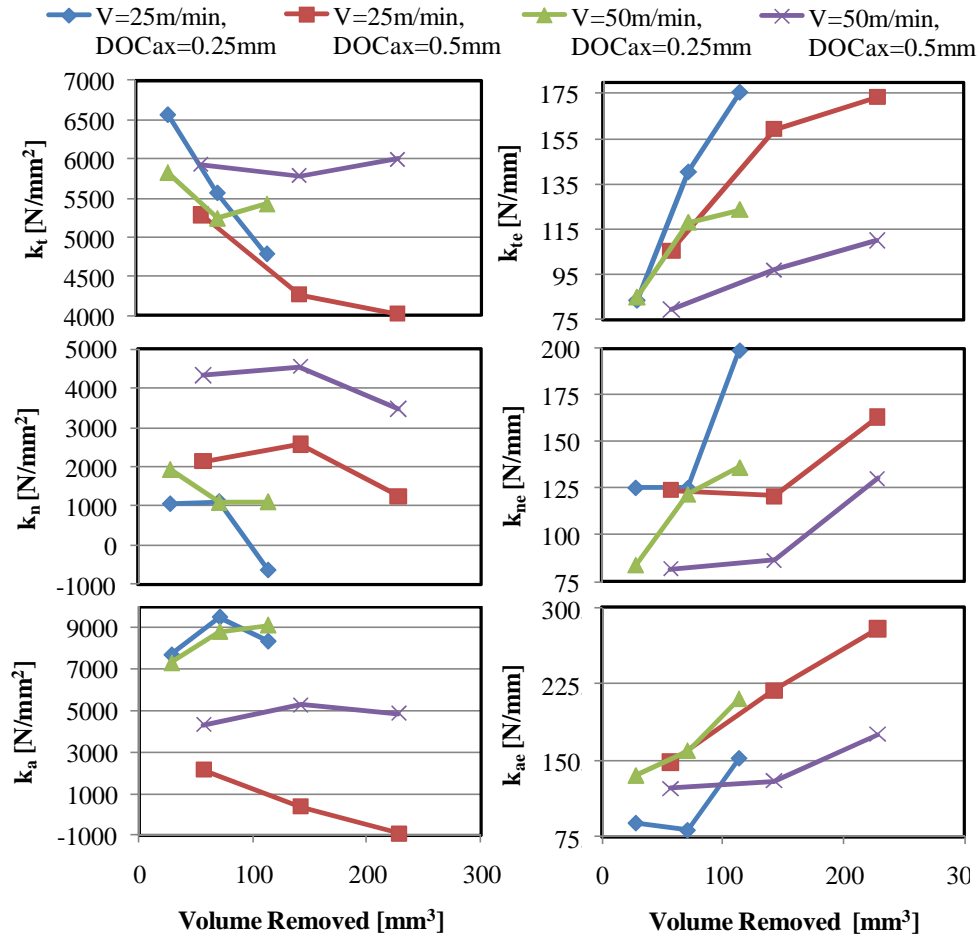


Figure 5.14: Change in chip area and edge effect coefficients with respect to volume of material removed.

The data in Figure 5.14 show that in general, as wear increases, the normal and tangential chip area components decrease while the normal and tangential edge-effect components increase. The increase from the edge-effect components is greater than the decrease from the chip-area components and, overall, the cutting forces increase. As the tool wears, the effective depth of cut decreases due to the cutter material that is being eroded away. Therefore, the force component from chip area decreases. Also, as the tool wears, the size of the flank wear land (VB) increases. Therefore, more rubbing occurs between the cutting edge and the material, and the component of the force that is attributed to the edge effects increases. These results indicate that the model can be improved by incorporating the geometric changes of the tool to account for tool wear.

New Approach for an Updated Model

A major component of this research is the model which defines the behavior between the physical aspects of the tool wear and the resulting forces. A proposed mechanistic force model which includes physical tool wear parameters is shown in equation (5.20),

$$F(t) = k_A b(t) h + k_{e,l} l_e(t) + k_{e,VB} VB(t), \quad (5.20)$$

where k_A , $k_{e,l}$, and $k_{e,VB}$ are experimentally determined material specific coefficients, l_e is the length of the edge that is in contact with the material, and b and VB are the axial depth of cut and size of flank wear, respectively, but are now functions of time. The edge effects component is divided into two new components. The edge length component, $k_{e,l} l_e(t)$, essentially replaces the edge effect component from the original model but the edge length is used in the place of the depth-of-cut. The edge length adjustment is made because in the case of shallow depths-of-cut, as in this research, more of the bottom edge is in contact with the workpiece surface than the side

edge. In side milling applications, this is not the case and the depth-of-cut approximation is appropriate. The edge length is also a function of time. This is represented by equation (5.21),

$$l_e(t) = l_{e,0} - \Delta b(t), \quad (5.21)$$

where $l_{e,0}$ is the initial edge length and $\Delta b(t)$ is the change in depth-of-cut over time. The flank wear adjustment is made because as the size of the flank wear increases, the contact area between the insert and machined surface increases and the amount of sliding friction increases. Figure 5.15 shows effect of tool wear on the edge contact area. As the tool wears the wear land increases, resulting in an increase of contact area, $VB(t)$. The effective depth of cut (b) decreases as the tool wears. Therefore, the component of the force which is related to the chip area decreases. The diameter of the cut made by an insert also changes as a tool wears; however, this does not affect the chip thickness that is cut during a rotation of the insert. This is because the change in the insert size from one pass of a tooth to the next is insignificant. Figure 5.16 shows the effect of tool wear on the chip area. As the bottom and side of the cutting edge is worn away, the depth of cut decreases but the uncut chip thickness does not. The depth of cut at tooth pass n is ΔL less than the initial depth of cut, b_0 . The uncut chip thickness at tooth pass n is the same as the initial uncut chip thickness because the wear on the radius is insignificant from one tooth passing to the next. Figure 5.16 also shows the contact edge length. It is represented by the bold lines. The solid bold line that represents to bottom of the insert and wraps around the side up to the initial depth-of-cut is the initial contact edge length, $l_{e,0}$, and the bold dashed line represents the contact edge length at tooth pass n .

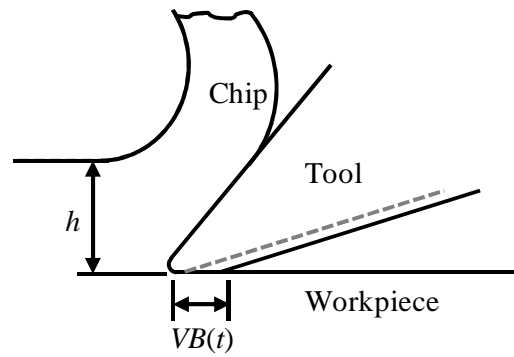


Figure 5.15: Wear progression in relation to the cutting action.

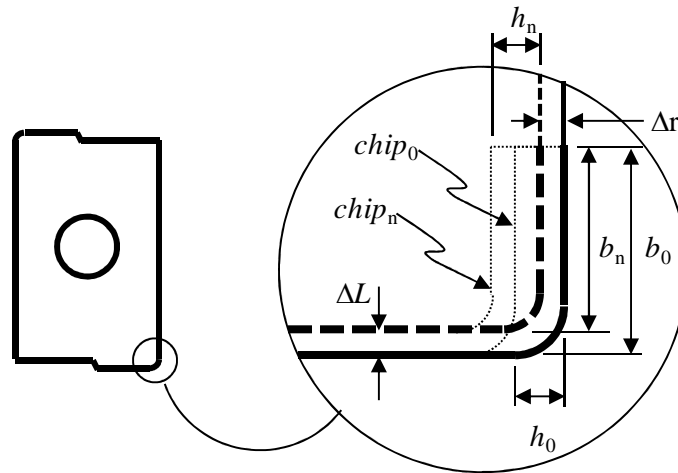


Figure 5.16: The effect of tool wear progression on chip size.

The change in contact edge length is negligible, resulting in a constant force component. It also becomes significantly smaller than the flank wear term. The true benefit of including the contact edge length term is so that the edge component of the force is not zero when the tool is new. However, this becomes negligible over time and this term may be dropped from the equation. The decrease in the chip area component over time is small due to the small changes in the depth-of-cut, but it is easily determined and implemented. The increase in cutting forces due

to the increase of the flank wear is crucial to this research and to the modeling of cutting forces for γ' -strengthened nickel-based superalloys. Therefore, the flank wear component will also remain. The resulting model is shown in equation (5.22),

$$F(t) = k_A b(t) h + k_e V B(t). \quad (5.22)$$

To illustrate the changes due to tool wear as they relate to the forces, two plots are shown in Figure 5.17 depicting the change in cutting force components as the tool wears using equation (5.22). The chip area component decreases by a small amount compared to the large increase in the edge-effect component. Thus, there is an overall increase in the cutting forces.

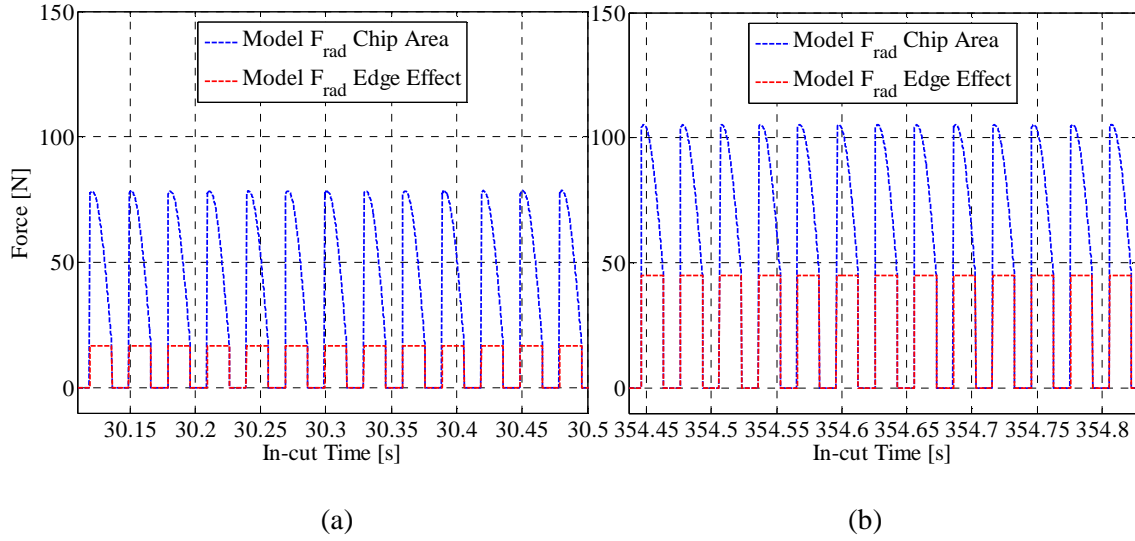


Figure 5.17: Plot of model components when the tool is (a) new and (b) worn.

Concluding Remarks

The mechanistic cutting force model for milling is capable of estimating cutting forces when milling aluminum, steel, and nickel-based superalloys. The calculation of new cutting force coefficients, due to substantial wear after a relatively small amount of material was machined, illustrates the need for a new approach of including this rapid tool wear effect. A new model was proposed, described, and justified with the evolution of the specific cutting force coefficients as the tool wore. The model is simplified for real implementation and the actual effects of the new model changes are illustrated.

CHAPTER SIX

VALIDATION OF THE NEW MODEL APPROACH

In this chapter, the tool wear estimations from the Tool Wear Estimation chapter are integrated with the new force model presented in the Force Model Development chapter. This approach addresses the effects of tool wear on cutting forces. The wear estimates are generated based on probe measurement data after each pass. Tool wear is linearly interpolated between the wear estimate at the beginning and end of a pass. The interpolated wear estimates are used to calculate the cutting forces for an entire cutting pass. The wear estimates for each test are shown in Table 6.1. The change in depth of cut was calculated from the wear estimate, using the tool set station to flank wear correlation factor, VB_{corr} , from the Tool Wear Estimation chapter.

Table 6.1: Improved wear estimates from Kalman filter.

Pass #	VB_1 [mm]	VB_2 [mm]	VB_3 [mm]
0	0	0	0
1	0.067	0.067	0.067
2	0.071	0.074	0.071
3	0.076	0.081	0.073
4	0.081	0.089	0.076
5	0.083	0.097	0.079
6	0.085	0.105	0.083
7	0.092	0.115	0.088
8	0.097	0.122	0.093

Since the model has changed and the cutting parameters are different now than in the previous testing, the coefficient values will differ from the values calculated for the γ' -strengthened nickel-based superalloy in the Force Model Development chapter. The cutting coefficients are intended to be independent of cutting parameters but the reality is that there are still influences from the operation which are not be explicitly captured in the model and therefore

the coefficients will vary. The effects from the reduction of the depth-of-cut as the tool wears were small and therefore nearly negligible. Thus, a change in the chip area coefficients resulted in up or down shifts in the magnitude of forces. The flank wear component drastically changes over the duration of the test and has a significant effect on the slope of the data. The coefficients for the updated model were determined by reducing the error between the data and the model predictions for the three tests. The flank wear/edge effects coefficient was adjusted to minimize the error in the overall slope of the data while the chip area coefficient was adjusted in order to minimize the magnitude of the force error. The model coefficients are shown in Table 6.2. The forces in the z-direction were not modeled in this new approach because there are additional effects of the tool wear affecting those measurements. The notch which forms on the radial edge of the tool at the top of the depth-of-cut causes additional forces in the z-direction which are not captured in this modeling approach.

Table 6.2: Model coefficients for updated force model.

Coefficients [units]	Values
k_n [N/mm ²]	2200
k_{ne} [N/mm]	775
k_t [N/mm ²]	4500
k_{te} [N/mm]	850

Results and Discussion

The normal and tangential cutting forces provide data that are always in the same direction, as far as positive or negative, and provide a clearly defined peak at maximum chip thickness. In this research, the maximum chip thickness occurs at a 90° cutter rotation angle, or when the cutting edge of tool is aligned with the y-axis. The force relationships in regards to the

cutting tool are shown in Figure 6.1. The average and standard deviation of these maximum normal and tangential cutting forces provides a simple method of condensing the data for comparison purposes. Calculating average and standard deviation of the normal and tangential cutting forces was accomplished by resolving the cutter angle from the force data, then applying an axis transform. Once the normal and tangential forces had been calculated, a window of data were extracted between 89.5° and 90.5° for each tooth engagement within the cutting data between 8 mm and 59 mm travel distance and the data's mean and standard deviation were calculated. The cutter was at full engagement between 8 mm and 59 mm and there would be no transient effects from entry into or exit from the material. A similar method was performed in order to condense the model data. The error bar plot in Figure 6.2 shows the calculated average and standard deviation for the measured force data and the average for the modeled data for each pass within the first cutting test. The error bars represent the deviation that occurs over the length of a single pass. Therefore, Figure 6.3 and Figure 6.4 show the same data for the second and third cutting test, respectively.

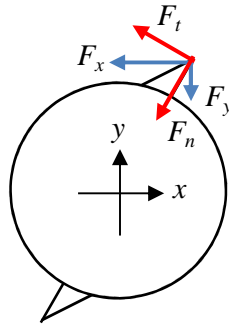


Figure 6.1: Cutting forces in the normal (n), tangential (t), x-, and y-directions.

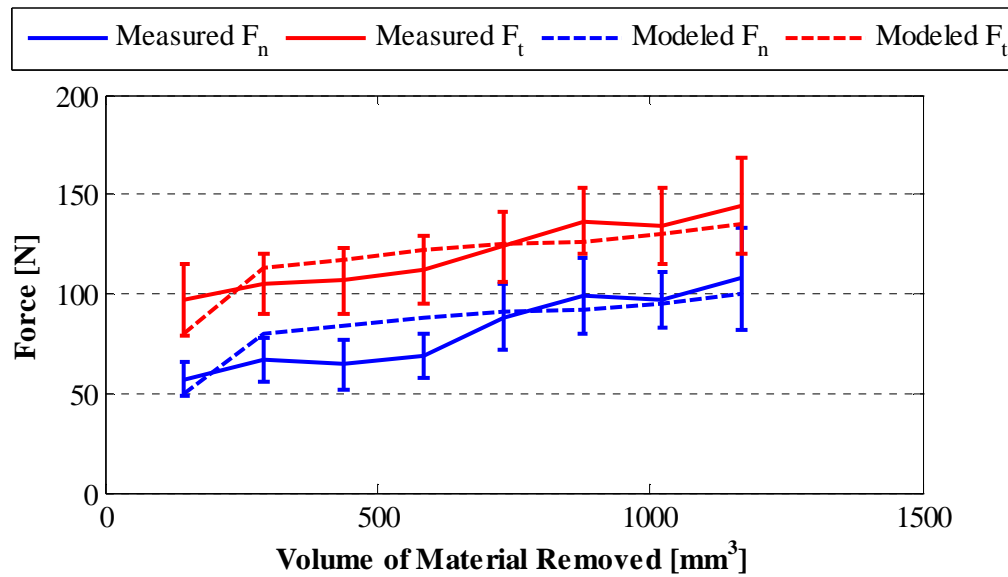


Figure 6.2: Comparison of average measured and modeled cutting forces as a function of volume of material removed for Test 1.

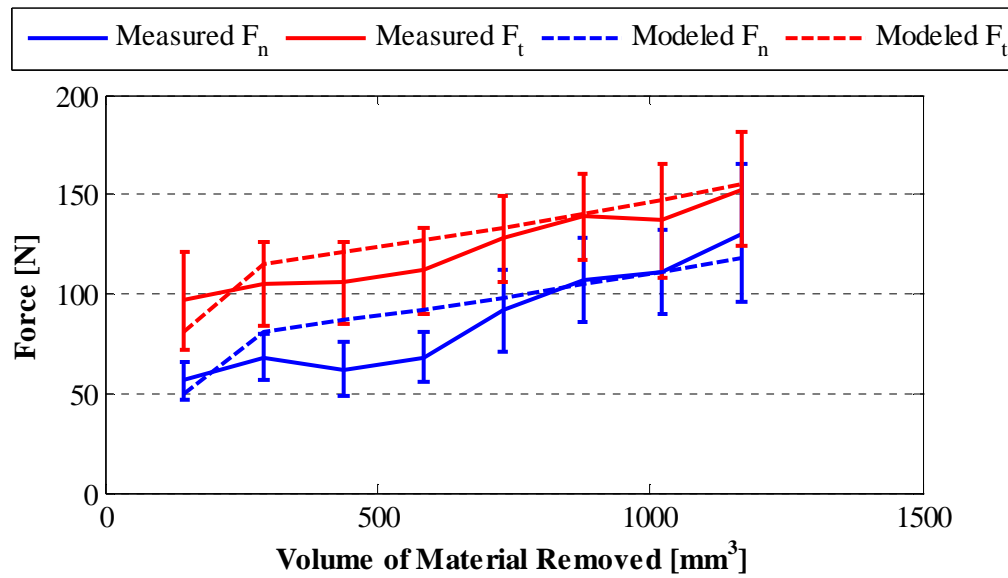


Figure 6.3: Comparison of average measured and modeled cutting forces as a function of volume of material removed for Test 2.

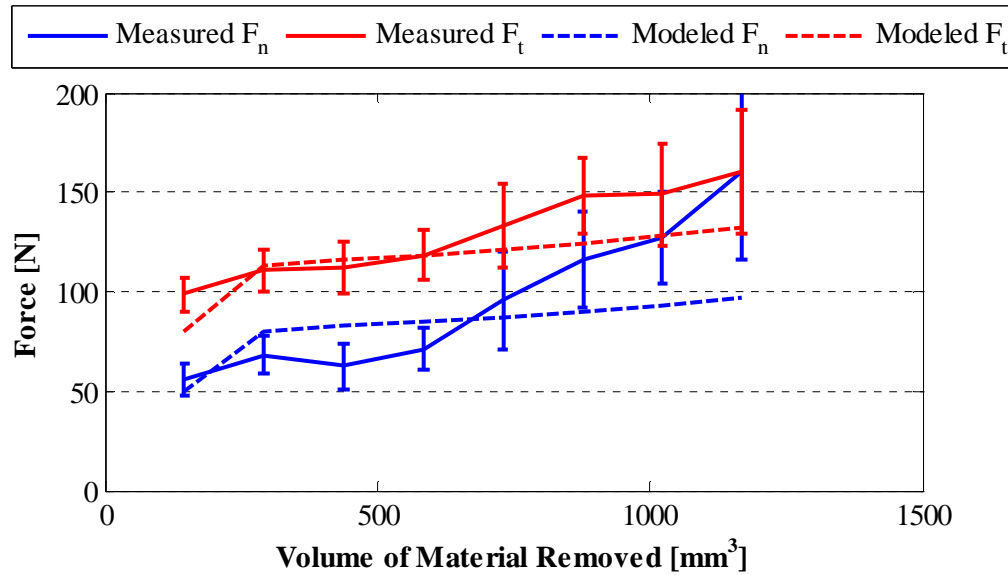


Figure 6.4: Comparison of average measured and modeled cutting forces as a function of volume of material removed for Test 3.

Overall, the model for the first and second test trend with the measured data for each pass except the third and fourth passes. The largest percent difference between the modeled and measured data was 32% for the radial force data after the third pass of test 1 and 38% for the radial force data after the third pass of test 2. The measured wear data from the microscope reflect a reduction in the wear rate for the early passes of tests one and two. The probe also detected a change for these passes in the second test. However, this was not reflected in the filtered estimate due to the high variance associated with the probe measurements. Therefore, the filtered estimate was essentially linear and this causes the errors seen in the forces of the initial passes. The percent difference ranged between 0% and 8% for both force components in the last four passes of tests 1 and 2. The latter passes are the primary concern for estimating subsurface damage because higher cutting forces correlates with greater subsurface damage and the highest cutting forces occur in the latter passes.

The model under predicted the cutting forces in the latter passes of the third test. The maximum errors were percent differences of 40% and 18% between the measurements and model estimation of the normal and tangential cutting forces, respectively, after the eighth pass. In each test, a notch began to develop in the corner of the insert during the fourth pass. Figure 6.5 shows typical corner radius and depth of cut notches on the front, side, and bottom of an insert. A comparison of the corner radius notch from the bottom of the insert for the eighth pass of the second and third tests is shown in Figure 6.6. The notch is on the right-hand side of insert. There is a noticeable difference between these two tests. This notch caused additional friction between the insert and the workpiece as well as more ploughing due to a blunt cutting edge. This notch was not detected by the tool-setting touch probe because it was not on the bottom of the insert and due to the geometry of the cut, insert, and stylus it was not feasible to measure the change in radius.

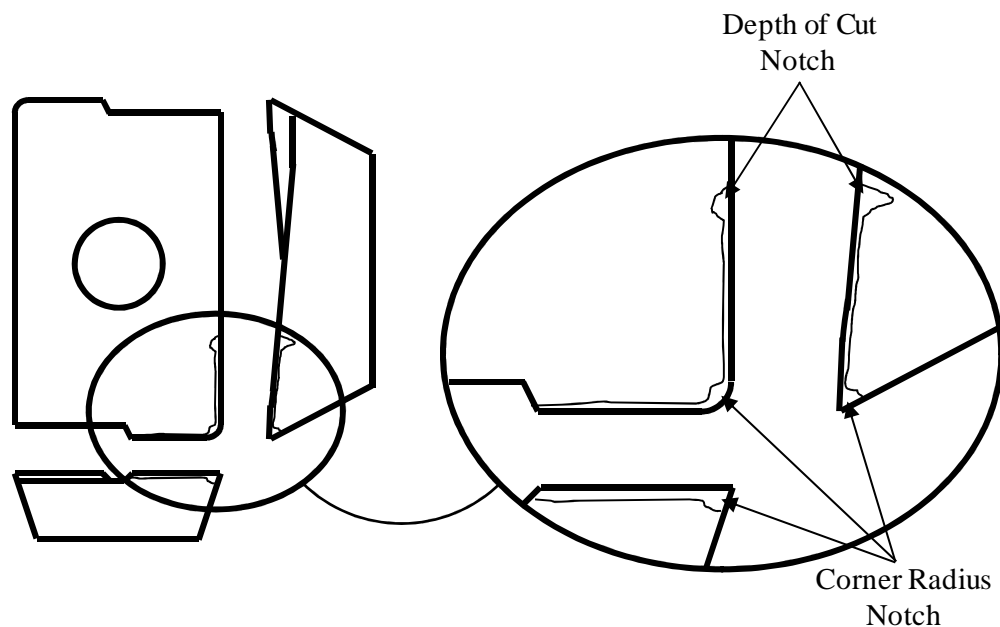


Figure 6.5: Corner radius and depth of cut notches.



Figure 6.6: Insert comparison from the eighth pass of the second and third test.

The average measured tangential cutting forces and corresponding 95% and 98% confidence intervals are shown in Figure 6.7 with model predictions for each test. The confidence intervals represent the expected range of 95% or 98% of the experimental results. Three test replications were completed; therefore, the confidence intervals are determined from the t -distribution with two degrees of freedom. The data in the figure show that as the tests progress, the confidence intervals widen. This occurs because tool wear is stochastic and is dependent on the previous state; therefore, as the tool usage increases, there is more variance in its performance. A similar variance is not observed in the microscope measurements of the tool's flank wear. The tangential cutting force model estimates for the first pass of each test are not within the confidence intervals of the measurements, indicating that, with 98% certainty, the model does not estimate the tangential cutting forces of the first pass. The model estimates for the first pass are low because the edge component of the force model is neglected and the wear is initially zero. Therefore, the model considers the initial cutting forces for the first pass to be only a function of the chip area component. After the first pass, tool wear is significant and the model estimates are all within the 98% confidence interval. Also, most of the model estimates are within the 95% confidence interval. Therefore, after the model initializes, most of the estimates are within the range of 95% of the measurements and the model is statistically significant.

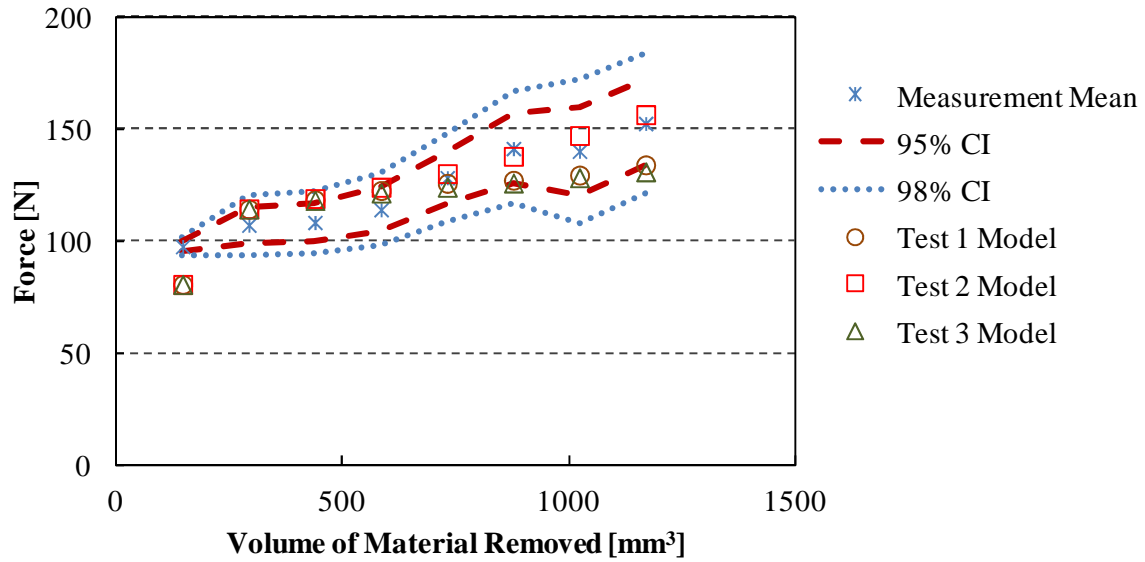


Figure 6.7: Statistical analysis of tangential cutting forces.

A similar analysis was performed on the cutting forces in the normal direction. This data is shown in Figure 6.8. The confidence intervals for the normal cutting force diverge rapidly after the fourth pass. The difference between the upper and lower bounds of the 98% confidence interval is 5 N for the first pass and 12 N for the fourth pass. This indicates good repeatability in the process and experimental data for the initial passes. A notch developed on the corner radius of the inserts during the fourth pass of each test. The development of the notch correlates with the divergence of the confidence intervals. The confidence intervals are based on a sample size of three. As discussed, the cutting forces for the third test deviated from those measured during tests one and two. More test replications are necessary to determine, with a greater statistical certainty, if the confidence intervals actually diverge in this manner or if the third test is an outlier. In addition to more experimentation, additional microscope images of the front and side of the insert must be done to provide the data necessary to understand the extents of the effect of the notch on the cutting operation. These are topics for future research.

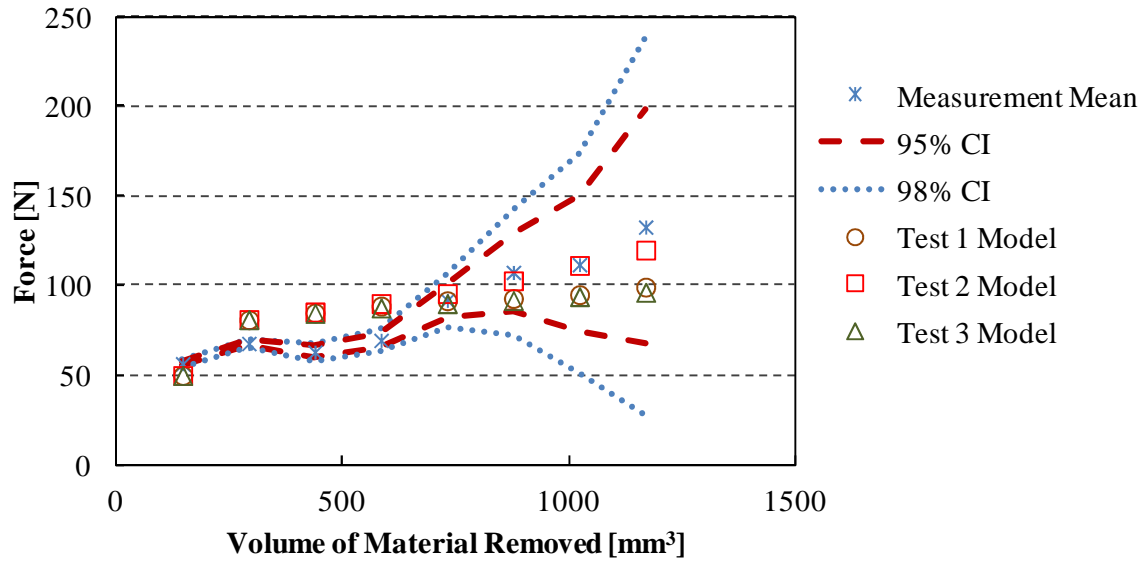


Figure 6.8: Statistical analysis of normal cutting forces.

If tool wear is neglected, the modeled forces remain constant and significant errors occur in the latter estimations. This is shown in Figure 6.9. The percent difference after the eighth pass is 54% and 44% for the normal and tangential cutting forces, respectively, in test 1 and 62% and 47% in test 2. The new force model improves the cutting force estimates by a minimum of 37%.

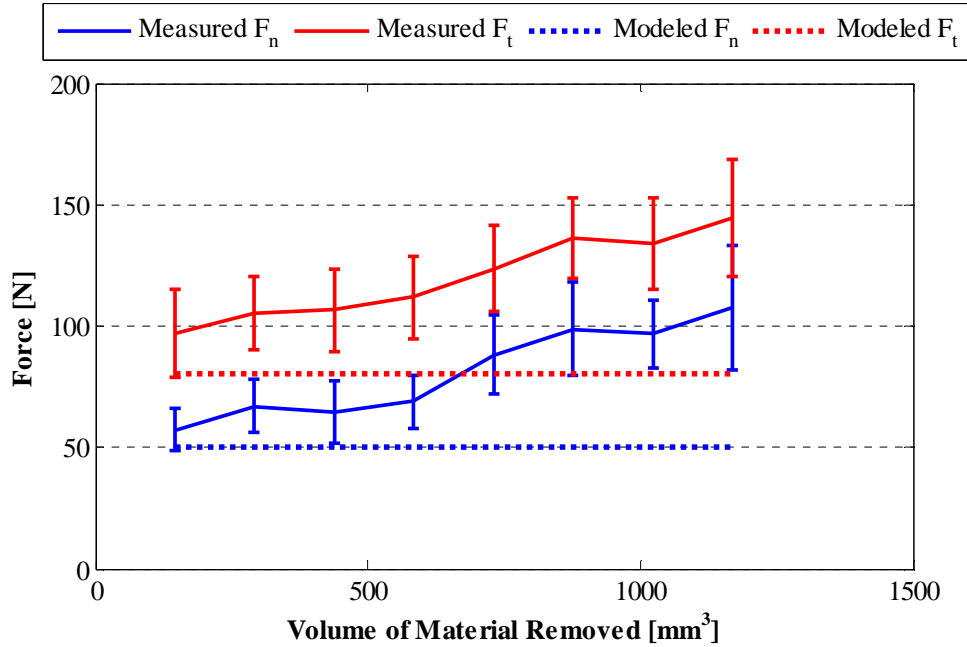


Figure 6.9: Comparison of model without tool wear compensation.

In order to demonstrate the model's ability to predict the cutting forces on a micro level, at the individual tooth passes, the model forces are compared to the measured forces for three complete tool rotations in the first, fourth, and seventh pass of the first test. These comparisons are shown in Figure 6.10, Figure 6.11, and Figure 6.12 for the first, fourth, and seventh pass, respectively. The data displayed are from the point in each pass when approximately 60% of the material has been removed. The time displayed on the x-axis is the total accumulated machining time for the entire test. As discussed in the background, machining time, distance, and volume of material removed are all directly proportional to each other. The x- and y-force components are shown in the figures below for consistency with force plots shown in the previous chapter. The model forces shown in Figure 6.11 for the fourth pass deviate from the measured forces by less

than 10% even though the average model force was shown to overestimate the measured forces by ~30% in Figure 6.2. This is because the data shown in Figure 6.11 are closer to the end of the fourth pass. The data which would show greater errors near the end of the third pass or the beginning of the fourth pass. As expected, based on the average force data, the model estimates the experimental data within ~10% for the seventh pass. The same data for the other two tests are shown in Appendix B with similar results.

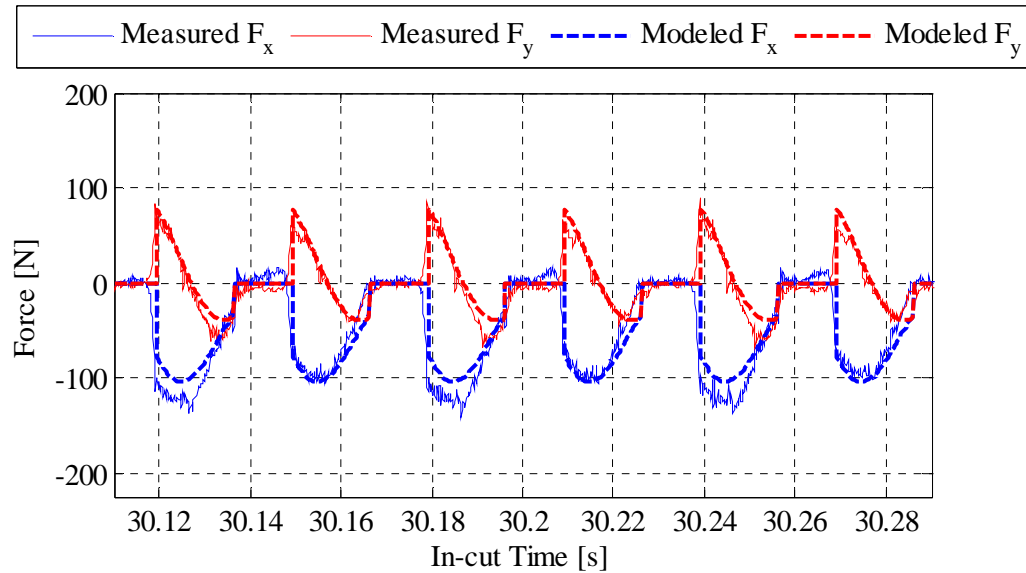


Figure 6.10: Modeled and measured x- and y-direction cutting forces for three tool rotations in the first pass of the first test.

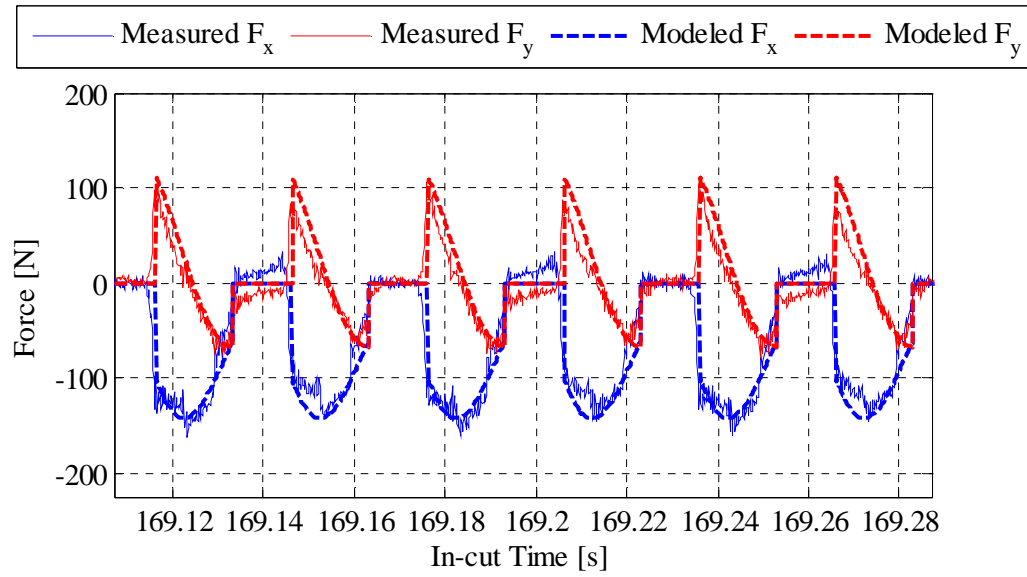


Figure 6.11: Modeled and measured x- and y-direction cutting forces for three tool rotations in the fourth pass of the first test.

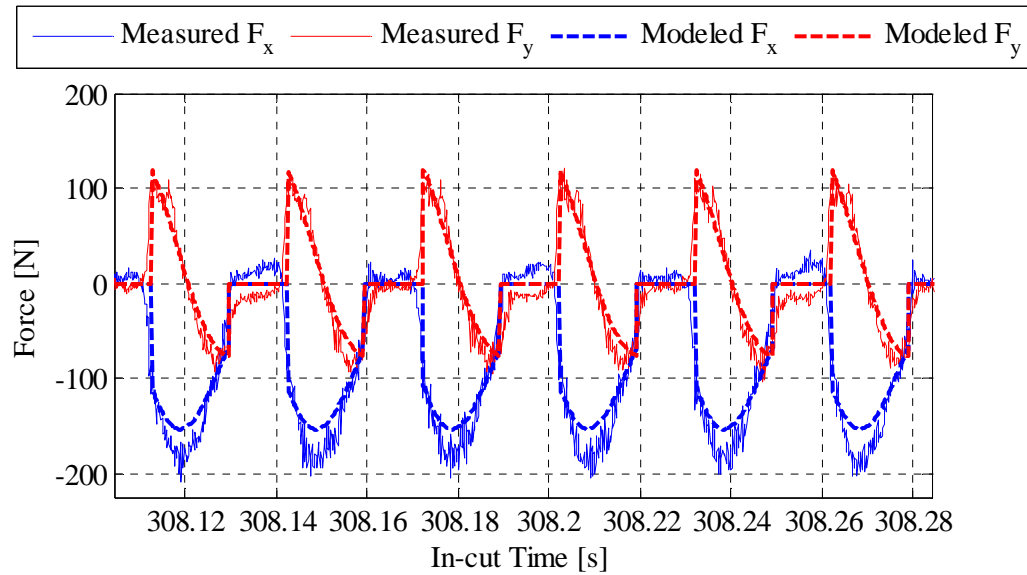


Figure 6.12: Modeled and measured x- and y-direction cutting forces for three tool rotations in the seventh pass of the first test.

Concluding Remarks

The wear estimations, from the methodology developed in the Tool Wear Estimation and Adaptive Tool Wear Estimation chapters, were applied to the new cutting force model, developed in the Force Model Development chapter. This approach was described in this chapter and is shown in the flow chart in Figure 6.13. The results were compared to the measured force data. The average modeled forces from the new model were within 8% of the average measured forces of the last half of tests 1 and 2. The deviation was as much as 62% with the uncompensated model. The average modeled forces do not reflect a rapid increase in the normal cutting force in the last passes of the third test. However, the estimation from the methodology and model presented in this research was 30% closer to the measured forces than the estimate from a force model that does not compensate for tool wear.

The rapid increase in the normal cutting force was concluded to be because of a notch developing in the corner of the insert. The notch is not detectable by the probe and therefore the wear estimations did not reflect it. As mentioned in the Adaptive Tool Wear Estimation chapter, adding a power monitor to this methodology can mitigate this problem. The power monitor is not able to give any indication of the geometric changes of the tool but it would be able to detect a disturbance like the notch. The power monitor would also not reflect the extent to which the normal cutting forces are changing because the spindle power is proportional to the torque required and the torque is a function of the tangential cutting force. The Kalman filter provides a logical platform for this type of sensor fusion because the vectors and matrices in the measurement equation are expandable to any number of measurement devices, so far as the measurements are correlated with the states being estimated. The generalized equations for this implementation are discussed in the Adaptive Tool Wear Estimation chapter.

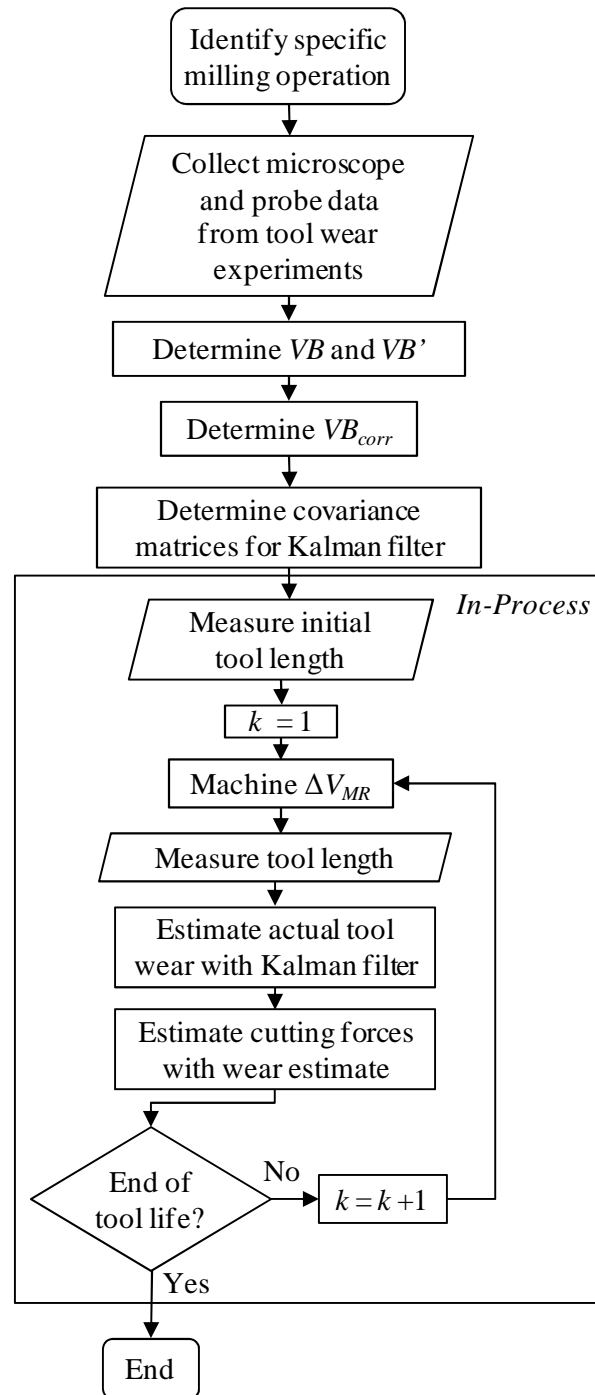


Figure 6.13: Flow chart for implementing the methodology presented.

CHAPTER SEVEN

SUMMARY AND CONCLUSIONS

This research has methodically approached determining a new cutting force model for extremely difficult to machine materials, such as γ' -strengthened nickel-based superalloys. Due to severe tool wear exhibited when machining these materials, the cutting regime is never stable and typical cutting force models are no longer valid. This research introduced new terms, related to the effects of the tool wear, in the force equations. Correlations were made between the physical changes in the geometry of the tool and the size of the wear land. These physical changes were then measured with a tool-setting touch probe. An empirical tool wear model was developed and used in correlation with the touch probe measurements in a Kalman filter to improve the wear estimate as well as make it adaptive. An updated cutting force model which incorporated the physical changes to the tool as it wore was derived. Finally, the improvements to the model were shown to be valid by generating the estimations for real experimental data and then performing a comparison.

With knowledge of the specific cutting coefficients, a reasonable starting estimate of tool wear parameters (VB_0 and VB'), and a touch probe for measuring the tool's change in length, the wear was estimated, using a Kalman filter, within 8 μm of the actual wear and the wear estimate was used to estimate the cutting forces within 8% of the measured forces. The specific cutting coefficients and wear parameters were empirically determined and therefore dependent on the specific test conditions. Therefore, in order to make the model more robust, additional research should be conducted in regards to establishing a knowledgebase for these coefficients when machining under various conditions within γ' -strengthened nickel-based superalloys and to the determination of these coefficients.

Contributions

The contributions of this research are the:

- experimentation and adapted models for milling cast γ' -strengthened nickel-based superalloys,
- use of on-machine touch probes for estimating tool wear,
- use of Kalman filter for adaptive estimation of tool wear using touch probes, and
- improved force model addressing physical changes in the tool.

The primary contribution is the improved force model which provides an improved force estimate for milling cast γ' -strengthened nickel-based superalloys. The use of touch probes and the Kalman filter allows this methodology to be applied in-process. The extremely low machinability of the γ' -strengthened nickel-based superalloys puts them in a class where no milling research has ever been done. Therefore, the experimentation and adapted models are significant.

The use of on-machine touch probes to estimate tool wear is novel. There have been research and industrial approaches to monitoring and estimating tool wear on-machine; however, touch probes have not been used for this purpose. The benefits of touch probes are low cost, ease of implementation, current availability on many production machine tools, and the insight to physical changes in the tool. The use of the Kalman filter to provide an adaptive estimation of an end-mill's tool wear via touch probes is also unique. The Kalman filter provides robust tool wear estimation utilizing on-machine measurements and associated uncertainty to determine an optimal state estimate. The improved force model is unique with regard to the method of accounting for tool wear through the changes to the tool's geometry. This provides a better fundamental physical understanding of the effects of tool wear on cutting forces.

Impact of Research

Wear and forces are both critical in terms of subsurface damage generation. Subsurface damage is directly linked to component failures in parts made of superalloys. Thus, it is a primary quality concern for the final manufactured products. Accurate subsurface damage models will allow manufacturing process development times to decrease and first part acceptance to increase. These aspects improve the manufacturer's bottom line by decreasing manufacturing costs and warranty costs. The improved part quality benefits the end user because there would be less missed defects from the factory and fewer failures in operation leading to, in regards to gas turbines, more power generated for the end user. The lower bottom line for the manufacturer results in more capital for expanding and job creation. From a broader sense, government sponsored initiatives are underway to group, characterize, and relate materials and their properties for the advancement of future material development. The γ' -strengthened nickel-based superalloys are an advanced type of material and this research provides processing characteristics of these materials which could be included as another criterion when developing future alloys.

In regards to the immediate practicality of this work, accurately estimating tool wear is a problem that plagues many machine shops. Due to the inability to accurately estimate the wear on a cutting tool, tool life limits are commonly set at conservative levels and tools are changed regardless of actual useful life. Therefore, cutting tools are not being used as efficiently as possible. This research can have an immediate and direct impact to the way machining is done today. The methodology for estimating tool wear can be implemented using standard equipment on most current machine tools. The adaptive estimations allow manufacturing personnel to utilize tooling longer and efficiently. The plot in Figure 3.9 illustrates the differences in wear rates between the cast γ' -strengthened nickel-based superalloys in this research and AISI 4340 Steel. This plot illustrates that similar wear can be observed while machining other materials but it will

occur over a much longer time (or after much more material has been removed) In addition to these immediate benefits, the wear estimation can be used to further refine other models, such as the force model in this research and ultimately the subsurface damage model.

Bounds of Applicability

The general forms of the models and the methodology of this research can be applied to the milling of any material. However, the specific model coefficients are empirical and are only applicable to the material, tools, and cutting parameter combinations presented in this research. The coefficients which need to be determined for other machining conditions are listed below:

- probe measurement to flank wear correlation factor, VB_{corr} ,
- tool wear model parameters, VB_0 and VB' ,
- Kalman filter covariance matrices, **Q**, **R**, and **P**, and
- specific cutting force coefficients, $k_{_}$.

The flank wear correlation factor, VB_{corr} , is dependent on the type of measurement, measurement location, and tool geometry. The logic for determining the factor will be similar for a different type of touch measurement and/or cutter geometry but the specific relationships will vary. The wear model parameters are dependent on cutter material, cutter geometry, workpiece material, and cutting parameters. Therefore, experimentation is required for the determination of these parameters whenever one of these components changes. The Kalman filter process covariance, **Q**, has the same dependencies as the tool wear model parameters. The measurement covariance, **R**, depends on the accuracy of the measurement system. The error covariance, **P**, depends on both **Q** and **R**. The specific cutting coefficients depend significantly on workpiece material and cutter geometry but they are also dependent on cutting parameters, as shown in Figure 5.14.

The tool wear estimation assumes that flank wear is the dominant wear type and that the tool is wearing consistently on the radial and bottom edge. As discussed in the Validation of the New Model Approach chapter, a developing notch on the tool's edge has a significant influence on the cutting force output. Furthermore, the measurements made on the bottom edge are not able to detect the notch as it occurs above the cutting tool's bottom edge. Therefore, this tool wear estimation approach requires modification when the dominant wear type is not flank wear. It is assumed that power monitoring will detect the development of the alternative wear types. The power monitor will not be able to discern the specific wear type that is developing as it does not measure the physical aspects of the tool; however, it will be able to detect a disturbance in the process which will indicate the development of a second wear type.

The cutting force estimation assumes that the radial and tangential cutting forces are influenced similarly by tool wear. The statistical analysis in the Validation of the New Model Approach chapter indicates that the corner radius notch has a more significant effect on the normal cutting forces than the tangential cutting forces. The ISO tool wear specification describes the notch wear, as seen in this research, as localized flank wear [29]. Assuming that the notch's VB is the maximum VB along the cutting edge, then estimating VB_{max} and substituting it for the VB term in the updated force model for normal cutting forces will reflect the effect of the notch on the normal force component.

Recommendations

This research is the foundation for in-process models which will eventually lead to the in-process estimation of subsurface damage from milling. Figure 7.1 shows the components that are necessary for achieving the in-process subsurface damage estimation. The solid lines indicate the components that were addressed in this research. The dashed lines indicate the components

that are recommended for future research. The tool wear estimation from power monitoring will provide the ability to detect wear types, other than flank wear. The analytical wear model parameter determination will reduce the amount of testing and data necessary to implement this methodology in multiple operations. Cutting temperatures are necessary for determining flow stresses in the material during the cutting action and will be used in conjunction with the cutting forces to estimate subsurface damage.

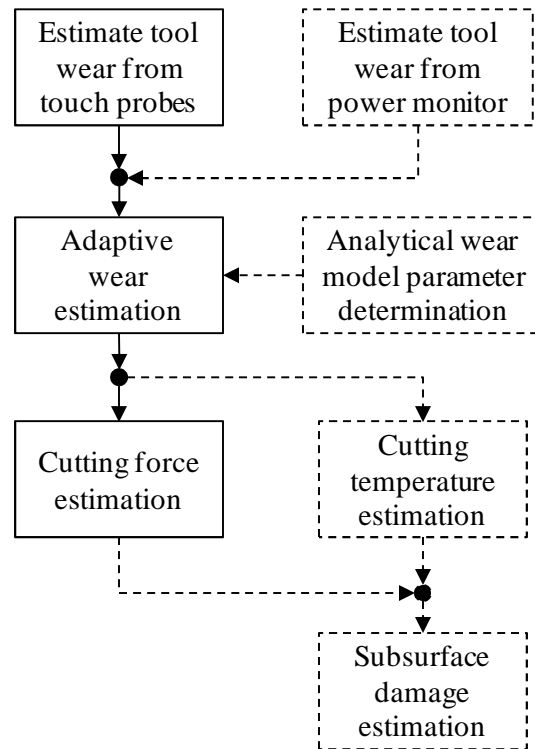


Figure 7.1: Necessary inputs for in-process estimations of subsurface damage.

APPENDICES

Appendix A

Force Estimation Using Touch Probes

The radial cutting forces can be estimated through the coordination of the tool-setting touch probe and spindle touch probe measurements under certain circumstances. It must be possible to assume that the cutting tool is the least stiff component within the cutting system. The spindle support, spindle-tool connection, and bearings within the spindle must form a structure that can be assumed to be significantly stiffer than the cutting tool itself and the workpiece and fixture must be more rigid than the cutting tool. The cutting tool should be assumed to be a cantilevered beam with constant circular cross-section.

Tool Deflection

The contact force between the probe's stylus and the tool is nearly zero. Therefore, tool deflection should not affect the measurements made with the tool set station. However, there are significant forces on the tool during the milling process. Therefore, tool deflection will affect the dimensions of the surface left on the workpiece and the measurements made with the spindle probe. When the tool deflects, the insert that is engaged in the material will make a deeper cut than expected. This is depicted in the sketch in Figure A.1. The example finite element analysis data, in Figure A.2, reinforce this fact. This finite element data were generated in Abaqus and it simulates a round bar that is fixed at the top and is being deflected by a force applied laterally at the bottom of the bar. This FEA example is a simplified case but gives insight into how the tool may deflect under load. Average force data was taken from the machining trials run on the machine and input into the simulation.

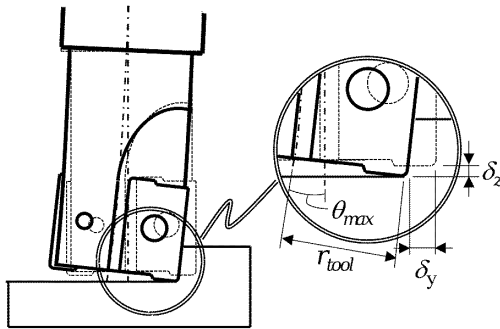


Figure A.1: Sketch of tool deflection while cutting.

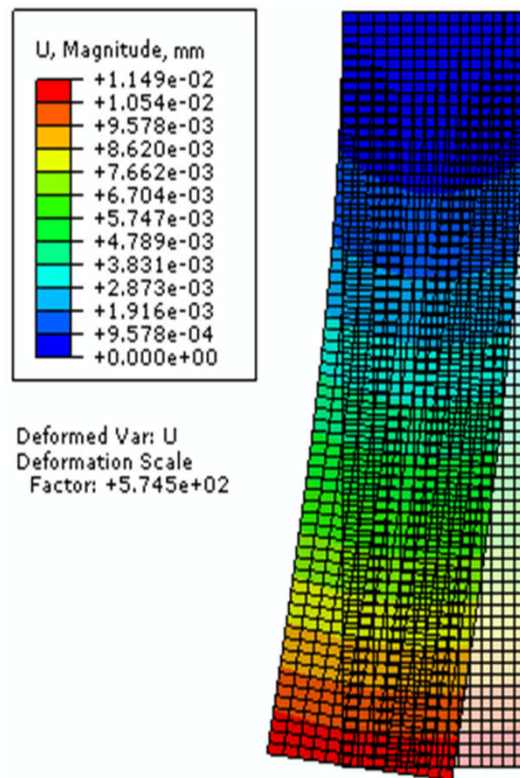


Figure A.2: Example results from a finite element simulation.

The standard beam deflection equations found in any mechanics of materials textbook show that, for a cantilevered beam of length L with a load at the free end (P_y) the maximum deflection at the free end ($\delta_{y,\max}$) is represented by equation (A.1),

$$\delta_{y,\max} = \frac{P_y L^3}{3EI}, \quad (\text{A.1})$$

and the angle at which it is deflected (θ_{\max}) is represented by equation (A.2),

$$\theta_{\max} = \frac{P_y L^2}{2EI}, \quad (\text{A.2})$$

where E and I are the material's Young's Modulus and the bar's area moment of inertia.

It is assumed that the rest of the spindle setup is much stiffer than the tool and that tool experiences the most deflection. Under this assumption only tool properties need to be known. In this experimental setup the tool diameter is 15.875 mm and therefore the area moment of inertia is 3118 mm⁴. The tool stick-out length (L) is 65 mm. The deflection can also be calculated via equation (A.3),

$$\delta_{y,\max} = \frac{P_y}{k_y}, \quad (\text{A.3})$$

by knowing the stiffness in the y-direction (k_y). By equating equations (A.1) and (A.3), it can be determined that the stiffness can be represented by equation (A.4),

$$k_y = \frac{3EI}{L^3}. \quad (\text{A.4})$$

The stiffness in the y-direction was determined experimentally by pushing the bottom corner of the tool against a workpiece which was securely mounted to a force dynamometer. The forces were measured by the dynamometer and the corresponding displacements were recorded from the machine tools coordinate read-out. The stiffness in the y-direction was determined to be 6.4 MN/m. Using the area moment of inertia and stick-out length of just the tool, the

experimental Young's modulus (E) is calculated to be 188 GPa. This is a reasonable value for the steel tool.

By assuming that the z-deflection (δ_z) at the centerline of the tool does not change significantly, a simple relationship between z-deflection at the radius of the tool (r_{tool}) and the applied load can be determined. This assumption was determined to be valid through FEA simulations. A simulation was completed with an input force of 400 N, which exceeds the maximum forces recorded during any of the tool wear tests. The z-deflection at the centerline for this case was 0.15 μm , a value that may be considered negligible and therefore the following derivation is valid.

By combining equation (A.2) and (A.4) the easily determined experimental stiffness value can be used in the angle equation as shown below in equation (A.5),

$$\theta_{\max} = \frac{3}{2} \frac{P_y}{Lk_y} . \quad (\text{A.5})$$

Using trigonometry, equation (A.6),

$$\delta_{z,\text{radius}} = r_{tool} \sin(\theta_{\max}) = r_{tool} \sin\left(\frac{3}{2} \frac{P_y}{Lk_y}\right), \quad (\text{A.6})$$

can be derived. Since, the calculated θ_{\max} is in radians, the sine of this angle should be calculated appropriately.

Since deflection increases with cutting forces and cutting forces increase with tool wear, as the tool wears the tool deflection will become greater, causing the cutting depth to increase. In the same time, the cutting depth decreases due to decrease in the length of the tool. Therefore, the measurement with the spindle probe will be smaller than the measurement with the tool set station. This relationship can be written as shown in equation (A.7),

$$\Delta SP = \Delta L_{TW} - \delta_{z,\text{radius}} . \quad (\text{A.7})$$

where ΔL_{TW} is the tool length measurement made with the tool set station and ΔSP is the change in the depth of cut which is measured with the spindle probe.

Combining equations (3.4) and (A.7) VB can be written as shown in equation (A.8),

$$VB = \left(\frac{1}{\tan(\psi)} - \tan(\lambda_s) \right) \left(\Delta SP + r_{tool} \sin \left(\frac{3}{2} \frac{P_y}{Lk_y} \right) \right). \quad (A.8)$$

Force Estimation

Using the equations derived so far and the change in touch probe measurements the force on the tool could be predicted. Since ΔL_{TW} is the measurement made with the tool set station (ΔTS), equations (A.7) and (A.6) can be combined and solved for the force. This rearranged equation is shown in equation (A.9),

$$P_y = \sin^{-1} \left(\frac{\Delta TS - \Delta SP}{r_{tool}} \right) \left(\frac{2Lk_y}{3} \right). \quad (A.9)$$

Results and Discussion

The force dynamometer recorded force data in the x-, y-, and z-directions. The spindle probe measurements were made along the path that the centerline of the tool traveled as a pass was machined. This correlated to the instance when the cutting edge was aligned with the y-axis (90° cutter rotation). Therefore, the forces pushing on the tool in the radial direction were simply the y-direction forces. From the tooling and cutting parameters, the entry angle for a tooth was resolved and this was correlated to the force data for each pass. With the cutter angle data, a window of force data around 90° were averaged and the error bar plot in Figure A.3 was generated. Figure A.3 also shows the estimation of this force based on equation (A.9). The connected points in Figure A.3 represent the average radial force at 90° of cutter rotation, while

the error bars represent a single standard deviation about the average.

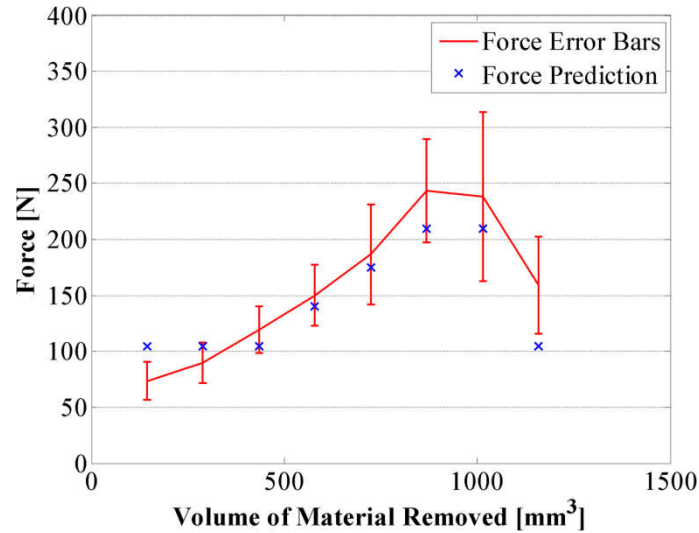


Figure A.3: Error bar plot of y-direction forces with estimations from probe analysis.

It can be seen in Figure A.3 that the estimated force values from probe measurements for each pass except the first and last fall within a single standard deviation of the average force measured with the dynamometer. It is expected that smaller amounts of tool wear will result in inaccurate measurements by the probes due to the resolution of the probe measurements. This will be discussed further in section 0. One of the cutting inserts fractured within the seventh pass. This explains the decrease in average cutting forces and the large standard deviation as well as the decrease in the eighth pass. The failure of the insert caused the corner to chip away in an unpredictable manner. Therefore, the calculation was not able to estimate the forces from the last pass.

Appendix B

Model Results for Each Pass of Tests 1-3

Test 1

The modeling results are compared to the measured data for each pass of the first tool wear test. These results are shown in Figure B.1 through Figure B.8.

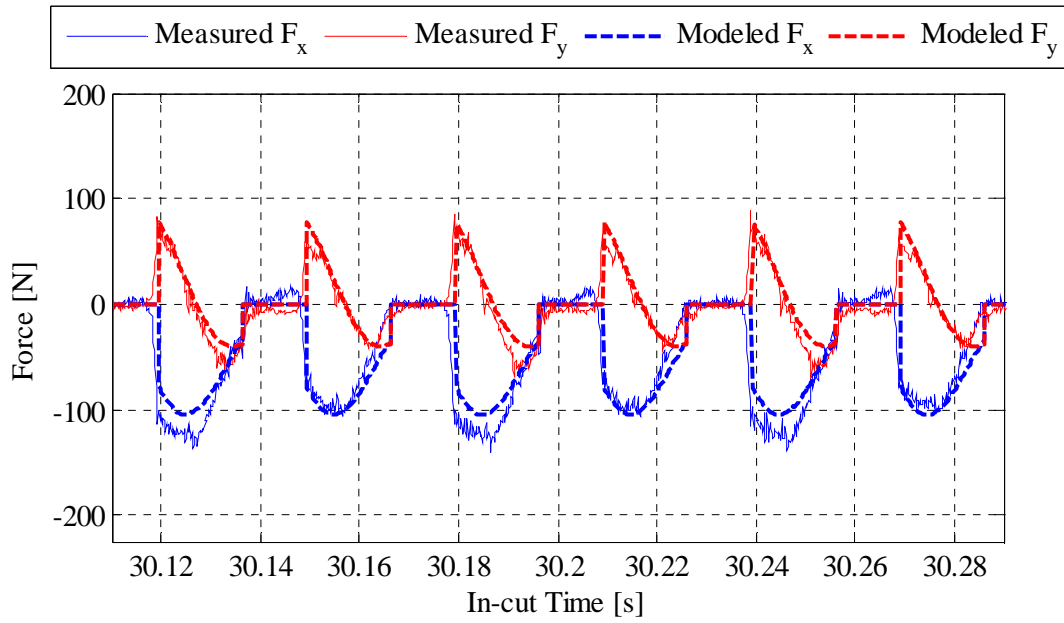


Figure B.1: Modeled forces compared to measured forces for the first pass of test 1.

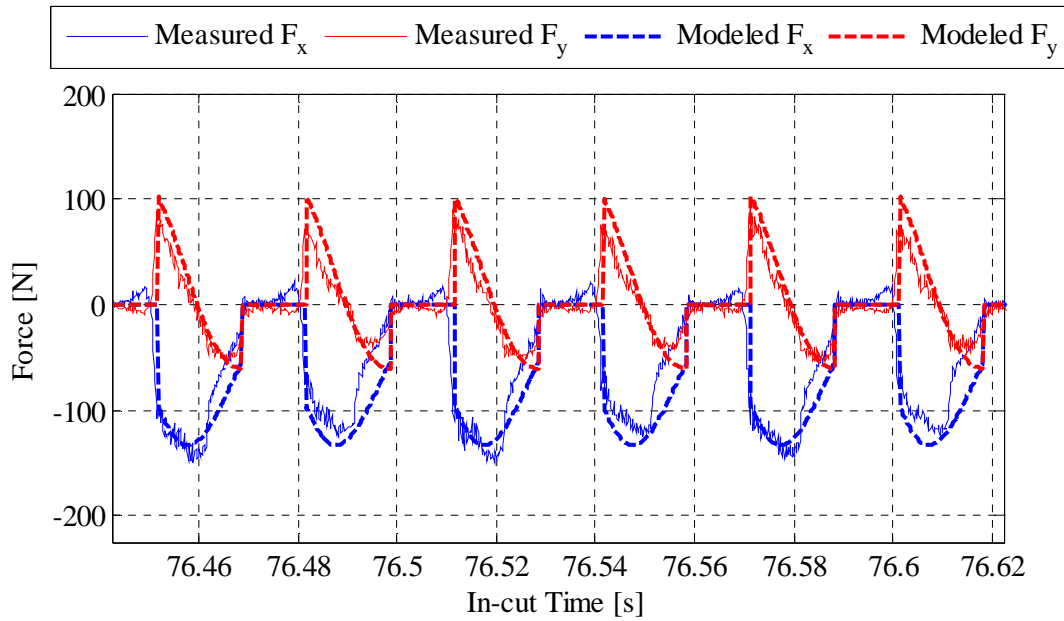


Figure B.2: Modeled forces compared to measured forces for the second pass of test 1.

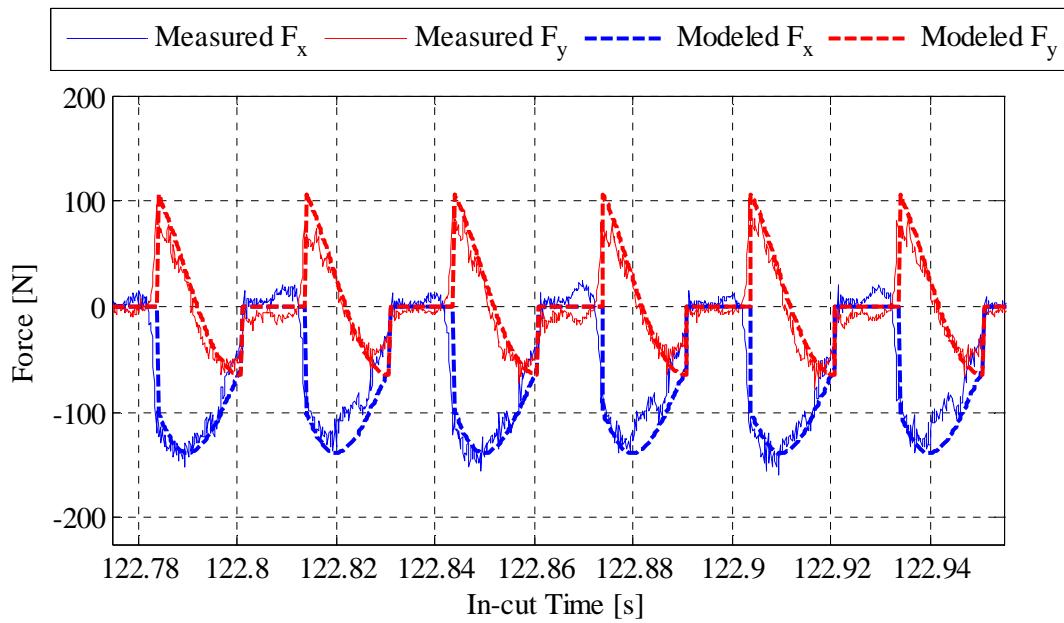


Figure B.3: Modeled forces compared to measured forces for the third pass of test 1.

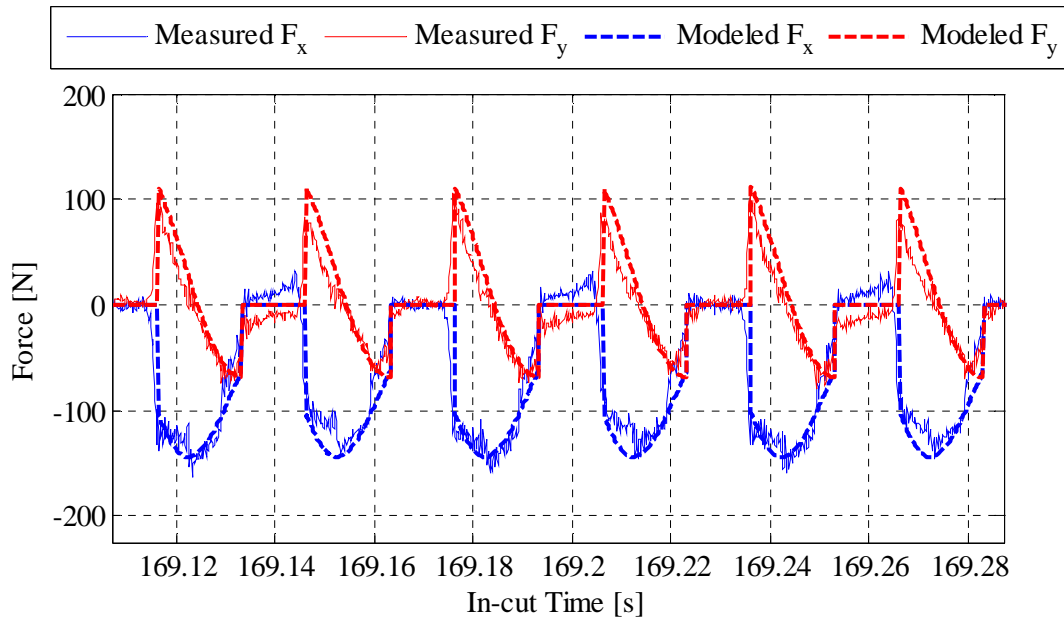


Figure B.4: Modeled forces compared to measured forces for the fourth pass of test 1.

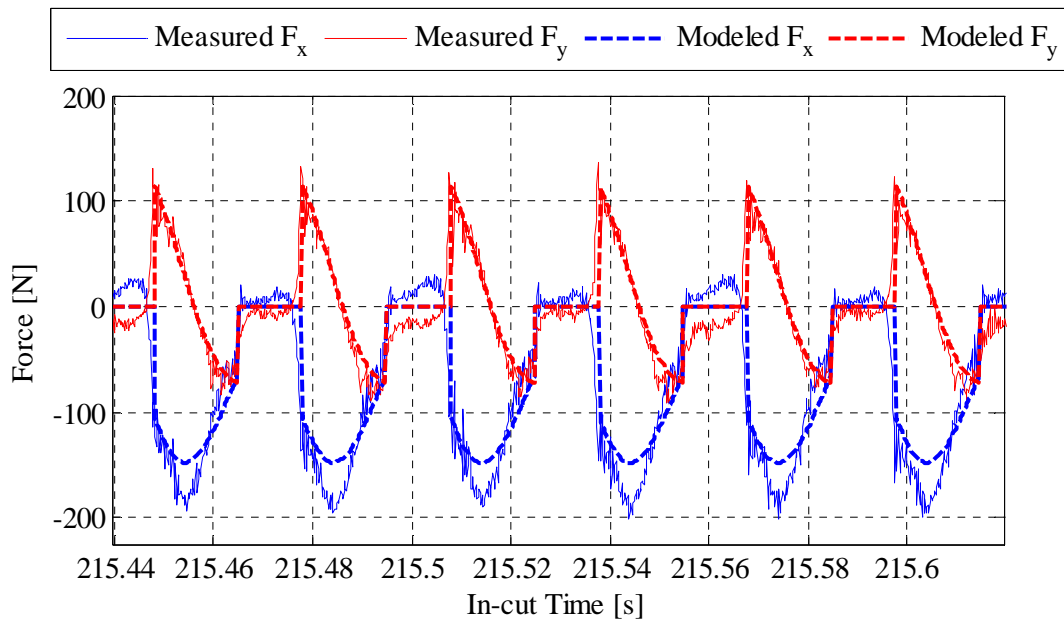


Figure B.5: Modeled forces compared to measured forces for the fifth pass of test 1.

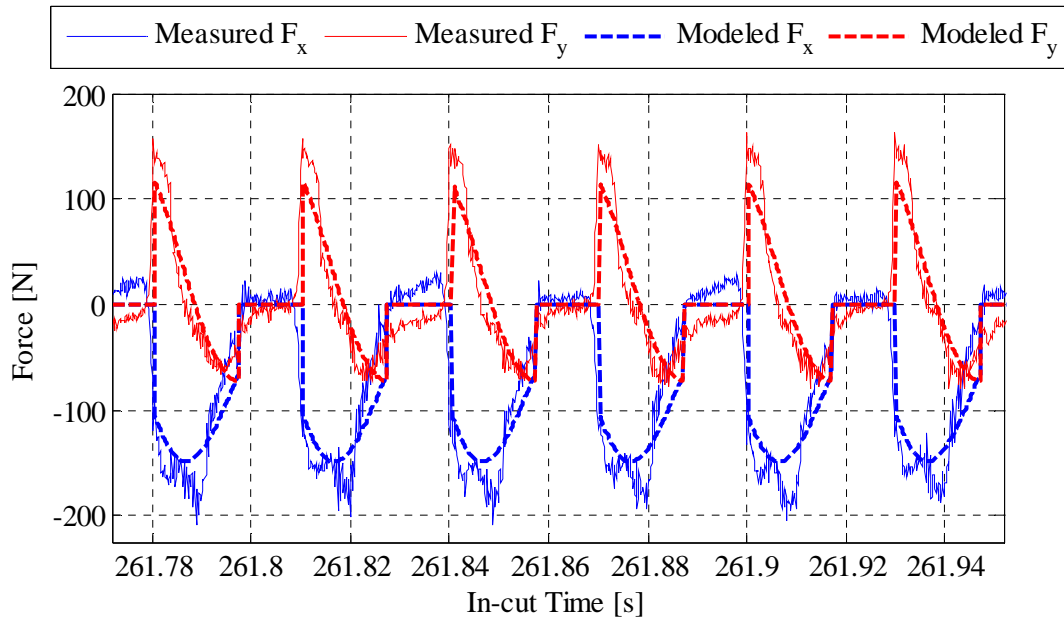


Figure B.6: Modeled forces compared to measured forces for the sixth pass of test 1.

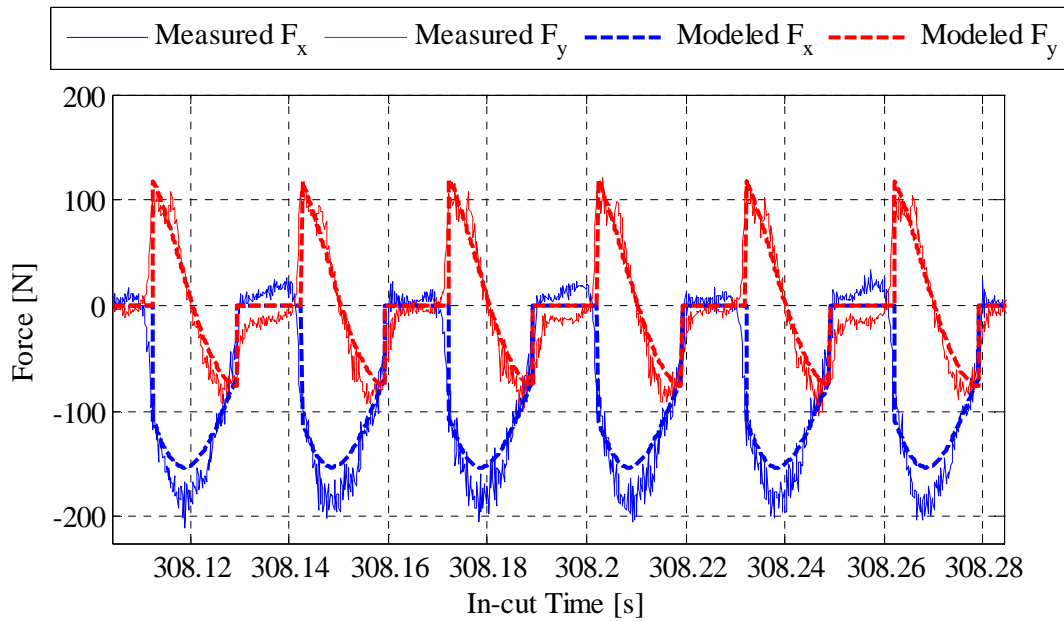


Figure B.7: Modeled forces compared to measured forces for the seventh pass of test 1.

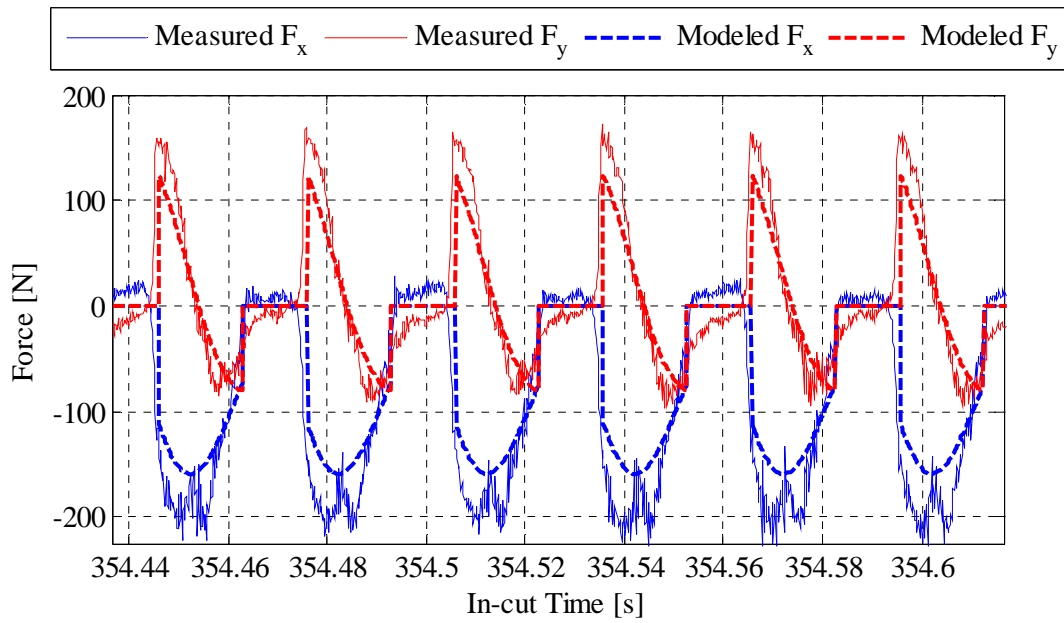


Figure B.8: Modeled forces compared to measured forces for the eighth pass of test 1.

Test 2

The modeling results are compared to the measured data for each pass of the second tool wear test. These results are shown in Figure B.9 through Figure B.16.

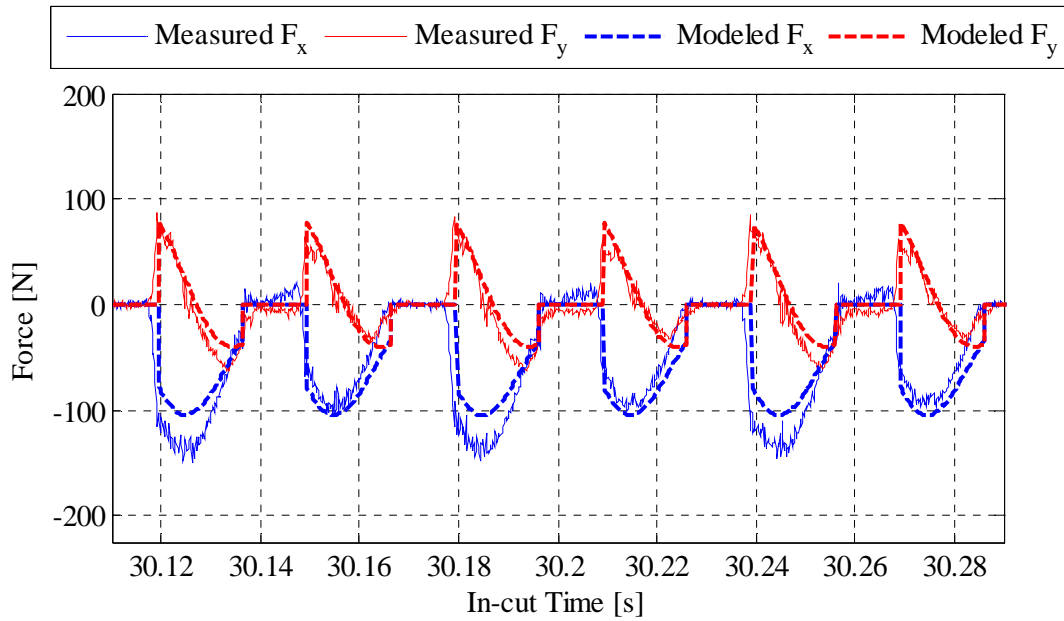


Figure B.9: Modeled forces compared to measured forces for the first pass of test 2.

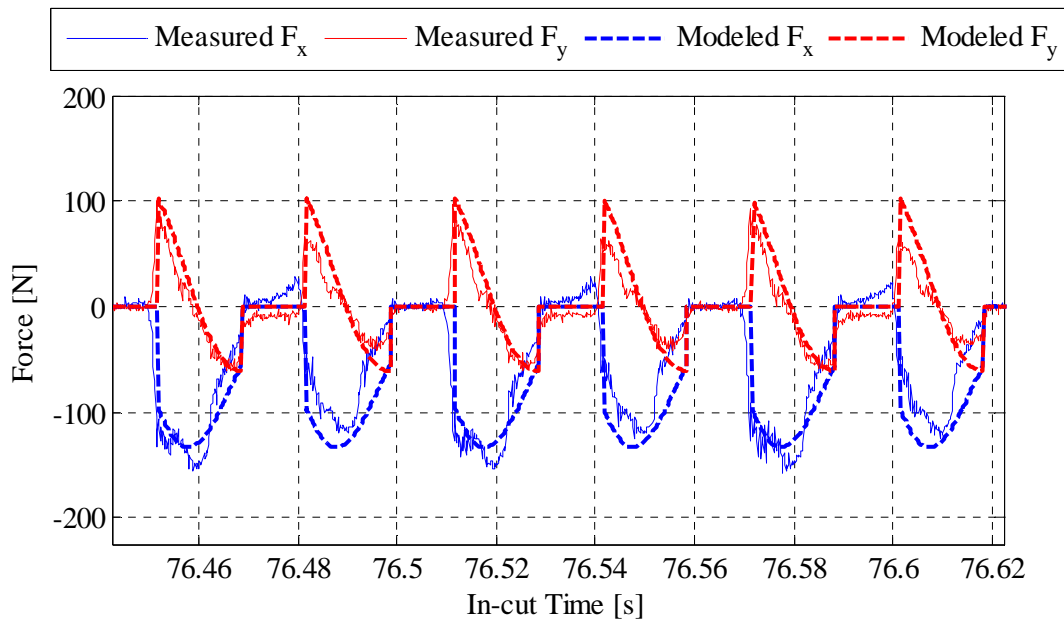


Figure B.10: Modeled forces compared to measured forces for the second pass of test 2.

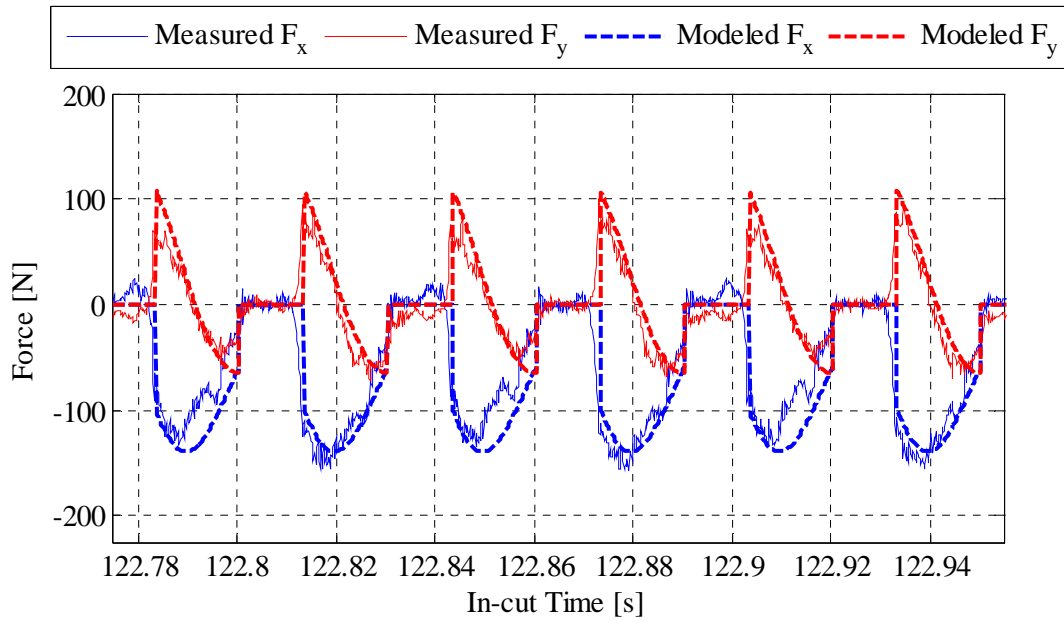


Figure B.11: Modeled forces compared to measured forces for the third pass of test 2.

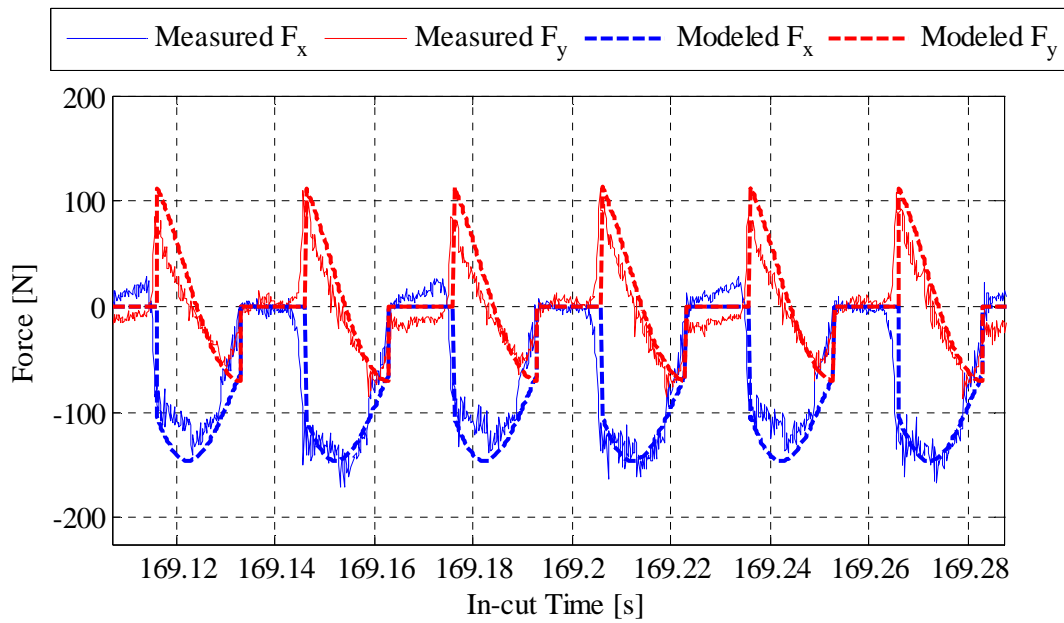


Figure B.12: Modeled forces compared to measured forces for the fourth pass of test 2.

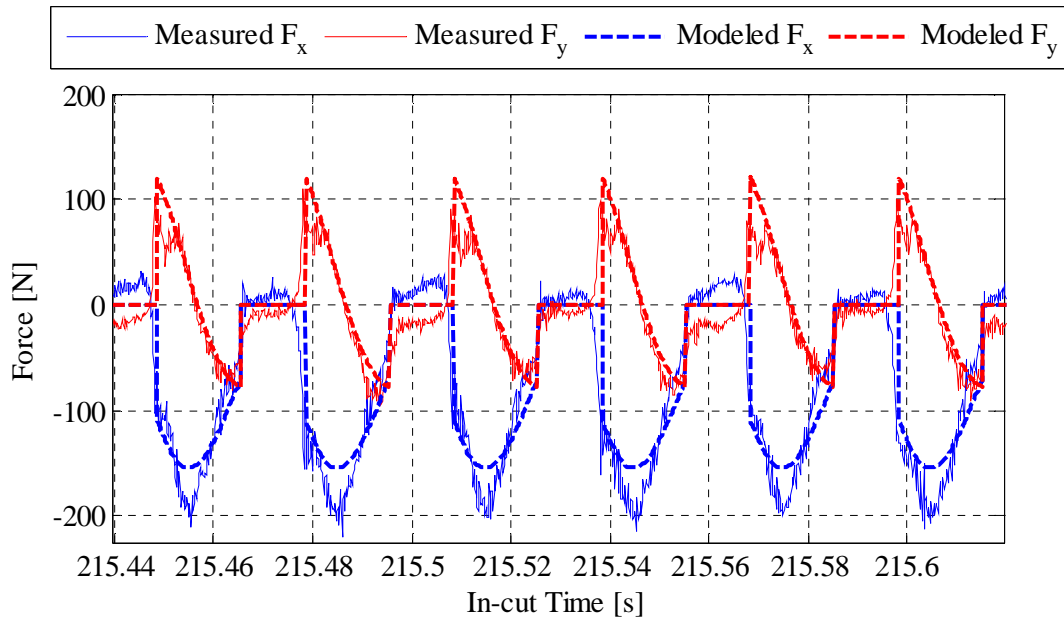


Figure B.13: Modeled forces compared to measured forces for the fifth pass of test 2.

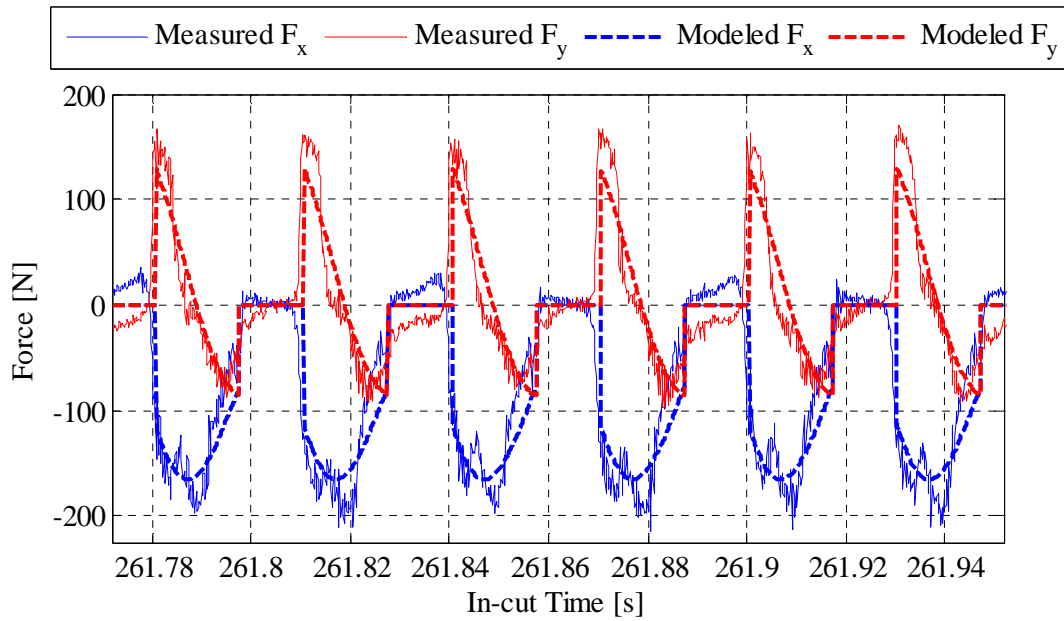


Figure B.14: Modeled forces compared to measured forces for the sixth pass of test 2.

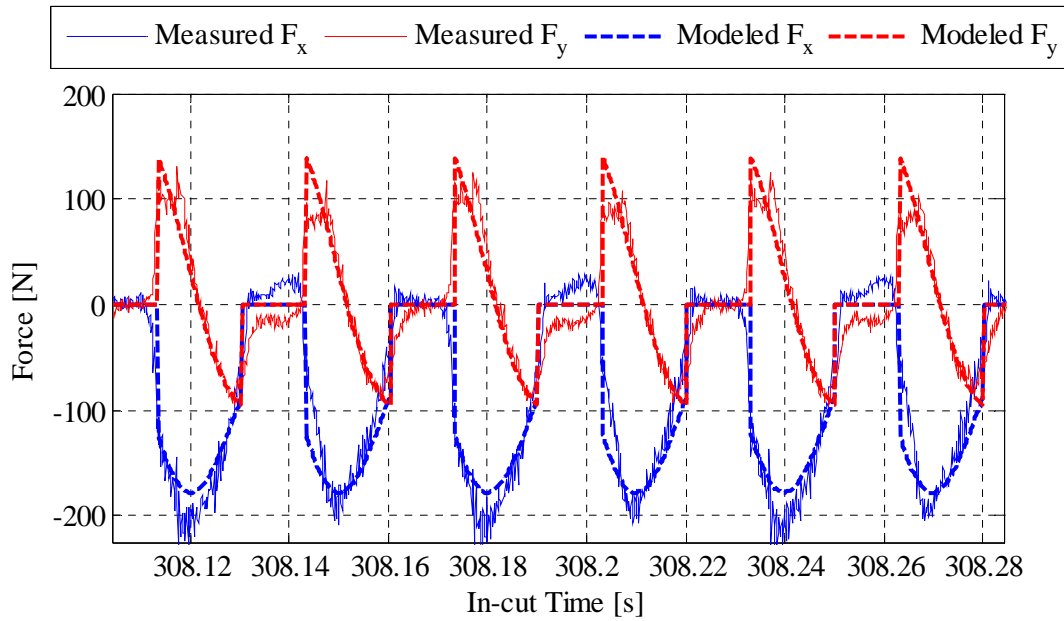


Figure B.15: Modeled forces compared to measured forces for the seventh pass of test 2.

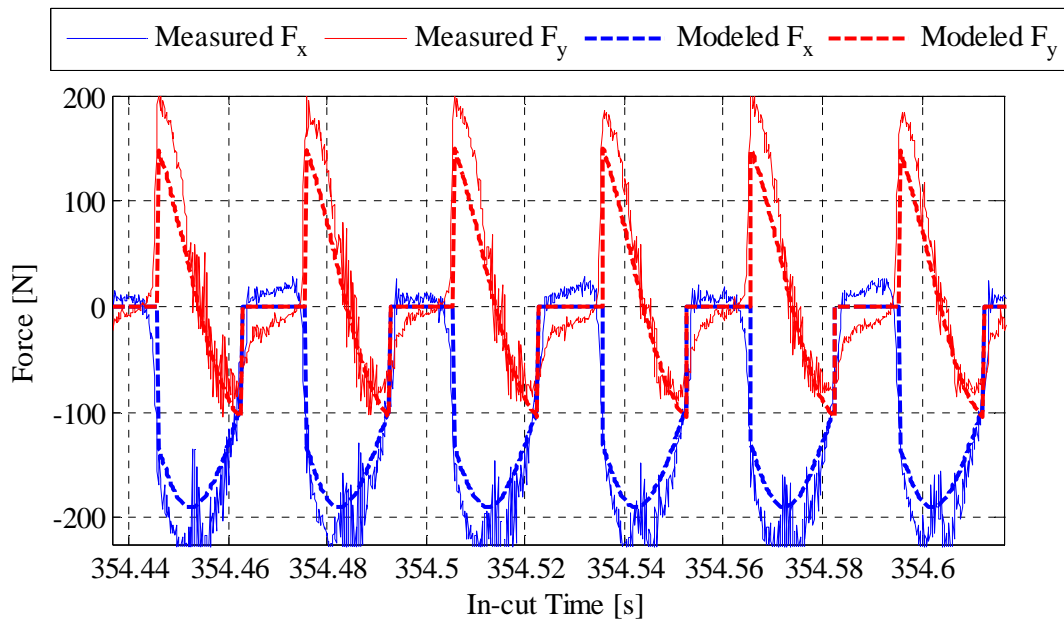


Figure B.16: Modeled forces compared to measured forces for the eighth pass of test 2.

Test 3

The modeling results are compared to the measured data for each pass of the second tool wear test. These results are shown in Figure B.17 through Figure B.24.

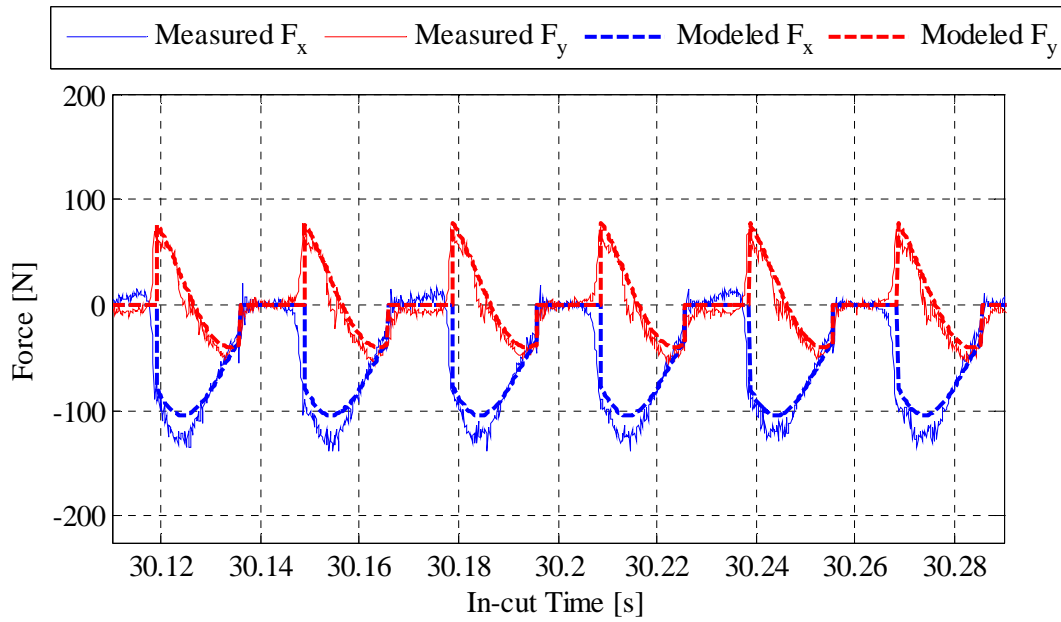


Figure B.17: Modeled forces compared to measured forces for the first pass of test 3.

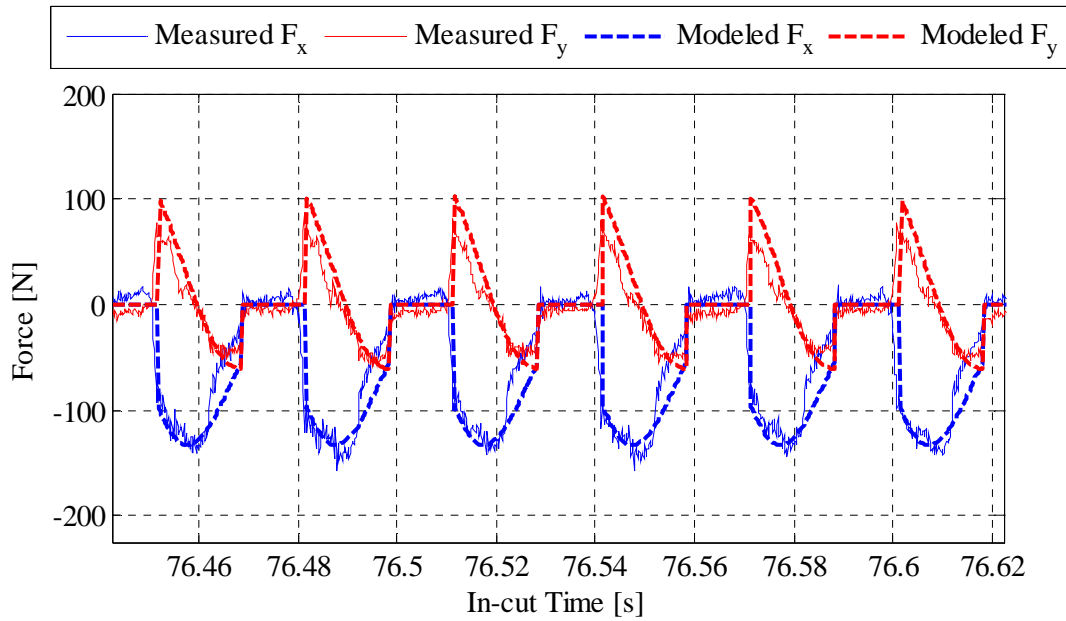


Figure B.18: Modeled forces compared to measured forces for the second pass of test 3.

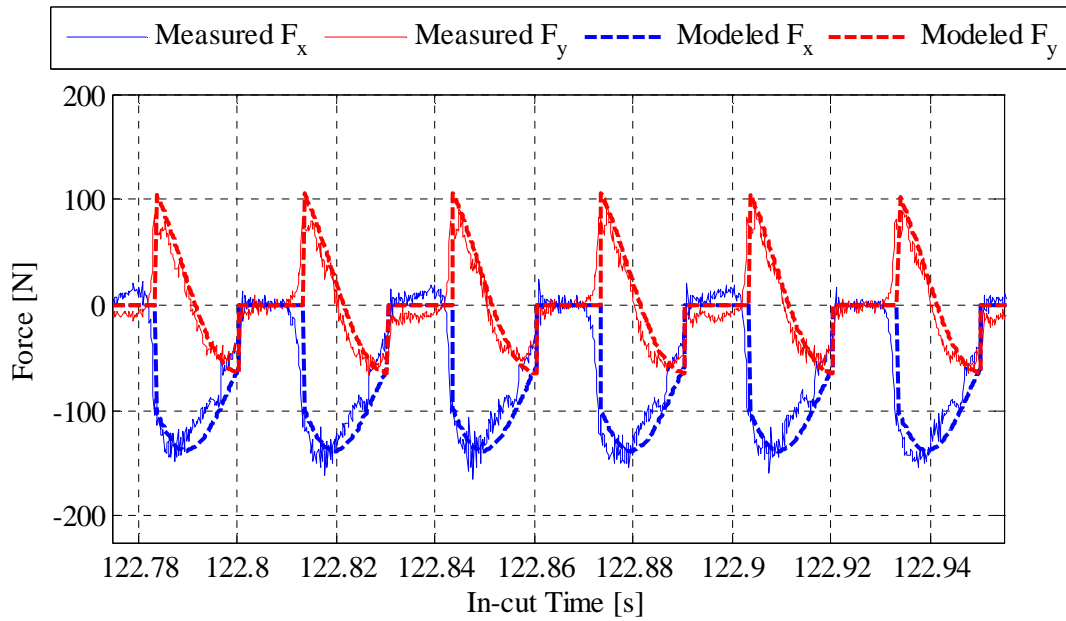


Figure B.19: Modeled forces compared to measured forces for the third pass of test 3.

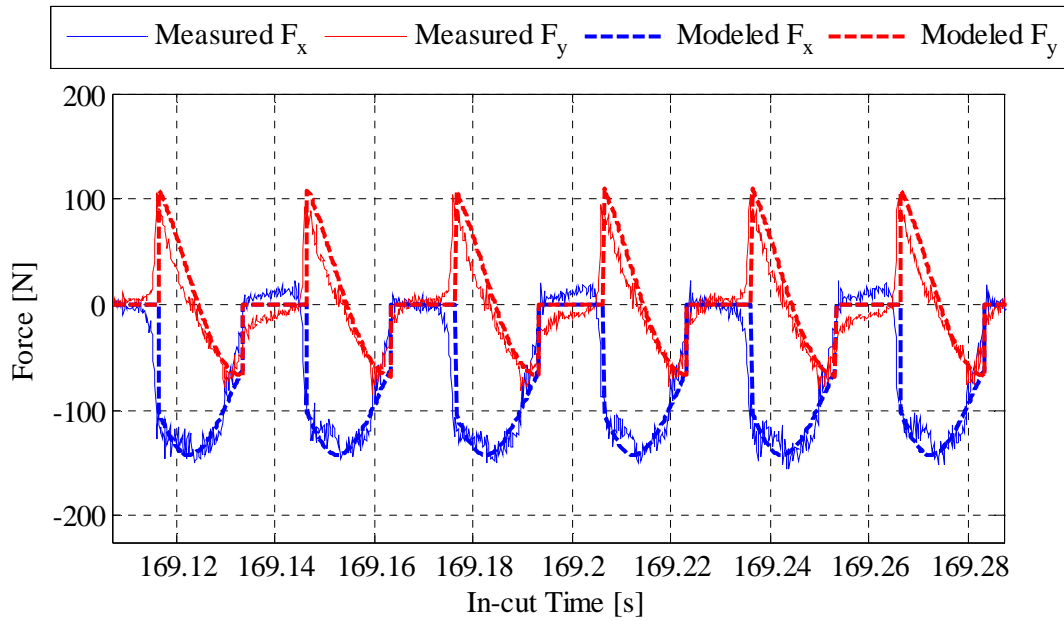


Figure B.20: Modeled forces compared to measured forces for the fourth pass of test 3.

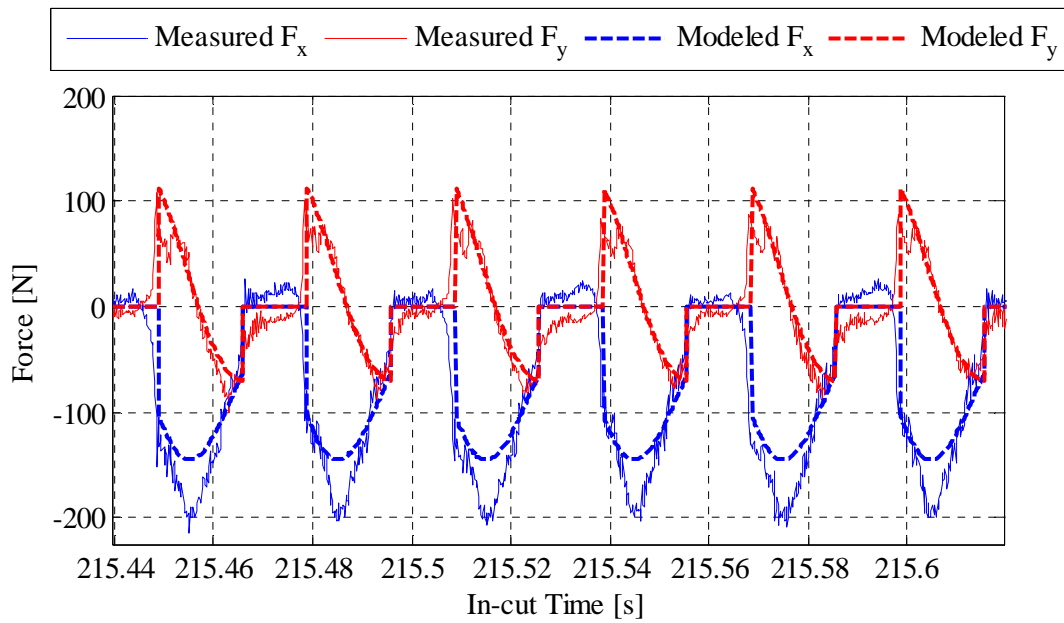


Figure B.21: Modeled forces compared to measured forces for the fifth pass of test 3.

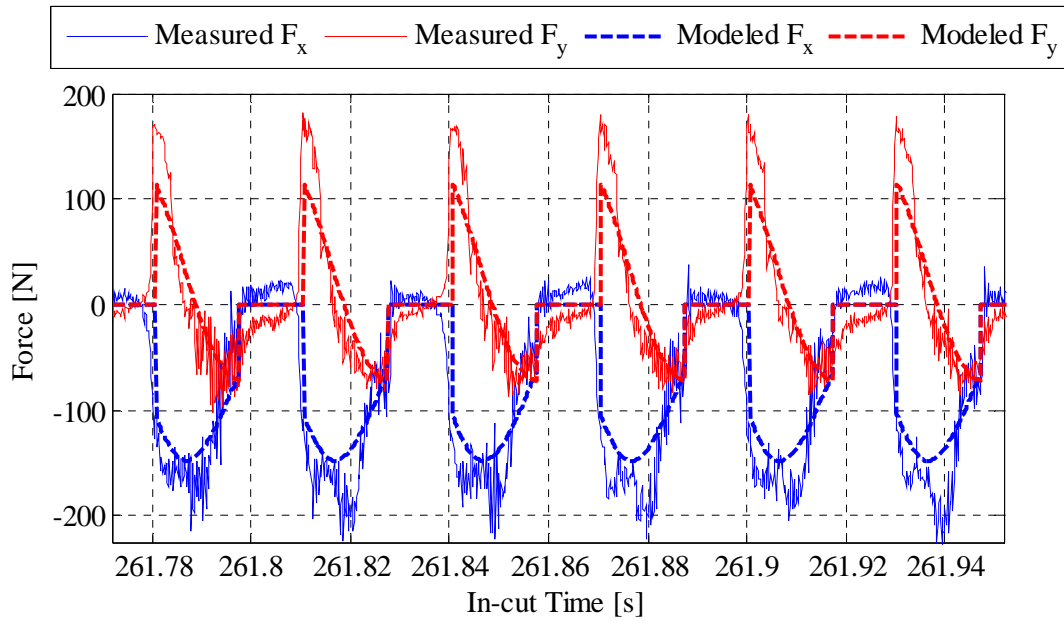


Figure B.22: Modeled forces compared to measured forces for the sixth pass of test 3.

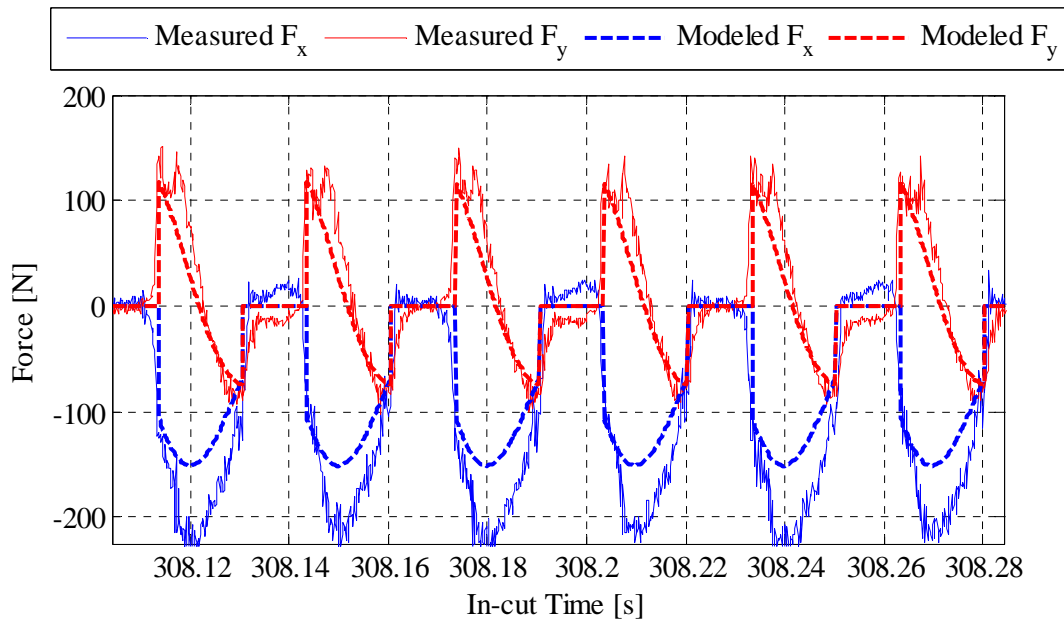


Figure B.23: Modeled forces compared to measured forces for the seventh pass of test 3.

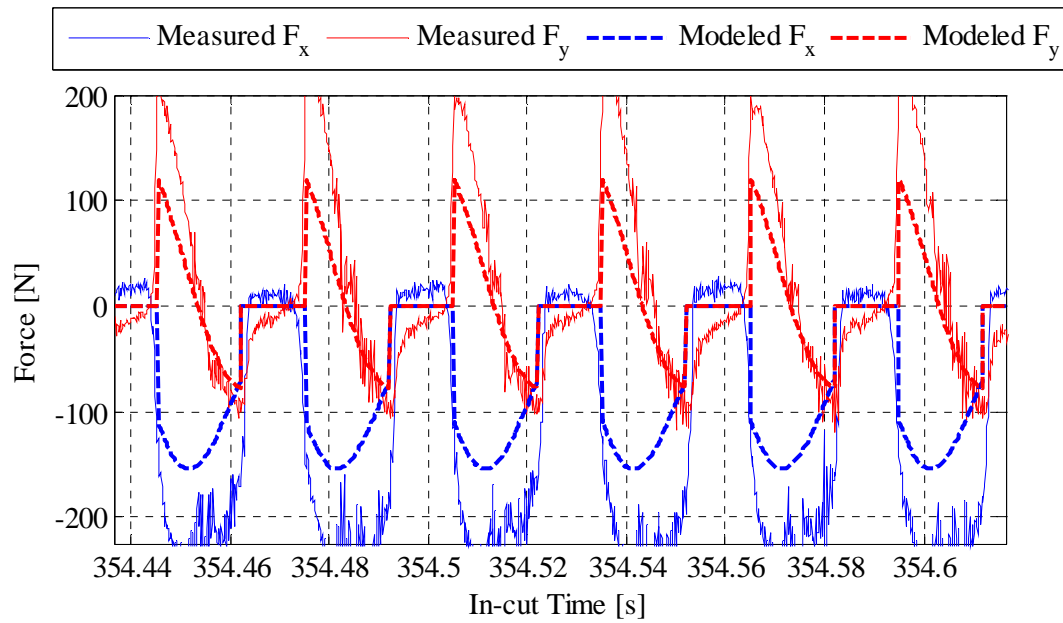


Figure B.24: Modeled forces compared to measured forces for the eighth pass of test 3.

Appendix C

Kalman Filter Matlab Code

The Matlab code used to implement the Kalman filter for tool wear estimation is shown below. The inputs are the measurements from the tool set station, TS_meas, in mm, volume of material removed per pass, Vol_MR, in mm³, the change in tool length to flank wear correlation factor, VB_TS_corr, and the initial wear model parameters, VB_dot_init and VB_init. The outputs are the *a posteriori* estimates of tool wear, VB_apo, for each pass within a given test.

```
TS_meas=Meas_TS_T3; %[mm] Measured change in tool length
Vol_MR=146.1; %[mm^3] volume of material removed in a single pass
VB_TS_corr=10; % VB|deltaL Correlation factor

%% Start of Tool Wear filter
% first a priori estimate of rate of VB change
VB_dot_init=3.48E-05;
% first a priori estimate of VB
VB_init=5.78E-02+(VB_dot_init*Vol_MR);

% Setup equation coefficient matrices
A=[1, Vol_MR; 0, 1];
H=[1/VB_TS_corr, 0];

% Setup covariances.
Q=[36, 0; 0, 0.01]; % Process covariance
R=400; % Measurement covariance

%Initialize a posteriori estimates of the P matrix and x vector
P=[49, 0.0002; 0.0002, 1e-8];
x_apo=[VB_init; VB_dot_init];

% Initialize vectors for Matlab
VB_apr=zeros(1,length(TS_meas));
VB_dot_apr=zeros(1,length(TS_meas));
VB_apo=zeros(1,length(TS_meas));
VB_dot_apo=zeros(1,length(TS_meas));

%Run filter
for i=1:length(TS_meas) %for each length measurement
    x_apr=A*x_apo; % Calculate a priori estimate of states
    P_apr=A*P*A'+Q; % Calculate a priori error covariance
    z=TS_meas(i); % initialize z

    K=P_apr*H'/(H*P_apr*H'+R); % Calculate Kalman gain
```

```

x_apo=x_apr+K*(z-H*x_apr); % Calculate a posterior state est.
P=([1, 0; 0, 1] -K*H)*P_apr; % Calculate a posterior P

% Transfer state estimates to appropriate variables
VB_apo(i)=x_apo(1);
VB_dot_apo(i)=x_apo(2);

VB_apr(i)=x_apr(1);
VB_dot_apr(i)=x_apr(2);
end

% Calculate a posteriori change in tool length.
del_L=VB_apo./(VB_TS_corr*1);

```

Appendix D

NC Program for Tests

The numerical control (NC) program used to conduct the tool wear tests is shown below. The comments describe the actions taking place at each step through the first pass of a test. After the first pass, the steps are repetitive but included here for completeness. The machining parameters, rotational speed, axial depth of cut, and feed per revolution were specified as variables in the beginning of the code. The tool was initially measured by the tool set station and the tool length was maintained for the entire test. The subsequent measurements for data collection were temporarily stored in an unused tool offset variable and written to a text file on the machine's controller. A second work coordinate system was defined for positioning the tool over the microscope. The microscope was removed during the tests to avoid damage from coolant spray.

```
ROT=1002 (Rotational Speed of cutter, rpm)
DOC=.250 (Axial depth of cut, mm)
FD=0.1 (Feed per revolution, mm)

(Specify coordinate system 96, 0,0,0 at front, top, left corner
of workpiece)
N010 G15 H96
(Open file for writing the tool setter data)
FWRITC MD1:TWEARAJH-T1.CSV
(Write header information)
PUT 'PNT'
PUT ', '
PUT 'R [mm]'
PUT ', '
PUT 'H [mm]'
WRITE C

(Setup Tool)
G56 H22 (Specify tool length offset of cutting tool, 22)
(Call subprogram for measuring length and diameter of cutting
tool 22)
CALL O9857 PB=3 PD=15.875 PT=22
(Write measurements to file)
PUT 'Actual Meas'
```

```

PUT ', '
PUT VTOFD[22], 7
PUT ', '
PUT VTOFH[22], 7
WRITE C

(Pre-Meas)
(Measure and write tool length and diameter three times)
(Store measurement values in an unused tool offset location)
CALL O9857 PB=3 PD=15.875 PT=65
PUT '0a'
PUT ', '
PUT VTOFD[65], 7
PUT ', '
PUT VTOFH[65], 7
WRITE C
CALL O9857 PB=3 PD=15.875 PT=65
PUT '0b'
PUT ', '
PUT VTOFD[65], 7
PUT ', '
PUT VTOFH[65], 7
WRITE C
CALL O9857 PB=3 PD=15.875 PT=65
PUT '0c'
PUT ', '
PUT VTOFD[65], 7
PUT ', '
PUT VTOFH[65], 7
WRITE C
M1

(Position the tool for Microscope measurements)
G15H72 (Specify coordinate system for measurements)
G0 X=0 Y=0 (Move to x and y positions)
G0 Z1000 (Position z at maximum point away from microscope)
M19 RS=45 (Rotate cutter to 45deg for measurement)
M1 (Optional Stop)
(BE CAREFUL WHEN LETTING THE TOOL COME DOWN!!!!)
G0 Z0 (Bring z into position for measurements)
M1 (Optional stop for acquiring pictures)
G0 Z1000 (Move z to maximum postion)
M19 RS=225 (Rotate tool by 180deg for second insert)
G0 Z0 (Bring z into position for measurements)
M1 (Optional stop for acquiring pictures)
G0 Z1000
M1 (REMOVE MICROSCOPE to avoid coolant damage)
G15H96 (Specify coordinate system for testing)

(Pass 1)
G95 (Specify feed in mm/rev rather than mm/min)
G56 H22 (Specify tool length offset of cutting tool, 22)
M3 S=ROT (Turn on spindle at specified rotational speed)
M8 (Turn on Coolant)

```

```

G0 X1.5625 Y-15 (Rapid to x and y position for first pass)
Z2.5 (Rapid to z position above workpiece)
G1 Z=-DOC F=FD (Feed to depth of cut at specified feed rate)
Y74.938 (Feed to back of part to machine material)
M9 (Coolant off)
G0 Z300 (Move tool to maximum z location, away from workpiece)
G94 (Specify feed in mm/min for tool set station measurements)
M1 (Optional stop)

```

```

(Position for Microscope)
(Repeat previous procedure)
G15H72
G0 X=0 Y=0
G0 Z1000
M19 RS=45
M1 (BE CAREFUL WHEN LETTING THE TOOL COME DOWN!!!!!!)
G0 Z0
M1
G0 Z1000
M19 RS=225
G0 Z0
M1
G0 Z1000
M1 (REMOVE MICROSCOPE)
G15H96

```

```

(OTS MEAS)
(Repeat method of measuring tool length and diameter)
CALL O9857 PB=3 PD=15.875 PT=65
PUT '1a'
PUT ', '
PUT VTOFD[65], 7
PUT ', '
PUT VTOFH[65], 7
WRITE C
CALL O9857 PB=3 PD=15.875 PT=65
PUT '1b'
PUT ', '
PUT VTOFD[65], 7
PUT ', '
PUT VTOFH[65], 7
WRITE C
CALL O9857 PB=3 PD=15.875 PT=65
PUT '1c'
PUT ', '
PUT VTOFD[65], 7
PUT ', '
PUT VTOFH[65], 7
WRITE C
M1

```

```

(Pass 2)
(Repeat machining pass for second location)
G95

```

```

G56 H22
M3 S=ROT
M8
G0 X11.0625 Y-15
Z2.5
G1 Z=-DOC F=FD
Y74.938
M9
G0 Z300
G94
M1

(Position for Microscope)
G15H72
G0 X=0 Y=0
G0 Z1000
M19 RS=45
M1 (BE CAREFUL WHEN LETTING THE TOOL COME DOWN!!!!!!)
G0 Z0
M1
G0 Z1000
M19 RS=225
G0 Z0
M1
G0 Z1000
M1 (REMOVE MICROSCOPE)
G15H96

(OTS MEAS)
CALL O9857 PB=3 PD=15.875 PT=65
PUT '2a'
PUT ', '
PUT VTOFD[65], 7
PUT ', '
PUT VTOFH[65], 7
WRITE C
CALL O9857 PB=3 PD=15.875 PT=65
PUT '2b'
PUT ', '
PUT VTOFD[65], 7
PUT ', '
PUT VTOFH[65], 7
WRITE C
CALL O9857 PB=3 PD=15.875 PT=65
PUT '2c'
PUT ', '
PUT VTOFD[65], 7
PUT ', '
PUT VTOFH[65], 7
WRITE C
M1

(Pass 3)
G95

```



```

G56 H22
M3 S=ROT
M8
G0 X20.5625 Y-15
Z2.5
G1 Z=-DOC F=FD
Y74.938
M9
G0 Z300
G94
M1

(Position for Microscope)
G15H72
G0 X=0 Y=0
G0 Z1000
M19 RS=45
M1 (BE CAREFUL WHEN LETTING THE TOOL COME DOWN!!!!!!)
G0 Z0
M1
G0 Z1000
M19 RS=225
G0 Z0
M1
G0 Z1000
M1 (REMOVE MICROSCOPE)
G15H96

(OTS MEAS)
CALL O9857 PB=3 PD=15.875 PT=65
PUT '3a'
PUT ', '
PUT VTOFD[65], 7
PUT ', '
PUT VTOFH[65], 7
WRITE C
CALL O9857 PB=3 PD=15.875 PT=65
PUT '3b'
PUT ', '
PUT VTOFD[65], 7
PUT ', '
PUT VTOFH[65], 7
WRITE C
CALL O9857 PB=3 PD=15.875 PT=65
PUT '3c'
PUT ', '
PUT VTOFD[65], 7
PUT ', '
PUT VTOFH[65], 7
WRITE C
M1

(Pass 4)
G95

```

```

G56 H22
M3 S=ROT
M8
G0 X30.0625 Y-15
Z2.5
G1 Z=-DOC F=FD
Y74.938
M9
G0 Z300
G94
M1

(Position for Microscope)
G15H72
G0 X=0 Y=0
G0 Z1000
M19 RS=45
M1 (BE CAREFUL WHEN LETTING THE TOOL COME DOWN!!!!!!)
G0 Z0
M1
G0 Z1000
M19 RS=225
G0 Z0
M1
G0 Z1000
M1 (REMOVE MICROSCOPE)
G15H96

(OTS MEAS)
CALL O9857 PB=3 PD=15.875 PT=65
PUT '4a'
PUT ', '
PUT VTOFD[65], 7
PUT ', '
PUT VTOFH[65], 7
WRITE C
CALL O9857 PB=3 PD=15.875 PT=65
PUT '4b'
PUT ', '
PUT VTOFD[65], 7
PUT ', '
PUT VTOFH[65], 7
WRITE C
CALL O9857 PB=3 PD=15.875 PT=65
PUT '4c'
PUT ', '
PUT VTOFD[65], 7
PUT ', '
PUT VTOFH[65], 7
WRITE C
M1

(Pass 5)
G95

```

```

G56 H22
M3 S=ROT
M8
G0 X39.5625 Y-15
Z2.5
G1 Z=-DOC F=FD
Y74.938
M9
G0 Z300
G94
M1

(Position for Microscope)
G15H72
G0 X=0 Y=0
G0 Z1000
M19 RS=45
M1 (BE CAREFUL WHEN LETTING THE TOOL COME DOWN!!!!!!)
G0 Z0
M1
G0 Z1000
M19 RS=225
G0 Z0
M1
G0 Z1000
M1 (REMOVE MICROSCOPE)
G15H96

(OTS MEAS)
CALL O9857 PB=3 PD=15.875 PT=65
PUT '5a'
PUT ', '
PUT VTOFD[65], 7
PUT ', '
PUT VTOFH[65], 7
WRITE C
CALL O9857 PB=3 PD=15.875 PT=65
PUT '5b'
PUT ', '
PUT VTOFD[65], 7
PUT ', '
PUT VTOFH[65], 7
WRITE C
CALL O9857 PB=3 PD=15.875 PT=65
PUT '5c'
PUT ', '
PUT VTOFD[65], 7
PUT ', '
PUT VTOFH[65], 7
WRITE C
M1

(Pass 6)
G95

```

```

G56 H22
M3 S=ROT
M8
G0 X49.0625 Y-15
Z2.5
G1 Z=-DOC F=FD
Y74.938
M9
G0 Z300
G94
M1

(Position for Microscope)
G15H72
G0 X=0 Y=0
G0 Z1000
M19 RS=45
M1 (BE CAREFUL WHEN LETTING THE TOOL COME DOWN!!!!!!)
G0 Z0
M1
G0 Z1000
M19 RS=225
G0 Z0
M1
G0 Z1000
M1 (REMOVE MICROSCOPE)
G15H96

(OTS MEAS)
CALL O9857 PB=3 PD=15.875 PT=65
PUT '6a'
PUT ', '
PUT VTOFD[65], 7
PUT ', '
PUT VTOFH[65], 7
WRITE C
CALL O9857 PB=3 PD=15.875 PT=65
PUT '6b'
PUT ', '
PUT VTOFD[65], 7
PUT ', '
PUT VTOFH[65], 7
WRITE C
CALL O9857 PB=3 PD=15.875 PT=65
PUT '6c'
PUT ', '
PUT VTOFD[65], 7
PUT ', '
PUT VTOFH[65], 7
WRITE C
M1

(Pass 7)
G95

```

```

G56 H22
M3 S=ROT
M8
G0 X58.5625 Y-15
Z2.5
G1 Z=-DOC F=FD
Y74.938
M9
G0 Z300
G94
M1

```

```

(Position for Microscope)
G15H72
G0 X=0 Y=0
G0 Z1000
M19 RS=45
M1 (BE CAREFUL WHEN LETTING THE TOOL COME DOWN!!!!!!)
G0 Z0
M1
G0 Z1000
M19 RS=225
G0 Z0
M1
G0 Z1000
M1 (REMOVE MICROSCOPE)
G15H96

```

```

(OTS MEAS)
CALL O9857 PB=3 PD=15.875 PT=65
PUT '7a'
PUT ', '
PUT VTOFD[65], 7
PUT ', '
PUT VTOFH[65], 7
WRITE C
CALL O9857 PB=3 PD=15.875 PT=65
PUT '7b'
PUT ', '
PUT VTOFD[65], 7
PUT ', '
PUT VTOFH[65], 7
WRITE C
CALL O9857 PB=3 PD=15.875 PT=65
PUT '7c'
PUT ', '
PUT VTOFD[65], 7
PUT ', '
PUT VTOFH[65], 7
WRITE C
M1

```

```

(Pass 8)
G95

```

```

G56 H22
M3 S=ROT
M8
G0 X68.0625 Y-15
Z2.5
G1 Z=-DOC F=FD
Y74.938
M9
G0 Z300
G94
M1

(Position for Microscope)
G15H72
G0 X=0 Y=0
G0 Z1000
M19 RS=45
M1 (BE CAREFUL WHEN LETTING THE TOOL COME DOWN!!!!!!)
G0 Z0
M1
G0 Z1000
M19 RS=225
G0 Z0
M1
G0 Z1000
M1 (REMOVE MICROSCOPE)
G15H96

(OTS MEAS)
CALL O9857 PB=3 PD=15.875 PT=65
PUT '8a'
PUT ', '
PUT VTOFD[65], 7
PUT ', '
PUT VTOFH[65], 7
WRITE C
CALL O9857 PB=3 PD=15.875 PT=65
PUT '8b'
PUT ', '
PUT VTOFD[65], 7
PUT ', '
PUT VTOFH[65], 7
WRITE C
CALL O9857 PB=3 PD=15.875 PT=65
PUT '8c'
PUT ', '
PUT VTOFD[65], 7
PUT ', '
PUT VTOFH[65], 7
WRITE C
CLOSE C (Close tool setter measurement file)
M30 (End Program)

```

Appendix D

Force Modeling Matlab Code

The Matlab code used to calculate the cutting force estimates is shown below. The inputs are the specific cutting coefficients, change in tool length to flank wear correlation factor, *a posteriori* wear estimates, and a structure element that contains the parameters for the test. The parameters structure includes the tool diameter, axial and radial depths of cut, spindle speed, feed per tooth, number of cutting teeth, a vector of cutter rotation angles, and a cumulative time vector. The vector of cutter rotation angles is a repeated array from 0° to 180°. It represents the angles of each tooth and the values correlate with the time in the time vector based on spindle speed. A travel distance ratio is calculated and used to interpolate between wear values for any instance of time. The outputs of this code are the normal and tangential cutting forces as well as the x and y cutting forces.

```
kn=2200;
kne=775;
kt=4500;
kte=850;

VB_TS_corr=10;
VB=[0, VB_apo];
del_L=VB./VB_TS_corr; %[mm]

% Get test parameters from a TestParams structure
d_tool=TestParams.d_tool; %Get the tool's diameter [mm].
DOC_r=TestParams.DOC_r; %Get the radial depth of cut [mm].
DOC_ax=TestParams.DOC_ax; %Get the axial depth of cut [mm].
S_speed=TestParams.speed; %Spindle Speed for the tests [rev/min]
feed=TestParams.feed; %feed rate [mm/(tooth*rev)]
Nt=TestParams.N_t; %tool's number of teeth
T_theta_comb=TestParams.theta; % Cutter rot. angle vector [deg].
time=TestParams.time; %vector of machining time [sec].

for i=1:8
    % Calculate beginning cutter rotation angle
    theta_s=acosd((DOC_r-d_tool/2)/(d_tool/2));
    theta_e=180; % Ending rotation angle is zero
    % Create the logical 'g' vector.
```

```

% This will dictate if the force is calculated or not.
g=zeros(length(T_theta_comb),1);
g(T_theta_comb>=theta_s&T_theta_comb<=theta_e)=1;

% Calculate a ratio for the distance traveled at any
% given instance of time.
trav_ratio=(time-time(start_index(i)))./...
            (time(end_index(i),1)-time(start_index(i),1));
curr_VB=trav_ratio.*((VB(i+1)-VB(i))+VB(i);
curr_del_L=curr_VB./VB_TS_corr;

%Calculate the uncut chip thickness.
h=feed(i).*sind(T_theta_comb).*g;
% Calc. the normal force edge component due to tool wear.
F_n_edge=kne.*curr_VB.*g;
% Calc. the tangential force edge component due to tool wear.
F_t_edge=kte.*curr_VB.*g;
%Calculate the normal force for each tooth.
F_n=(kn*(DOC_ax-curr_del_L).*h).*g+F_n_edge;
%Calculate the tangential force for each tooth.
F_t=(kt*(DOC_ax-curr_del_L).*h).*g+F_t_edge;

%Translate the normal and tangential forces to x forces
F_x=(F_t.*sind(T_theta_comb)-F_n.*cosd(T_theta_comb)).*g;
%Translate the normal and tangential forces to y forces
F_y=(F_t.*cosd(T_theta_comb)+F_n.*sind(T_theta_comb)).*g;
end

```


REFERENCES

- [1] D. Ulutan, T. Ozel, Machining induced surface integrity in titanium and nickel alloys: A review, *Int. J. Mach. Tools Manuf.* 51 (2011) 250-280.
- [2] A.J. Henderson, C. Bunget, T.R. Kurfess, Integration of On-Machine Measurements in the Force Modeling for Machining of Advanced Nickel-Based Superalloys, *Proc. Int. Symp. Flex. Autom.* (2012).
- [3] Google Scholar, Search Results, 2012 (2012).
- [4] E.O. Ezugwu, Z.M. Wang, A.R. Machado, The machinability of nickel-based alloys: a review, *J. Mater. Process. Technol.* 86 (1999) 1-16.
- [5] E.O. Ezugwu, J. Bonney, Y. Yamane, An overview of the machinability of aeroengine alloys, *J. Mater. Process. Technol.* 134 (2003) 233-253.
- [6] C.T. Sims, N.S. Stoloff, W.C. Hagel, *Superalloys II*, (1987) 598.
- [7] S.A. Sajjadi, S. Nategh, M. Isac, S.M. Zebarjad, Tensile deformation mechanisms at different temperatures in the Ni-base superalloy GTD-111, *J. Mater. Process. Technol.* 155–156 (2004) 1900-1904.
- [8] S.A. Sajjadi, S. Nategh, R.I.L. Guthrie, Study of microstructure and mechanical properties of high performance Ni-base superalloy GTD-111, *Materials Science and Engineering: A.* 325 (2002) 484-489.
- [9] T.L. Schmitz, K.S. Smith, *Machining Dynamics: Frequency Response to Improved Productivity*, Springer, 2009.
- [10] E.O. Ezugwu, S.H. Tang, Surface abuse when machining cast iron (G-17) and nickel-base superalloy (Inconel 718) with ceramic tools, *J. Mater. Process. Technol.* 55 (1995) 63-69.
- [11] S. Ranganath, C. Guo, P. Hegde, A finite element modeling approach to predict white layer formation in nickel superalloys, *CIRP Annals - Manufacturing Technology.* 58 (2009) 77-80.
- [12] R.S. Pawade, S.S. Joshi, P.K. Brahmanekar, Effect of machining parameters and cutting edge geometry on surface integrity of high-speed turned Inconel 718, *Int. J. Mach. Tools Manuf.* 48 (2008) 15-28.
- [13] B.J. Griffiths, Mechanism of white layer generation with reference to machining and deformation processes, *ASME J. Tribol.* 109 (1987) 525-530.
- [14] A. Ramesh, S.N. Melkote, Modeling of white layer formation under thermally dominant conditions in orthogonal machining of hardened AISI 52100 steel, *Int. J. Mach. Tools Manuf.* 48 (2008) 402-414.

- [15] B.J. Richardson, C. Bunget, T.R. Kurfess, A Statistically Based Determination of the Depth of the Machining Affected Zone in Nickel-Based Superalloys Using MATLAB, ASME Conf. Proc. 2010 (2010) 287-290.
- [16] Kistler Group, Multicomponent Dynamometer, -5 ... 10 kN, Top Plate 100x170 mm, Type 9257B - Data Sheet, 9257B_000-151e-11.09 (2009).
- [17] Kistler Group, Multichannel Charge Amplifier for Multicomponent Force Measurement, Type 5070A, 5070A_000-485e-03.10 (2010).
- [18] A.J. Henderson, M. Gall, C. Bunget, T. Kurfess, Machining Process Monitoring on Superalloys (Nickel-base Alloys): Phase I Progress Report, CUICAR/GE-2009-02 (2009).
- [19] Renishaw Inc., Probe Certification, SN: 20H207.
- [20] Renishaw Inc., OTS optical tool setter, H-5514-8200-01-A (2009).
- [21] Renishaw Inc., OMP40-2 optical machine probe, H-4071-8200-03-A (2008).
- [22] Sandvik Coromant, GC4240 and GC1030, C-1140:529 ENG/01 (2006).
- [23] Sandvik Coromant, Rotating Tools, Cutting tools from Sandvik Coromant. (2012).
- [24] A.J. Henderson, B.J. Richardson, C. Bunget, T. Kurfess, Machining Process Monitoring on Superalloys (Nickel-Based Superalloys): Phase II Progress Report, CUICAR/GE-2010-01 (2010).
- [25] A.J. Henderson, B.J. Richardson, Y. Chen, J. Tarbutton, C. Bunget, T. Kurfess, Machining Process Monitoring on Superalloys (Nickel-Based Superalloys): Phase III Progress Report, CUICAR/GE-2011-01 (2011).
- [26] Y. Chen, T. Klein, G. Wilson, N. DeVol, J. Tarbutton, C. Bunget, T. Kurfess, Machining Process Monitoring on Superalloys (Nickel-Based Superalloys): Phase IV Progress Report, CUICAR/GE-2011-02 (2011).
- [27] Y. Chen, A. Henderson, J. Milner, C. Boehmer, G. Wilson, C. Bunget, T. Kurfess, Machining Process Monitoring on Superalloys (Nickel-Based Superalloys): Phase V Progress Report, CUICAR/GE-2012-01 (2012).
- [28] Y. Chen, A. Henderson, M. Rokvam, G. Wilson, N. DeVol, J. Milner, C. Bunget, T. Kurfess, L. Mears, Machining Process Monitoring on Superalloys (Nickel-Based Superalloys): Phase VI Progress Report, CUICAR/GE-2012-02 (2012).
- [29] International Standards Organization, Tool life testing in milling - Part 2 End Milling, ISO 8688-2. (1989).
- [30] M. Nouari, A. Ginting, Wear characteristics and performance of multi-layer CVD-coated alloyed carbide tool in dry end milling of titanium alloy, Surface and Coatings Technology. 200 (2006) 5663-5676.

- [31] N.H. Cook, Tool Wear and Tool Life, J. Eng. for Industry. 95 (1973) 931-938.
- [32] A. Devillez, S. Lesko, W. Mozer, Cutting tool crater wear measurement with white light interferometry, Wear. 256 (2004) 56-65.
- [33] A. Bhattacharyya, I. Ham, Analysis of Tool Wear---Part I: Theoretical Models of Flank Wear, J. Eng. for Industry. 91 (1969) 790-796.
- [34] I.A. Choudhury, M.A. El-Baradie, Machinability of nickel-base super alloys: a general review, J. Mater. Process. Technol. 77 (1998) 278-284.
- [35] H.Z. Li, H. Zeng, X.Q. Chen, An experimental study of tool wear and cutting force variation in the end milling of Inconel 718 with coated carbide inserts, J. Mater. Process. Technol. 180 (2006) 296-304.
- [36] F.W. Taylors, On the Art of Cutting Metals, The American Society of Mechanical Engineers, New York, 1907.
- [37] S. Kalpakjian, S.R. Schmid, Manufacturing Processes for Engineering Materials, 4th ed., Pearson Education, Inc., Upper Saddle River, NJ, 2003.
- [38] Y. Koren, E. Lenz, Mathematical model for the flank wear while turning steel with carbide tools, CIRP Proceedings on Manufacturing Systems. 1 (1972) 127-139.
- [39] E. Usui, T. Shirakashi, T. Kitagawa, Analytical prediction of cutting tool wear, Wear. 100 (1984) 129-151.
- [40] T. Wong, W. Kim, P. Kwon, Experimental support for a model-based prediction of tool wear, Wear. 257 (2004) 790-798.
- [41] M. Teitenberg, A.E. Bayoumi, G. Yucessan, Tool wear modeling through analytical mechanistic model of milling process, Wear. 154 (1992) 287-304.
- [42] T.A. Papazafiriou, M.A. Elbestawi, Flank wear modeling in milling, J. Mech. Work. Technol. 20 (1989) 93-104.
- [43] Y. Koren, A.G. Ulsoy, K. Danai, Tool Wear and Breakage Detection Using a Process Model, CIRP Ann. Manuf. Technol. 35 (1986) 283-288.
- [44] Y. Koren, Flank Wear Model of Cutting Tools Using Control Theory, Journal of Engineering for Industry. 100 (1978) 103.
- [45] J.L. Milner, J.T. Roth, Condition Monitoring for Indexable Carbide End Mill Using Acceleration Data, Mach. Sci. Technol. 14 (2010) 63-80.
- [46] S.K. Choudhury, S. Rath, In-process tool wear estimation in milling using cutting force model, J. Mater. Process. Technol. 99 (2000) 113-119.

- [47] S.E. Oraby, D.R. Hayhurst, Tool wear and force relationship in metal cutting, *Int. J. Mech. Sci.* 33 (1991) 125-138.
- [48] J. Karandikar, R.E. Zapata, T.L. Schmitz, Incorporating Stability, Surface Location Error, Tool Wear, and Uncertainty in the Milling Super Diagram, *Trans. NAMRI/SME.* 38 (2010) 229.
- [49] S.Y. Liang, R.L. Hecker, R.G. Landers, Machining process monitoring and control: the state-of-the-art, *J. Manuf. Sci. Eng.* 126 (2004) 297-310.
- [50] J.T. Roth, D. Djurdjanovic, X. Yang, L. Mears, T. Kurfess, Quality and Inspection of Machining Operations: Tool Condition Monitoring, *J. Manuf. Sci. Eng.* 132 (2010) 041015.
- [51] D. Cuppini, G. D'errico, G. Rutelli, Tool wear monitoring based on cutting power measurement, *Wear.* 139 (1990) 303-311.
- [52] I.N. Tansel, A. Wagiman, A. Tziranis, Recognition of chatter with neural networks, *Int. J. Mach. Tools Manuf.* 31 (1991) 539-552.
- [53] E. Kuljanic, M. Sortino, TWEM, a method based on cutting forces - monitoring tool wear in face milling, *Int. J. Mach. Tools Manuf.* 45 (2005) 29-34.
- [54] A. Sarhan, R. Sayed, A.A. Nassr, R.M. El-Zahry, Interrelationships between cutting force variation and tool wear in end-milling, *J. Mater. Process. Technol.* 109 (2001) 229-235.
- [55] S.Y. Liang, D.A. Dornfeld, Tool Wear Detection Using Time Series Analysis of Acoustic Emission, *Journal of Engineering for Industry.* 111 (1989) 199-205.
- [56] A.E. Diniz, J.J. Liu, D.A. Dornfeld, Correlating tool life, tool wear and surface roughness by monitoring acoustic emission in finish turning, *Wear.* 152 (1992) 395-407.
- [57] C. Bradley, Y.S. Wong, Surface Texture Indicators of Tool Wear - A Machine Vision Approach, *Int. J. Adv. Manuf. Technol.* 17 (2001) 435-443.
- [58] S.A. Coker, Y.C. Shin, In-process control of surface roughness due to tool wear using a new ultrasonic system, *Int. J. Mach. Tools Manuf.* 36 (1996) 411-422.
- [59] T. Pfeifer, L. Wieggers, Reliable tool wear monitoring by optimized image and illumination control in machine vision, *Measurement.* 28 (2000) 209-218.
- [60] P.W. Prickett, C. Johns, An overview of approaches to end milling tool monitoring, *Int. J. Mach. Tools Manuf.* 39 (1999) 105-122.
- [61] D. Shouszhi, D. Yanting, S. Weixiang, The detection and compensation of tool wear in process, *J. Mater. Process. Technol.* 48 (1995) 283-290.
- [62] L. Mears, J.T. Roth, D. Djurdjanovic, X. Yang, T. Kurfess, Quality and Inspection of Machining Operations: CMM Integration to the Machine Tool, *J. Manuf. Sci. Eng.* 131 (2009) 1-14.

- [63] R.E. Kalman, A New Approach to Linear Filtering and Prediction Problems, Transaction of the ASME - Journal of Basic Engineering. 82 (Series D) (1960) 35-10.
- [64] G. Welch, G. Bishop, An Introduction to the Kalman Filter, SIGGRAPH 2001. Course 8 (2001).
- [65] P.S. Maybeck, Stochastic models, estimation, and control, (1979).
- [66] H.V. Ravindra, Y.G. Srinivasa, R. Krishnamurthy, Acoustic emission for tool condition monitoring in metal cutting, Wear. 212 (1997) 78-84.
- [67] Y. Altintas, S.S. Park, Dynamic Compensation of Spindle-Integrated Force Sensors, CIRP Ann. Manuf. Technol. 53 (2004) 305-308.
- [68] K. Erkorkmaz, Y. Altintas, High speed CNC system design. Part II: modeling and identification of feed drives, Int. J. Mach. Tools Manuf. 41 (2001) 1487-1509.
- [69] K. Erkorkmaz, Y. Altintas, High speed CNC system design. Part III: high speed tracking and contouring control of feed drives, Int. J. Mach. Tools Manuf. 41 (2001) 1637-1658.
- [70] H.-. Möhring, K.M. Litwinski, O. Gümmner, Process monitoring with sensory machine tool components, CIRP Ann. Manuf. Technol. 59 (2010) 383-386.
- [71] K. Lou, C. Lin, An intelligent sensor fusion system for tool monitoring on a machining centre, The International Journal of Advanced Manufacturing Technology. 13 (1997) 556-565.
- [72] S.S. Park, M. Malekian, Mechanistic modeling and accurate measurement of micro end milling forces, CIRP Ann. Manuf. Technol. 58 (2009) 49-52.
- [73] R.E. Kalman, R.S. Bucy, New Results in Linear Filtering and Prediction Theory, ASME Journal of Basic Engineering. 83 (1961) 95-12.
- [74] M. Alauddin, M.A. El Baradie, M.S.J. Hashmi, Modelling of cutting force in end milling Inconel 718, J. Mater. Process. Technol. 58 (1996) 100-108.
- [75] R. Arunachalam, M.A. Mannan, Machinability of Nickel-based high temperature alloys, Mach. Sci. Technol. 4 (2000) 127-168.
- [76] H.E. Jenkins, T.R. Kurfess, R.C. Dorf, Design of a Robust Controller for a Grinding System, The IEEE Transactions on Control Systems Technology. 4 (1996) 40-49.
- [77] B.C. Ulmer, T.R. Kurfess, Integration of an Open Architecture Controller with a Diamond Turning Machine, Mechatronics. 9 (1999) 349-362.
- [78] R. Cowan, T.R. Kurfess, D. Schertz, An Adaptive Statistically Based Controller for Through-Feed Centerless Grinding, ASME J. Manuf. Sci. Eng. 123 (2001) 380-386.

- [79] H.A. Razavi, S. Danyluk, T.R. Kurfess, Force Control Grinding of Gamma Titanium Aluminide, *Int. J. Mach. Tools Manuf.* 43 (2003) 185-191.
- [80] O. Gonzalo, J. Beristain, H. Jauregi, C. Sanz, A method for the identification of the specific force coefficients for mechanistic milling simulation, *Int. J. Mach. Tools Manuf.* 50 (2010) 765-774.
- [81] M.E. Merchant, Basic mechanics of the metal cutting process, *ASME J. Appl. Phys.* 11 (1944) 168-175.
- [82] G.V. Stabler, The Fundamental Geometry of Cutting Tools, *Proc. Inst. Mech. Eng.* 165 (1951) 14-26.
- [83] J.K. Russell, R.H. Brown, The measurement of chip flow direction, *Int. J. Mach. Tool Des. Res.* 6 (1966) 129-138.
- [84] L.N. Payton, A Basic Correction to the Orthogonal Metal Cutting Models, *ASME Conf. Proc.* 2009 (2009) 455-465.
- [85] M.E. Merchant, Mechanics of the Metal Cutting Process. I. Orthogonal Cutting and a Type 2 Chip, *J. Appl. Phys.* 16 (1945) 267-275.
- [86] G.R. Johnson, W.H. Cook, A constitutive model and data for metals subjected to large strains, high strain rates and high temperatures, *Proc. 7th International Symposium on Ballistics.* (1983) 541-547.
- [87] W.L. Stone, T.R. Kurfess, Titanium Aluminide – Thermal Diffusivity, Heat Capacitance, and Coefficient of Thermal Expansion as a Function of Temperature, *Transactions of the North American Research Institute.* 30 (2002) 417-421.
- [88] Y. Chen, C. Bunget, T. Kurfess, Investigations in Subsurface Damage when Machining Nickel-based Superalloys, 40 (2012).
- [89] B. Shi, H. Attia, N. Tounsi, Identification of Material Constitutive Laws for Machining--- Part I: An Analytical Model Describing the Stress, Strain, Strain Rate, and Temperature Fields in the Primary Shear Zone in Orthogonal Metal Cutting, *J. Manuf. Sci. Eng.* 132 (2010) 051008.
- [90] C.Y.H. Lim, P.P.T. Lau, S.C. Lim, The effects of work material on tool wear, *Wear.* 250 (2001) 344-348.
- [91] OKUMA Corporation, MB-46VAE Test Record, SN: 129716.
- [92] A.J. Henderson, C. Bunget, T.R. Kurfess, Cutting Force Modeling When Milling Nickel-Base Superalloys, *ASME Conf. Proc.* 2010 (2010) 193-202.
- [93] A.J. Henderson, C. Bunget, T.R. Kurfess, On-Machine Monitoring of Tool Wear with Touch Probes, *Proc. NAMRI/SME.* (2011).

- [94] A.J. Henderson, C. Bunget, T.R. Kurfess, Updated Mechanistic Force Model to Account for Rapid Tool Wear when Milling Nickel-Based Superalloys, Proc. NAMRI/SME. (2012).
- [95] A. Henderson, C. Bunget, T. Kurfess, Estimating Tool Wear and Cutting Forces When End-Milling Using On-Machine Touch Probes, ASME J. Manuf. Sci. Eng. (Under Review).